

## Library Declaration and Deposit Agreement

### 1. STUDENT DETAILS

Ethan Moorfield  
2043500

### 2. THESIS DEPOSIT

- 2.1 I understand that under my registration at the University, I am required to deposit my thesis with the University in BOTH hard copy and in digital format. The digital version should normally be saved as a single pdf file.
- 2.2 The hard copy will be housed in the University Library. The digital version will be deposited in the University's Institutional Repository (WRAP). Unless otherwise indicated (see 2.3 below) this will be made openly accessible on the Internet and will be supplied to the British Library to be made available online via its Electronic Theses Online Service (EThOS) service. [At present, theses submitted for a Master's degree by Research (MA, MSc, LLM, MS or MMedSci) are not being deposited in WRAP and not being made available via EthOS. This may change in future.]
- 2.3 In exceptional circumstances, the Chair of the Board of Graduate Studies may grant permission for an embargo to be placed on public access to the hard copy thesis for a limited period. It is also possible to apply separately for an embargo on the digital version. (Further information is available in the Guide to Examinations for Higher Degrees by Research.)
- 2.4 (a) Hard Copy I hereby deposit a hard copy of my thesis in the University Library to be made publicly available to readers immediately.  
I agree that my thesis may be photocopied.
- (b) Digital Copy I hereby deposit a digital copy of my thesis to be held in WRAP and made available via EThOS.  
My thesis can be made publicly available online.

### 3. GRANTING OF NON-EXCLUSIVE RIGHTS

Whether I deposit my Work personally or through an assistant or other agent, I agree to the following: Rights granted to the University of Warwick and the British Library and the user of the thesis through this agreement are non-exclusive. I retain all rights in the thesis in its present version or future versions. I agree that the institutional repository administrators and the British Library or their agents may, without changing content, digitise and migrate the thesis to any medium or format for the purpose of future preservation and accessibility.

#### 4. DECLARATIONS

(a) I DECLARE THAT:

- I am the author and owner of the copyright in the thesis and/or I have the authority of the authors and owners of the copyright in the thesis to make this agreement. Reproduction of any part of this thesis for teaching or in academic or other forms of publication is subject to the normal limitations on the use of copyrighted materials and to the proper and full acknowledgement of its source.
- The digital version of the thesis I am supplying is the same version as the final, hardbound copy submitted in completion of my degree, once any minor corrections have been completed.
- I have exercised reasonable care to ensure that the thesis is original, and does not to the best of my knowledge break any UK law or other Intellectual Property Right, or contain any confidential material.
- I understand that, through the medium of the Internet, files will be available to automated agents, and may be searched and copied by, for example, text mining and plagiarism detection software.

(b) IF I HAVE AGREED (in Section 2 above) TO MAKE MY THESIS PUBLICLY AVAILABLE DIGITALLY, I ALSO DECLARE THAT:

- I grant the University of Warwick and the British Library a licence to make available on the Internet the thesis in digitised format through the Institutional Repository and through the British Library via the EThOS service.
- If my thesis does include any substantial subsidiary material owned by third-party copyright holders, I have sought and obtained permission to include it in any version of my thesis available in digital format and that this permission encompasses the rights that I have granted to the University of Warwick and to the British Library.

#### 5. LEGAL INFRINGEMENTS

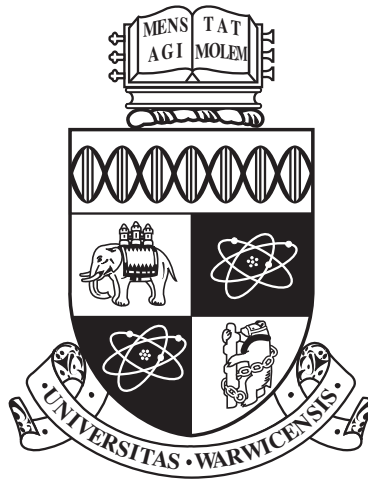
I understand that neither the University of Warwick nor the British Library have any obligation to take legal action on behalf of myself, or other rights holders, in the event of infringement of intellectual property rights, breach of contract or of any other right, in the thesis.

---

*Please sign this agreement and return it to the Graduate School Office when you submit your thesis.*

Student's signature: Ethan Moorfield

Date: 19-09-24



**Illuminating the Elusive: Identifying astrophysically  
important Compact Binaries.**

by

**Ethan Moorfield**

**Thesis**

Submitted to the University of Warwick

for the degree of

**Master of Science (by Research) in Physics**

**Physics**

September 2024

THE UNIVERSITY OF  
**WARWICK**

# Contents

<b>List of Figures</b>	<b>v</b>
<b>List of Tables</b>	<b>viii</b>
<b>Acknowledgments</b>	<b>ix</b>
<b>Declarations</b>	<b>x</b>
<b>Abstract</b>	<b>xi</b>
<b>Abbreviations</b>	<b>xii</b>
<b>Chapter 1 Compact Binaries in Modern Day Astrophysics</b>	<b>1</b>
<b>Chapter 2 Single Star Evolution</b>	<b>3</b>
2.1 Nuclear Fusion . . . . .	3
2.2 Stellar Expansion . . . . .	3
2.3 Stellar Winds . . . . .	4
2.4 Compact Object Formation . . . . .	4
<b>Chapter 3 Compact Binary Formation and Evolution</b>	<b>8</b>
3.1 Mass transfer through Roche Lobe Overflow . . . . .	9
3.2 Mechanisms for the Loss of Orbital Angular Momentum . . . . .	10
3.2.1 Gravitational Wave Radiation . . . . .	10
3.2.2 Magnetic Braking . . . . .	10
3.3 Conservation in Mass Transfer . . . . .	11
3.3.1 Conservative Mass Transfer . . . . .	11
3.3.2 Non-conservative Mass Transfer . . . . .	11
3.4 Orbital Evolution driven by Mass Transfer . . . . .	12
3.4.1 Orbital Evolution under Conservative Mass Transfer . . . . .	12

3.4.2	Orbital Evolution under Non-conservative Mass Transfer . . .	12
3.5	Stability of Mass Transfer . . . . .	13
3.5.1	Response of the Donor . . . . .	14
3.5.2	Response of the Roche Lobe . . . . .	15
3.6	Common Envelope Evolution . . . . .	15
3.7	Accretion Disc Formation . . . . .	17
3.8	X-rays and the Boundary Layer . . . . .	18
3.9	Accretion as a Source of Energy . . . . .	19
3.9.1	The Efficiency of Fusion . . . . .	19
3.9.2	The Efficiency of Accretion . . . . .	19
3.9.3	The Eddington Limit . . . . .	20
<b>Chapter 4 White Dwarf Binaries</b>		<b>22</b>
4.1	Formation Channels . . . . .	22
4.2	Symbiotic Stars . . . . .	25
4.3	Cataclysmic Variables . . . . .	25
4.3.1	Properties and Evolution . . . . .	25
4.3.2	Classical Novae . . . . .	27
4.4	Non-magnetic Cataclysmic Variables . . . . .	27
4.4.1	Dwarf Novae . . . . .	27
4.4.2	Novalike Variables . . . . .	32
4.4.3	AMCVn . . . . .	32
4.5	Magnetic Cataclysmic Variables . . . . .	33
4.5.1	Polars . . . . .	33
4.5.2	Intermediate Polars . . . . .	34
4.5.3	Pre-Polars . . . . .	35
4.6	White Dwarf Pulsars . . . . .	36
<b>Chapter 5 X-ray Binaries</b>		<b>41</b>
5.1	The X-ray Binary Zoo . . . . .	41
5.1.1	Low-Mass and High-Mass X-ray Binaries . . . . .	41
5.1.2	Pulsing X-ray Binaries . . . . .	42
5.1.3	Non-Pulsing X-ray Binaries . . . . .	45
5.1.4	X-ray Binary Formation Channels . . . . .	46
5.2	Observations at Longer Wavelengths . . . . .	49

<b>Chapter 6</b>	<b>The Compact Binary Landscape</b>	<b>50</b>
6.1	Gaps in our Current Understanding . . . . .	50
6.1.1	Observational Bias . . . . .	51
6.1.2	The Most Problematic Compact Binary Subtypes . . . . .	51
6.1.3	The Way Forward . . . . .	52
<b>Chapter 7</b>	<b>Methods</b>	<b>53</b>
7.1	Observational Techniques . . . . .	53
7.1.1	Observing a System’s Brightness through Time . . . . .	53
7.1.2	Estimating the Orbital Period . . . . .	54
7.1.3	Estimating the Rate of Mass Transfer . . . . .	55
7.1.4	Measuring the Magnetic Field Strength . . . . .	57
7.1.5	Constraining the Mass of the Accretor . . . . .	59
7.2	The AstroToolkit Package . . . . .	61
7.2.1	The Query Tool . . . . .	63
7.2.2	The Bokeh Plotting Library . . . . .	68
7.2.3	Matching Positional Data . . . . .	69
7.2.4	Datapages . . . . .	71
7.2.5	Local Data Management . . . . .	73
7.2.6	Usability . . . . .	73
7.3	STILTS . . . . .	73
7.4	Instrumentation . . . . .	74
7.4.1	Optical Surveys . . . . .	74
7.4.2	The Thai National Observatory . . . . .	74
7.4.3	The Palomar Observatory . . . . .	75
7.4.4	The Lick Observatory . . . . .	75
7.4.5	The BlackCAT Catalogue . . . . .	75
<b>Chapter 8</b>	<b>The Search for White Dwarf Pulsars</b>	<b>76</b>
8.1	Methodology . . . . .	76
8.1.1	Obtaining a Set of Candidates . . . . .	76
8.1.2	Obtaining and Analysing Light Curves . . . . .	81
8.2	Results . . . . .	83
8.2.1	J235354.93+415304.33 . . . . .	83
8.2.2	J045254.56+301718.00 . . . . .	87
8.2.3	J035055.99–204815.82 . . . . .	90
8.2.4	J201135.84–021340.49 . . . . .	93
8.2.5	J235354.93+415304.33 . . . . .	95

8.2.6	J142438.93–022739.25 . . . . .	96
8.3	Summary . . . . .	99
<b>Chapter 9 The Search for X-ray Binaries</b>		<b>100</b>
9.1	Methodology . . . . .	100
9.1.1	Obtaining a Set of Candidates . . . . .	100
9.1.2	Obtaining and Analysing Light Curves . . . . .	105
9.1.3	Estimating Spectral Types . . . . .	108
9.2	Results . . . . .	110
9.2.1	Spectral Type Distribution . . . . .	110
9.2.2	Orbital Period and X-ray Flux Distributions . . . . .	112
9.2.3	Exploring the Candidates . . . . .	112
9.3	Summary . . . . .	116
<b>Chapter 10 Discussion</b>		<b>117</b>
10.1	Contamination . . . . .	117
10.1.1	Contaminants in the White Dwarf Pulsar Search . . . . .	117
10.1.2	Contaminants in the X-ray Binary Search . . . . .	117
10.1.3	The Problem of Contamination . . . . .	119
10.2	Search Optimisation . . . . .	121
10.3	Future Developments . . . . .	123
10.3.1	Instrumentation . . . . .	123
10.3.2	Novel Approaches . . . . .	124
10.4	Further Work . . . . .	125
10.4.1	The White Dwarf Pulsar Search . . . . .	125
10.4.2	The X-ray Binary Search . . . . .	125
<b>Chapter 11 Conclusions</b>		<b>126</b>
<b>Appendices</b>		<b>1</b>

# List of Figures

3.1	Interacting Binary Configuration . . . . .	9
4.1	White Dwarf Binary Formation Channels . . . . .	23
4.2	Dwarf Nova Light Curve . . . . .	28
4.3	SU UMa Light Curve . . . . .	29
4.4	ER UMa Light Curve . . . . .	29
4.5	WZ Sge Light Curve . . . . .	30
4.6	Z Cam Light Curve . . . . .	31
4.7	AM CVn Light Curve . . . . .	32
4.8	Polar Light Curve . . . . .	34
4.9	Intermediate Polar Light Curve . . . . .	35
4.10	Pre-Polar Light Curve . . . . .	36
4.11	AR Sco Light Curve . . . . .	37
4.12	AR Sco Time Series Analysis . . . . .	38
4.13	White Dwarf Pulsars and Delta Scuti Stars in the Hertzsprung-Russell Diagram . . . . .	39
5.1	X-ray Binary Formation Channels . . . . .	47
5.2	Transient X-ray Binary Light Curve . . . . .	49
7.1	Phase Folding Example . . . . .	55
7.2	Novalike Variable and AM CVn SDSS Spectra . . . . .	56
7.3	Pre-Polar Spectrum . . . . .	58
7.4	Zeeman Splitting Spectrum . . . . .	59
7.5	Cyclotron Hump Spectrum . . . . .	60
7.6	AstroToolkit Proper Motion Correction Example . . . . .	62
7.7	AstroToolkit Light Curve Example . . . . .	65
7.8	AstroToolkit Detection Correction Example . . . . .	67
7.9	AstroToolkit Spectrum Example . . . . .	68

7.10	AstroToolkit Spectral Energy Distribution Example . . . . .	69
7.11	AstroToolkit Positional Data Matching Example . . . . .	70
7.12	AstroToolkit Datapage Example . . . . .	72
7.13	Optical Survey Transmission Profiles . . . . .	74
8.1	Cut to the Hertzsprung-Russell Diagram in the White Dwarf Pulsar Search . . . . .	77
8.2	J191213.72–441045.08 Light Curve . . . . .	78
8.3	Candidate Filtering Results in the White Dwarf Pulsar Search . . . . .	80
8.4	Candidate Filtering Results in the White Dwarf Pulsar Search (Percentages) . . . . .	81
8.5	ZTF Query Success Distribution in the White Dwarf Pulsar Search . . . . .	82
8.6	AR Sco’s High-Speed Photometry and Optical Spectra . . . . .	84
8.7	J235354.93+415304.33 Light Curve . . . . .	85
8.8	J235354.93+415304.33 Phase-Resolved Spectra . . . . .	86
8.9	J045254.56+301718.00 Light Curve . . . . .	88
8.10	J045254.56+301718.00 High-Speed Photometry . . . . .	89
8.11	J045254.56+301718.00 Spectrum . . . . .	90
8.12	J035055.99–204815.82 Light Curves . . . . .	91
8.13	Locations of Known ER UMa Systems in the Hertzsprung-Russell Diagram against J035055.99–204815.82 . . . . .	92
8.14	Location of J035055.99–204815.82 on a Positional Map of Known Young Stellar Objects . . . . .	93
8.15	J201135.84–021340.49 Light Curves . . . . .	94
8.16	J201135.84–021340.49 Power Spectra . . . . .	95
8.17	J095308.20+145836.44 High-Speed Photometry . . . . .	96
8.18	J142438.93–022739.25 Light Curves . . . . .	97
8.19	J142438.93–022739.25 High-Speed Photometry . . . . .	98
9.1	Cut to the Hertzsprung-Russell Diagram in the X-ray Binary Search . . . . .	103
9.2	Candidate Filtering Results in the X-ray Binary Search . . . . .	104
9.3	Candidate Filtering Results in the X-ray Binary Search (Percentages) . . . . .	105
9.4	X-ray Binary Candidate Astrometry . . . . .	106
9.5	Time Series of a Known Black Hole X-ray Binary using ATLAS and ZTF . . . . .	107
9.6	Time Series Analysis of the TESS Photometry of a Known Black Hole X-ray Binary . . . . .	108

9.7	X-ray Binary Candidate Typical Spectral Type Distribution on the Hertzsprung-Russell Diagram . . . . .	109
9.8	X-ray Binary Candidate Typical Spectral Type Distribution . . . . .	110
9.9	X-ray Binary Candidate Orbital Period Distribution . . . . .	111
9.10	X-ray Binary Candidate X-ray Flux Distribution . . . . .	111
9.11	Classifications of Known Systems among the final set of X-ray Binary Candidates . . . . .	112
9.12	Phase-Folded TESS Photometry of five Black Hole Binary Candidates . . . . .	113
9.13	ATLAS photometry of two Black Hole Binary Candidates, J133030.39–361425.93 and J052830.76–045403.73 . . . . .	114
9.14	J151503.52-433712.50 TESS Outburst . . . . .	115
10.1	Light Curves of the Main Contaminants in the X-ray Binary Search	118
10.2	Hertzsprung-Russel Diagram Positions of the main Contaminants in the White Dwarf Pulsar Search . . . . .	120

# List of Tables

8.1	Key Parameters of the Reference White Dwarf Pulsars . . . . .	79
8.2	Known Systems returned by the White Dwarf Pulsar Search . . . . .	83
9.1	Key Parameters of the Reference Black Hole Binaries . . . . .	101

# Acknowledgments

I would like to thank Prof. Boris Gänsicke for providing me with the opportunity to undertake this project, and for his invaluable support throughout. I would also like to thank the rest of the WDPLANETS group and any others who assisted or showed interest in this work, with particular thanks to Dr Keith Inight for his continued assistance in the technical aspects that this work demanded. I also wish to extend my gratitude to Tony Rodriguez, Caltech, for his help in obtaining optical spectra for a number of systems identified in this work. Outside of academia, I would like to give thanks to my close family and friends for their unending support, with particular thanks to my mum, dad, sister and partner for putting up with me through the writing process. I would finally like to thank those responsible for all prior research on which this work stands.

# Declarations

I declare that the work presented in this thesis is entirely my own, except where stated otherwise by reference or acknowledgement. This work was carried out at the University of Warwick during the period July 2023 to September 2024, and has not been submitted to any other academic institution or for the purpose of any other degree or qualification.

# Abstract

Due to their wide utility in the study of astrophysical phenomena—from gravitational waves to extreme quantum interactions—it is difficult to overstate the importance of compact binaries in modern astrophysics. Advancements in optical and X-ray instrumentation have ushered in a new era in the identification of astronomical systems, and yet the populations of many compact binaries remain small. The goal of this work was therefore to expand the populations of two elusive classes of compact binaries: white dwarf pulsars and black hole binaries.

To facilitate the retrieval and analysis of archival data, a Python package, *AstroToolkit*, was developed. The search for white dwarf pulsar candidates was achieved through an exploration of Gaia’s third data release, using three known white dwarf pulsars as reference. An analysis of ZTF photometry resulted in the identification of 58 candidates, at least one of which shows significant promise. We are in the process of obtaining spectroscopy to confirm or refute J2011–0213 as a fourth white dwarf pulsar. Through photometry from the Thai National Telescope and spectra from the Hale and Shane Telescopes, several interesting systems were revealed—including a previously unidentified pre-polar and an extreme young stellar object. The search for black hole binary candidates used four reference systems selected from 72 known black hole binaries. Through the analysis of ATLAS and TESS photometry, these systems were utilised in the identification of 322 candidates in a cross-match of Gaia’s third data release with the first data release of eROSITA-DE. While the time constraints of an MSc limited the depth of this search, 35 candidates exhibit unambiguous ellipsoidal modulation in their phase-folded photometry and hence require further follow-up at a later date.

The contaminants in either set of candidates were identified, and improvements to similar searches—including new analytical approaches and upcoming advancements in instrumentation—are discussed.

# Abbreviations

**AEN** Astrometric Excess Noise

**AENS** Astrometric Excess Noise Significance

**AOVMHW** Multi-Harmonic Analysis Of Variance

**ATK** AstroToolkit

**ATLAS** Asteroid Terrestrial-impact Last Alert System

**CE** Common Envelope

**CEE** Common Envelope Evolution

**CV** Cataclysmic Variable

**eROSITA** extended ROentgen Survey with an Imaging Telescope Array

**FWHM** Full Width at Half Maximum

**GALEX** Galaxy Evolution Explorer

**HMXB** High-Mass X-ray Binary

**HRD** Hertzsprung-Russell Diagram

**LIGO** Laser Interferometer Gravitational-Wave Observatory

**LMXB** Low-Mass X-ray Binary

**Pan-STARRS** Panoramic Survey Telescope and Rapid Response System

**RUWE** Renormalised Unit Weight Error

**SDSS** Sloan Digital Sky Survey

**SED** Spectral Energy Distribution

**SIMBAD** the Set of Identifications, Measurements and Bibliography for Astronomical  
Data

**STILISM** STructuring by Inversion the Local Interstellar Medium

**STILTS** Starlink Tables Infrastructure Library Tool Set

**TESS** Transiting Exoplanet Survey Satellite

**TNT** Thai National Telescope

**YSO** Young Stellar Object

**ZTF** Zwicky Transient Facility

$M_{\odot}$  Solar Mass,  $1.989 \times 10^{30}$  kg

au Astronomical Unit,  $1.496 \times 10^8$  km

# Chapter 1

## Compact Binaries in Modern Day Astrophysics

Binary systems—systems in which two stars orbit a common centre of mass—are of great importance to astrophysics, in no small part due to them (or higher multiple systems) being equally or more abundant than single stars (see Whitworth and Lomax [2015], Chen et al. [2024]). Furthermore, the presence of a companion allows for the constraining of stellar parameters that would not normally be possible for single stars. The focus of this work will be on a subset of binary systems—compact binaries. These are systems containing two (often closely orbiting) components in which at least one component is a compact object: a white dwarf, neutron star or black hole. In up to 50% of compact binary systems, the orbital separation is large enough that the components are ‘detached’ [Podsiadlowski, 2014]. In the other  $\sim 50\%$ , the components are close enough to elicit the transfer of mass from one component to the other. In this case, the system is described as ‘interacting’. The characteristic phenomena exhibited by interacting systems provide a unique opportunity for the study of accretion: the gravitational capture of material by a massive object. As will be discussed, accretion is the source of some of the most violent and high-energy interactions in the Universe, from supernovae to active galactic nuclei and astrophysical jets. Even the least massive compact binary configurations, i.e. those containing a white dwarf, are known to launch these jets [Coppejans and Knigge, 2020].

Perhaps the most extreme of these interactions, however, are mergers. Here, the binary orbit shrinks until the two components combine to form a single object in a violent collision. These collisions, along with the preceding inspiral of the system’s components, have been responsible for all current gravitational wave

detections. Perhaps the most important example is the first detection of gravitational waves by LIGO in 2015 [Abbott et al., 2016], in which the inspiralling and consequent merging of two black holes was detected. The importance of gravitational waves to modern astrophysics is discussed in detail by LIGO [2024]. The primary reason is that gravitational waves provide a way to explore the behaviour and properties of astronomical systems that is completely separate from electromagnetic radiation—essentially providing a new ‘sense’ with which to explore these phenomena. Furthermore (and unlike electromagnetic radiation), gravitational waves travel through the Universe essentially unaffected by matter. As a result, they offer an opportunity to study these phenomena with far greater precision and accuracy than would otherwise be possible.

Looking even more broadly at the great unknowns in physics as a whole, an important question still remains regarding the unification of general relativity with quantum theory. The fundamental problem is that gravity has yet to be successfully described in a quantum framework [Kiefer, 2007]. Compact binaries (particularly those containing a neutron star or black hole) offer a unique opportunity to study environments in which neither quantum-mechanical nor strong-field gravitational effects can be ignored [Damour, 2009], and so these systems may hold the key to solving what is arguably the greatest problem in modern physics. Their importance, therefore, cannot be overstated.

However, before delving into the wealth of physics that governs the formation, evolution and behaviour of compact binaries, we must first consider the more simple case of single stars.

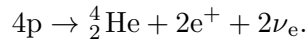
## Chapter 2

# Single Star Evolution

### 2.1 Nuclear Fusion

Every instant of a main sequence star's life is spent struggling against its collapse. Inward gravitational forces are balanced with the thermal pressure generated by fusion in the stellar core, leaving the star in a state of hydrostatic equilibrium.

The majority of the star's life cycle is spent fusing hydrogen into helium, which occurs primarily via the following process:



Here, four protons contained in hydrogen nuclei are fused into one helium nucleus, two positrons and two electron neutrinos via the 'proton-proton chain' [Adelberger et al., 2011]. The rest mass of the resulting  ${}^4_2\text{He}$  nucleus is  $\simeq 0.7\%$  less than the combined mass of the four protons that form it, and this mass is released as light.

### 2.2 Stellar Expansion

It can be shown that in hydrostatic equilibrium,

$$L \propto \frac{\mu^4}{\kappa} M^3 \tag{2.1}$$

where  $L$  and  $M$  are the luminosity and mass of the star, respectively,  $\mu$  is the mean molecular mass, and  $\kappa$  is the average opacity in the star. As more and more hydrogen is fused into helium in the core, the mean molecular weight of the star increases, and the density of free electrons (and hence  $\kappa$ ) decreases. It is then clear from Eq. 2.1 that the luminosity of the star increases with age, inducing an expansion of the

stellar envelope [Kippenhahn et al., 2012].

Expansion of a greater magnitude (and over a significantly shorter timescale) also occurs as a star evolves off of the main sequence. As the star ages and the supply of hydrogen in the core is exhausted, fusion shifts to regions of greater hydrogen abundance outside the core. The thermal pressure drops due to the lack of ongoing fusion in the core, and the gravitational potential causes the core to contract as hydrogen from these bordering regions is drawn in. This then ignites, resulting in an increased rate of thermal radiation and a consequent expansion of the stellar envelope [Iben, 1967]. The result is a red giant, a massively inflated late-stage star of much lower density, with ongoing hydrogen fusion in a shell surrounding the core which is itself fusing helium. As will be discussed more thoroughly below, this state is reached significantly earlier in the most massive stars.

## 2.3 Stellar Winds

Both giants and main sequence stars eject strongly ionised material from their outermost layer through stellar winds [Wood, 2004]. In low to intermediate-mass stars like the Sun, these winds are thought to be driven by interactions in the magnetic field which accelerate particles in its outer layers to such a degree that they escape its gravitational field [Johnstone et al., 2015]. In higher-mass stars, significantly stronger winds are instead driven by radiation pressure resulting from fusion.

## 2.4 Compact Object Formation

Stars on the main sequence and red giant stages can exist for timescales on the order of millions to billions of years. Given that a star can only support hydrostatic equilibrium for as long as it has fuel to burn, its lifetime can be expressed as a ratio of the total available energy from fusion against the rate at which this energy is released:

$$\tau \simeq \frac{E_{\text{tot}}}{L} \tag{2.2}$$

where  $E_{\text{tot}}$  is the total available energy from fusion and  $L$  is the star's luminosity.  $E_{\text{tot}}$  is directly proportional to the mass of the star,  $M$ , since this sets the total amount of fuel available for fusion. In the case of main sequence stars with  $M \lesssim 10 M_{\odot}$ , where  $M_{\odot}$  is the mass of the Sun,  $L$  can be derived from the mass-luminosity relation:

$$L \propto M^a \tag{2.3}$$

where  $3.5 \lesssim a \lesssim 4$  [Duric, 2003]. For more massive stars, this relation flattens to  $L \propto M$ . Combining Eqs. 2.2 and 2.3, we have:

$$\tau \simeq \frac{E_{\text{tot}}}{L} \propto \frac{M}{M^{3.5-4}},$$

and hence

$$\tau \propto M^{-(2.5-3)} \tag{2.4}$$

in the case of typical stars with  $M \lesssim 10 M_{\odot}$ . It is therefore clear that a main sequence star's lifetime is a strongly inverse function of its mass. This relation is not obeyed by red giants due to the differences in their structure and the resulting fusion profile.

In any case, a star's fuel will eventually run out. As fusion ceases, the main sequence phase of the star's life comes to an end as the gravitational force wins. In low-mass stars, this manifests in the shrinking of the core and the expulsion of the majority of the stellar envelope. The fate of high-mass stars is significantly more extreme. As heavier elements are fused in the core, the energy released by fusion decreases. Once iron begins to be formed from the fusion of silicon, the energy released by each reaction is less than the energy required to initiate it. The support provided by fusion rapidly decreases, and the core undergoes a violent collapse.

If and what mechanisms can support the core from further shrinking/collapse depends on the mass of the star. When the formation of a compact object occurs in stars below  $8.5\text{--}10 M_{\odot}$ , the core is supported from further shrinkage by electron degeneracy pressure [Chandrasekhar, 1931]. This is a result of a quantum-mechanical effect—the Pauli exclusion principle—which states that two electrons in the same small volume cannot occupy the same energy state. The star's collapse forces electrons in the core to become increasingly close to one another, pushing them into higher and higher energy levels as the lower levels become full. The increased kinetic energy and momentum of the electrons gives rise to an outwards pressure which supports the core from further collapse [Lamers and Levesque, 2017]. The result is a white dwarf: an extremely dense stellar remnant in which there is no ongoing fusion. Despite the lack of energy production, the core is still extremely hot due to the rapid compression of the highly energetic material that formed it—with the highest mass white dwarfs having initial surface temperatures of over  $10^5$  K [McCook and Sion, 1999].

There is an upper limit, however, to the mass of a white dwarf that can be supported by electron degeneracy pressure. This is the Chandrasekhar limit, with an accepted value of  $M_{\text{ch}} \simeq 1.4 M_{\odot}$ . If a white dwarf reaches a mass greater than this, the core becomes unstable and is destroyed in a Type Ia supernova [Belloni and Schreiber, 2023]. Chandrasekhar also proposed a limit on the density of a white dwarf, based on the two limiting cases of electron degeneracy pressure. These are the non-relativistic and relativistic limits, with the relevance of each being set by the speeds to which the electrons are accelerated. The higher the density of the white dwarf, the more closely the electrons are packed together, and so the greater the magnitude of this acceleration. The key is that in either case, the governing solution is of the form:

$$P \propto \bar{\rho}^n$$

where  $P$  is the generated pressure and  $\rho$  is the average white dwarf density.  $n$  is the polytropic index, with a value of  $\frac{3}{2}$  or 3 in the non-relativistic and relativistic cases, respectively. This allows for the following to be reached, a full derivation for which can be found in CU Boulder [2003]:

$$R \propto M^{\frac{n-1}{n-3}} \tag{2.5}$$

where  $R$  is the white dwarf radius and  $M$  is the white dwarf mass. In the non-relativistic case, with  $n = \frac{3}{2}$ , we then have

$$R \propto M^{-\frac{1}{3}}.$$

From this,

$$\bar{\rho} \propto \frac{M}{R^3} \propto M^2,$$

where  $\bar{\rho}$  is the average white dwarf density. In the non-relativistic case (i.e. when the mass density is low) the density of a white dwarf therefore increases with its mass squared. As the mass (and hence the density) of the white dwarf increases, its electrons become more relativistic and so the second solution ( $n = 3$ ) can no longer be ignored. As  $n$  tends towards 3, the radius of the white dwarf as given by Eq. 2.5 tends to zero. Since  $n$  is dependent on the density and hence the mass of the white dwarf, this occurs at a specific value of  $M$ : the Chandrasekhar limit [Chandrasekhar, 1935].  $M_{\text{ch}}$  therefore also sets an upper limit on the density of a white dwarf, which is found to be close to  $10^7 \text{ g cm}^{-3}$  [Chandrasekhar, 1931]. The formation of a white

dwarf is the expected end result for 95% of stars in our Galaxy [Antunes et al., 2024].

For more massive stars, gravity once again wins and the core instead begins to collapse. The resulting increase in density causes electrons to be captured by protons to form a gas almost entirely comprised of neutrons. This collapse continues until it is halted by an even stronger force: neutron degeneracy pressure. The result is a neutron star, a hotter and even more dense degenerate star. The surface temperature of a newly formed neutron star can be in excess of  $10^7 - 10^8$  K [Geppert, 2016], approximately 2 – 3 orders of magnitude hotter than was noted above for a white dwarf. Similarly, comparing the above upper limit on density for a maximally dense white dwarf with the density of only a typical neutron star ( $\simeq 10^{15}$  g cm $^{-3}$  [Potekhin, 2010]) shows that the latter can easily be  $10^7 - 10^8$  times more dense. For comparison, the central density of the Sun is a mere  $10^2$  g cm $^{-3}$  [Lamers and Levesque, 2017].

However, as is the case for white dwarfs, there is an upper limit on the mass of a stable neutron star. Beyond this limit, not even neutron degeneracy pressure can halt the star's collapse. The result is a further collapse of the core to form a black hole, with recent research suggesting that this occurs at a limit of  $\simeq 2 M_{\odot}$  [Rezzolla et al., 2018]. The collapsing material becomes increasingly dense, warping the local spacetime to such an extent that even light is trapped in a region around it. The radius of the sphere that encloses this region is the Schwarzschild radius, which is around 3 km for a black hole with the same mass as our Sun. The surface of the sphere is known as the black hole's event horizon, beyond which the singularity awaits any visitor.

## Chapter 3

# Compact Binary Formation and Evolution

With an overview of compact object formation from single stars completed, it is now time to explore the focus of this work. The formation of most compact binary systems initially follows the evolution of single stars, with the more massive star in such a system exhibiting a shorter evolutionary timescale (see Eq. 2.4). This star then collapses, leaving a compact object and a main sequence companion. Other possible formation channels include mergers of components within higher-order systems and dynamical interactions in regions of high stellar density. However, the contribution to observed compact binary populations from the latter channels is expected to be insignificant. This is largely due to the lower abundance of higher-order systems and the infrequency of strong dynamical interactions outside dense stellar regions. Nonetheless, they are still occasionally required to explain the formation of certain systems which could not have been formed via the standard stellar evolution pathway [Belloni and Schreiber, 2023].

As noted in the introduction, the orbital separation in around 50% of compact binary systems is large enough that the components are non-interacting. This is typically the case for systems with an orbital separation of  $\gtrsim 5 - 10$  au. In this case, both components simply evolve as if they were single stars. However, for systems with a small enough separation, the evolution of the higher-mass star can drive the binary into interactions involving the transfer of mass. In this case, the accreting object (i.e. the object to which mass is being transferred) is referred to as the accretor, and the star from which this mass originates is referred to as the donor. Mass transfer affects the structure of both stars and the configuration of the system as a whole, and so it is the driving mechanism behind the evolution of interacting

systems [Podsiadlowski, 2014].

### 3.1 Mass transfer through Roche Lobe Overflow

The Roche lobe is defined as the last equipotential geometry beyond which any stellar mass is no longer bound to it by the star's gravity. Both stars in an interacting binary will therefore have their own Roche lobes, which meet at the inner Lagrangian point where the effect of gravity from both stars is felt equally. If a star in an interacting binary overflows its Roche lobe, the transfer of mass through the inner Lagrangian point is initiated (Fig. 3.1) [Lubow and Shu, 1975]. There are two causes of Roche lobe overflow: Roche lobe shrinkage and stellar expansion.

The former occurs when the orbital separation of the binary is reduced as a result of angular momentum loss from the system. As the orbital separation decreases, the donor feels the effect of the accretor's gravity more strongly—while the strength of its own gravity is unchanged. Material in the donor's envelope is therefore less bound to it at a given radius, which is by definition a reduction in the size of its Roche lobe. Since the two binary components are equidistant from one another, the ratio of their gravitational field strengths is simply the ratio of their masses. The Roche lobe radius therefore depends only on the mass ratio of the two binary components and their separation (Eq. 1.3, Podsiadlowski [2014]).

The latter occurs through the expansion of the companion's stellar envelope via Eq. 2.1, or its evolution off of the main sequence. In either case, mass transfer is only initiated if the expansion is sufficient to cause Roche lobe overflow. For a companion of a given mass, the likelihood of this condition being met is set by the closeness of the binary configuration. It is important to note that as the density of each component has a significant impact on the likelihood of it overflowing its Roche

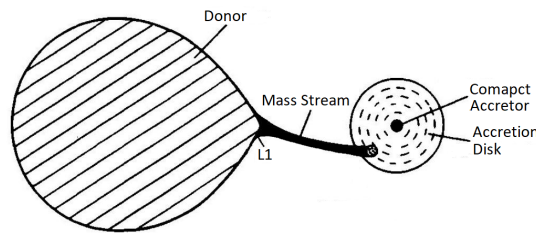


Figure 3.1: An interacting compact binary in which the donor is overflowing its Roche lobe, leading to the transfer of mass through the inner Lagrangian point (L1) and the formation of an accretion disc. Adapted from Warner [1995].

lobe, the donor is not necessarily the component of lower mass. This is particularly relevant in compact binaries, in which the difference in the densities of the binary components can be extremely large.

## **3.2 Mechanisms for the Loss of Orbital Angular Momentum**

From the above discussion, it is clear that either method of mass transfer initiation requires a previous or ongoing period of orbital angular momentum loss. There are two primary mechanisms through which this occurs in a binary system: gravitational wave radiation and magnetic braking. It is important to note that since neither of these mechanisms is restricted to interacting systems, both offer pathways for a non-interacting system to eventually become interacting.

### **3.2.1 Gravitational Wave Radiation**

Following their original prediction from special relativity, gravitational waves are now understood to be a key driver of angular momentum loss in binary systems. The emission of gravitational waves is expected to occur in any system in which a mass is either accelerating or is non-symmetric and rotating [Flanagan and Hughes, 2005]. In binary systems, this process carries away energy and orbital angular momentum, with the large masses and short orbital periods of compact binaries making them a significant source of gravitational waves. As noted previously, gravitational waves were first detected in 2015 by the LIGO Scientific Collaboration and the Virgo Collaboration [Abbott et al., 2016].

### **3.2.2 Magnetic Braking**

As discussed in the section on single-star evolution, stars drive away ionised particles through processes that depend on the stellar mass. This material can then be captured by the star's magnetic field lines as it travels outwards, with coupling maintained up to the Alfvén radius. Beyond this, gravitational and magnetic forces are no longer strong enough to control the motion of the plasma, and so it is ejected—carrying away energy and angular momentum. This mechanism is responsible for the gradual spin-down of single stars but is equally applicable to stars in binary systems. In some cases, magnetic braking may dominate over gravitational wave radiation as the primary mechanism for the loss of orbital angular momentum [Knigge et al., 2011]. Since the effect of magnetic braking increases with the

magnetic field strength (see Eq. 1 in Meynet et al. [2011]), this is particularly likely to be the case in systems with a strong magnetic field. This is also true for systems with a large orbital separation, in which both components experience a lower magnitude of acceleration and therefore lose less energy to the emission of gravitational waves. A thorough review of this mechanism can be found in Li [1994].

### 3.3 Conservation in Mass Transfer

It is clear from magnetic braking that the loss of mass from a system can be a significant driver of angular momentum loss. In interacting systems, an important consideration is therefore the amount of mass lost by the donor which is consequently captured by the accretor. Two fundamental regimes for mass transfer describe the conservation of the system’s mass, and therefore its total angular momentum. In the following, properties of the accretor and donor will be denoted by the subscripts ‘a’ and ‘d’, respectively.

#### 3.3.1 Conservative Mass Transfer

Conservative mass transfer describes the case where the system does not lose any of its total mass during the transfer process, i.e.  $\dot{m}_a = -\dot{m}_d$ . In this case, it is often also assumed that the total angular momentum of the system is conserved, i.e.  $\dot{J}_T = 0$ .

#### 3.3.2 Non-conservative Mass Transfer

Non-conservative mass transfer describes the opposite case, where mass is lost from the system during transfer (i.e.  $\dot{m}_a < -\dot{m}_d$ ). The system’s total angular momentum is therefore not conserved, i.e.  $\dot{J}_T < 0$ .

When mass transfer is assumed to be conservative, it is essentially inevitable that the transfer is only quasi-conservative in reality (i.e. an insignificant amount of the system’s total mass/angular momentum is lost during transfer). This is particularly likely to be the case when the transfer of mass is dominated by the gravitational capture of the companion’s stellar wind [Blondin and Owen, 1997]. For material that is driven towards the accretor, the resulting mass transfer can generally still be considered conservative. However, this can not be said for the entire wind, which is expected to be emitted largely isotropically [Rosen, 2022]. Mass transfer in this case is therefore clearly *not* conservative. Furthermore, it has already been noted that gravitational wave radiation (which does not require the system to lose mass

to operate) is expected to occur in all binaries. Regardless of the conservation of mass, the total angular momentum of any binary system is therefore necessarily not conserved.

### 3.4 Orbital Evolution driven by Mass Transfer

The evolution of angular momentum in a binary system ( $\dot{J}$ ) can be described in terms of the orbital separation ( $a$ ) and the masses of the accretor and donor ( $M_a$  and  $M_d$ , respectively) as

$$\frac{\dot{J}}{J} = \frac{1}{2} \left( \frac{\dot{a}}{a} + 2 \frac{\dot{M}_a}{M_a} + 2 \frac{\dot{M}_d}{M_d} - \frac{\dot{M}_a + \dot{M}_d}{M_a + M_d} \right) \quad (3.1)$$

where  $\dot{x}$  denotes the first time derivative of  $x$ . Here, it is assumed that the binary orbits are circularised (i.e. of zero eccentricity) and that the contribution to the system's total angular momentum from the rotation of its components is negligible [Pols, 2015]. Of course, this is not always the case—but it is a useful assumption for the sake of simplicity. It is important to note that  $\dot{J}$  represents any loss of angular momentum from the system, either from mass loss or via other processes such as those discussed previously.

#### 3.4.1 Orbital Evolution under Conservative Mass Transfer

In the case of conservative mass transfer, where  $\dot{J} = 0$  and  $\dot{M}_a = -\dot{M}_d$ , Eq. 3.1 simplifies to

$$\frac{\dot{a}}{a} = 2 \left( \frac{M_d}{M_a} - 1 \right) \left( \frac{\dot{M}_d}{M_d} \right). \quad (3.2)$$

This equation is of great importance, as it gives a simple condition for orbital expansion/shrinkage as a result of mass transfer. Since  $\dot{M}_d < 0$ , the sign of  $\frac{\dot{a}}{a}$  is only dependent on the mass ratio  $q = \frac{M_d}{M_a}$ . We therefore have the following conditions:

For  $q > 1 \rightarrow \frac{\dot{a}}{a} < 0$ , the orbit shrinks.

For  $q < 1 \rightarrow \frac{\dot{a}}{a} > 0$ , the orbit expands.

#### 3.4.2 Orbital Evolution under Non-conservative Mass Transfer

As noted previously, the assumption that total mass and angular momentum are conserved cannot often be made in real systems. It is therefore important to also

consider the opposite case. The need to consider the loss of angular momentum and mass quickly complicates the situation, so all that will be discussed here are the parameterisations used in its description. The following can be derived in the non-conservative case:

$$\frac{\dot{a}}{a} = -2 \frac{\dot{M}_d}{M_d} \left[ 1 - \beta \frac{M_d}{M_a} - (1 - \beta) \left( \gamma + \frac{1}{2} \right) \frac{M_d}{M_d + M_a} \right]. \quad (3.3)$$

Here,  $\beta$  parameterises the amount of mass lost from the system during transfer:

$$\dot{M}_a = -\beta \dot{M}_d.$$

Similarly,  $\gamma$  parameterises the loss of angular momentum:

$$\frac{\dot{J}}{\dot{M}_a + \dot{M}_d} = \gamma \frac{J}{M_a + M_d}.$$

While the equation describing this situation (Eq. 3.3) is still relatively simple, the complexity arises from the need to obtain accurate values of  $\beta$  and  $\gamma$ . Any reasonable estimate of these parameters will depend heavily on the individual system and the processes that drive mass transfer and/or angular momentum loss. This quickly becomes a difficult problem [Pols, 2015].

### 3.5 Stability of Mass Transfer

The stability of mass transfer is one of the primary parameters that determine an interacting binary's evolutionary pathway and is set by the response of the donor's radius and Roche lobe to its mass loss [Belloni and Schreiber, 2023]. Once mass transfer has begun, the process can only be stable for as long as the donor can shrink at a rate equal to or greater than that of its Roche lobe. If this condition is not met, the transfer of mass becomes a runaway process as  $|\dot{m}|$  increases as a result of ongoing mass loss. The following is largely a summary of the information found in Pols [2015], which may be read for further information.

To provide a more quantitative description, we introduce the mass-radius response exponents:

$$R_{\text{RL}} \propto M_d^{\zeta_{\text{RL}}} \quad R_d \propto M_d^{\zeta_d}$$

where  $R_d$  and  $R_{\text{RL}}$  are the radii of the donor and its Roche lobe radius, respectively,  $M_d$  is the mass of the donor, and the mass-radius response exponents for the donor and its Roche lobe are given by:

$$\zeta_{\text{RL}} \equiv \frac{d \log R_{\text{RL}}}{d \log M_{\text{d}}} \quad \zeta_{\text{d}} \equiv \frac{d \log R_{\text{d}}}{d \log M_{\text{d}}} \quad .$$

These exponents parameterise the rate at which the donor and its Roche lobe shrink as a response to mass loss, which allows us to write the previously stated condition for stability as:

$$\zeta_{\text{d}} \geq \zeta_{\text{RL}} \rightarrow \text{stable mass transfer}$$

$$\zeta_{\text{d}} < \zeta_{\text{RL}} \rightarrow \text{unstable mass transfer}$$

### 3.5.1 Response of the Donor

However, the use of a single exponent to describe the rate of donor shrinkage is an oversimplification. When a star loses mass, it must adjust its structure to restore its previous state of hydrostatic *and* thermal equilibrium. These occur on two greatly different timescales: the dynamical timescale ( $\tau_{\text{dyn}}$ ) and the thermal timescale ( $\tau_{\text{KH}}$ ), respectively. The dynamical timescale is significantly shorter than the thermal timescale, i.e.  $\tau_{\text{dyn}} \ll \tau_{\text{KH}}$ , and so the dynamical response of the donor to the onset of mass transfer can be considered adiabatic (i.e. there is assumed to be no local heat transfer). In light of this, a new mass-radius exponent is introduced:

$$\zeta_{\text{ad}} \equiv \left. \frac{d \log R_{\text{d}}}{d M_{\text{d}}} \right|_{\text{ad}}$$

with a corresponding condition for dynamical stability of mass transfer,  $\zeta_{\text{RL}} \leq \zeta_{\text{ad}}$ . For dynamically stable mass transfer, the donor must therefore shrink to a radius smaller than that of its Roche lobe within  $\tau_{\text{dyn}}$  and restore its state of hydrostatic equilibrium. A thermal equilibrium determined by the star's mass, composition and evolutionary stage is then recovered over the significantly longer timescale of  $\tau_{\text{KH}}$ . The corresponding mass-radius exponent in the thermal timescale is then given by

$$\zeta_{\text{eq}} \equiv \left. \frac{d \log R_{\text{d}}}{d M_{\text{d}}} \right|_{\text{eq}},$$

with the now familiar stability condition of  $\zeta_{\text{RL}} \leq \zeta_{\text{eq}}$ . This improved description gives rise to three regimes of mass transfer:

1. Stable mass transfer,  $\zeta_{\text{RL}} \leq \zeta_{\text{ad}}$  and  $\zeta_{\text{RL}} \leq \zeta_{\text{eq}}$

In this case, the donor settles into a hydrostatic and thermal equilibrium without initially filling its Roche lobe. Mass transfer is then only initiated by either expansion of the stellar envelope due to ageing/evolution, or Roche

lobe shrinkage through the loss of orbital angular momentum. In this regime, mass transfer therefore takes place either on the evolutionary timescale of the donor,  $\tau_{\text{nuc}}$ , or the timescale of orbital (and hence Roche lobe) shrinkage.

2. Stable mass transfer on  $\tau_{\text{KH}}$ ,  $\zeta_{\text{eq}} < \zeta_{\text{RL}} \leq \zeta_{\text{ad}}$

Here, mass transfer is still dynamically stable (as  $\zeta_{\text{RL}} \leq \zeta_{\text{ad}}$ ), but is driven by the expansion of the donor due to thermal reconfiguration. Despite not being in a state of thermal equilibrium, the resulting mass transfer is stable and self-regulating ( $\dot{M}$  decreases/increases to maintain stability).

3. Unstable mass transfer,  $\zeta_{\text{RL}} > \zeta_{\text{ad}}$

As noted above, unstable mass transfer occurs when the donor is not able to shrink faster than its Roche lobe, resulting in a runaway process of increasing mass loss.

Together, these three regimes describe the response of the donor to mass transfer. It is important to note that more than one of these regimes will likely be exhibited by a given system as it evolves.

### 3.5.2 Response of the Roche Lobe

When describing the response of the Roche lobe to mass loss, the aforementioned regimes of conservative/non-conservative mass transfer are once again relevant. In the case of conservative mass transfer, the response of the Roche lobe ( $\zeta_{\text{RL}}$ ) depends almost entirely on the binary mass ratio  $q = \frac{M_{\text{d}}}{M_{\text{a}}}$ , where  $M_{\text{d}}$  and  $M_{\text{a}}$  are the masses of the donor and the accretor, respectively. The stability condition can then be written in terms of a critical mass ratio,  $q_{\text{c}}$ . The case of non-conservative mass transfer is less simple as  $\zeta_{\text{RL}}$  then also depends on the amount of outgoing mass that is lost from the system, and any mechanisms driving this mass loss. As it did when discussing orbital evolution (Eq. 3.3), this complicates the estimation of  $\zeta_{\text{RL}}$  significantly. It was previously noted that mass transfer is very rarely fully conservative in reality, and so the stability of mass transfer is often an incredibly complex problem.

Now that the various regimes and modes of mass transfer have been discussed, our focus can shift to their structural and evolutionary consequences.

## 3.6 Common Envelope Evolution

Initially proposed as a mechanism for the formation of cataclysmic variables (a subtype of compact binaries, more on these later), a phase of common envelope evo-

lution (henceforth CEE) can be initiated in two ways: the unstable decay of a binary orbit, or the evolution of a binary component off of the main sequence [Paczynski, 1976]. The process driving the decay in the former is often considered to be one of unstable mass transfer [Ivanova et al., 2013b]. As has been already discussed, unstable mass transfer occurs when the Roche lobe shrinks faster than the adiabatic response of the donor as a result of its mass loss (see regime three of mass transfer stability). This leads to a runaway process in which the rate of mass loss from the donor rapidly increases. If the rate of mass transfer exceeds the rate at which it can be accreted, the result is a common envelope (henceforth CE): a large cloud of material which envelopes both stars. This occurs most commonly in systems where the donor is a giant or supergiant with a convective envelope, as these stars often expand as a result of mass loss [Podsiadlowski, 2014]. Additionally, donors of greater mass than their companion are more likely to exhibit unstable mass transfer due to the response of the orbit in Eq. 3.2. The latter path to the formation of a CE occurs when a main sequence binary component evolves into a red giant. If the expansion of the companion is large enough, the secondary component will be engulfed in its stellar envelope [Ivanova et al., 2013a].

During the CE phase, the binary components continue to orbit one another—losing energy and angular momentum to the envelope. This tightens the orbit of the binary significantly and, if enough energy is gained by the envelope, may cause the envelope to be ejected [Ivanova et al., 2020]. This gives rise to two fundamental pathways through the CE phase:

1. The envelope is ejected before the inspiralling components merge, stopping orbital shrinkage. The system emerges in a significantly tightened configuration. The system consequently orbits on a much shorter period on the order of hours to days, and the companion is relatively unchanged owing to the brevity of the CE phase prior to ejection [Podsiadlowski, 2014]. The small orbital separations observed in many compact binaries imply that the compact component’s giant progenitor was orders of magnitude larger than the current system, and therefore that the binary experienced significant orbital shrinkage during this component’s formation [Belloni and Schreiber, 2023; Ivanova et al., 2013a]. CEE is therefore accepted as an essential process in the formation of close, short-period compact binaries [Ivanova et al., 2013a; Taam and Sandquist, 2000].
2. The envelope is not ejected, and the binary components continue to spiral in until they collide. The result of this is the merging of the binary components to

form a single star with increased mass, and often a rapid initial spin due to the transfer of orbital angular momentum into the spin angular momentum of the merger remnant. If the star formed by the merger exceeds the relevant mass limit, the merger may also initiate further evolution through collapse [Ivanova et al., 2020]. As noted in the introduction, mergers are key sources of many extreme astrophysical phenomena, such as gamma-ray bursts [Belczynski et al., 2006] and gravitational waves. The aforementioned first detection of gravitational waves by LIGO was the result of a black hole–black hole merger.

Despite the clear importance of CEE, physically accurate and detailed models are severely lacking. Of course, a condition separating the two above outcomes would be of great utility for predicting a system’s evolution. However, as noted in Marchant et al. [2021], such a condition is not yet known. Furthermore, the lack of a complete physical picture of CEE means that existing models rely on the use of often poorly defined free parameters. This problem is only worsened by the fact that the exact values of these parameters are also expected to differ greatly between systems [Ivanova et al., 2013a]. In fact, Ivanova et al. [2013a] states that “common envelope evolution is one of the most important unsolved problems in stellar evolution, and is arguably the most significant and least-well-constrained major process in binary evolution”.

### 3.7 Accretion Disc Formation

So far the accretion geometry, i.e. the path taken by infalling material, has not been considered. The most simple configuration would be a radial inflow of material from the donor, where the material has been assumed to have zero angular momentum. In reality, however, this is rarely the case. As material with non-zero angular momentum falls towards the accretor, it begins to rotate around it rather than falling directly inward—being accelerated to supersonic speeds as it leaves the inner Lagrangian point. The infalling material can therefore be considered as approximately following the path of a free particle [Spruit, 2014]. When these supersonic particle streams are decelerated, usually by intra-stream collisions, shocks develop [Caditz, 1998]. These shocks propagate outwards as waves that heat and compress the inflowing material, further increasing the frequency of collisions. As a result, angular momentum and energy are both in constant exchange among the orbiting particles. Angular momentum is conserved while energy is dissipated via collisions, and so the largely random paths eventually settle into the lowest-energy orbit: a ring [Spruit, 2014]. The radius of this ring is the circularisation radius, which is approximately

equal to the radius of a Keplerian orbit of zero eccentricity which would have the same angular momentum per unit mass as the infalling material [El Mellah et al., 2019]. Tidal forces resulting from the gravitational field and rotation of the accretor align this ring with the rotational axis where, if the ring exhibits sufficient viscosity, it then spreads inwards and outwards radially to form a disc. Friction due to gravity and differential rotation in the disc heats the material significantly, causing it to travel inwards as it loses angular momentum. As it does so, it releases its gravitational potential energy which—along with the heating of the material—makes accretion discs extremely luminous [Lewin and van der Klis, 2006]. The structure and behaviour of an accretion disc can provide key insight into the properties of the binary system in which it was formed and so, along with their clear importance to binary evolution, accretion discs are also of great importance to observational astronomy.

### 3.8 X-rays and the Boundary Layer

The boundary layer, a region between the accretor and the inner region of its disc, is of fundamental importance to the evolution of compact binary systems. In addition to its role as a mediator of the transfer of mass and angular momentum between the binary components [Popham and Narayan, 1995], the boundary layer is also a significant emission region: in non-rotating systems, this region can be responsible for up to half of the total luminosity produced via accretion [Popham and Narayan, 1995]. The small size of the boundary layer causes it to dominate emission at high energies, which is in no small part responsible for the significant X-ray emission observed in many compact binary systems. This X-ray emission is often split into two (not well-defined) types: ‘hard’ and ‘soft’ X-rays. Hard X-rays are emitted by extremely hot material with a typical temperature of  $\simeq 10^7 - 10^8$  K. These X-rays are therefore very energetic ( $\gtrsim 10$  keV) and hence highly penetrative. Soft X-rays are emitted from significantly cooler material ( $\simeq 10^6$  K), and are therefore less energetic ( $\lesssim 10$  keV) and more easily absorbed. The contribution of either to a system’s total luminosity in X-rays largely depends on the optical thickness of the emission region, and hence on the rate of mass transfer. For low accretion rates of  $\lesssim 10^{-10} M_{\odot} \text{ yr}^{-1}$ , the boundary layer is optically thin and hence significantly hotter; the contribution from hard X-rays increases. If the mass accretion rate is instead much larger, the boundary layer becomes optically thick and consequently cools to temperatures that favour soft X-ray emission [Hertfelder et al., 2013].

### 3.9 Accretion as a Source of Energy

It has been established that in addition to accretion's role as a driver of interacting binary evolution, it is also a significant source of energy. However, it would be useful to place this in context by providing a more quantitative comparison to the other primary mechanism of energy production in stars: fusion. Due to the equivalence of mass and energy, the key parameter to consider here will be the efficiency of conversion: the fraction of input mass that is radiated as heat. This is given by:

$$\eta = \frac{E}{mc^2} \quad (3.4)$$

where  $E$  is the released energy,  $m$  is the rest mass of the material and  $c$  is the speed of light [Fabian, 2009].

#### 3.9.1 The Efficiency of Fusion

In the earlier section on single stars, it was noted that  $\simeq 0.7\%$  of the input mass of hydrogen is released as energy during fusion. By definition, this sets the efficiency of the nuclear fusion of hydrogen at  $\simeq 0.7\%$ . It was also noted that this efficiency decreases with the fusion of heavier elements, and so this is in fact the maximum possible efficiency of fusion in stars.

#### 3.9.2 The Efficiency of Accretion

The gravitational potential energy released by the accretion of material (i.e. by a given mass falling into a body due to gravitational capture) is given by

$$\Delta E_{\text{acc}} = \frac{GMm}{R} \quad (3.5)$$

where  $G$  is the gravitational constant,  $M$  and  $R$  are the mass and radius of the accretor, respectively, and  $m$  is the mass of the infalling material. Most of this energy is expected to be released via radiation processes [Juhan et al., 2002]. Combining Eqs. 3.4 and 3.5, we acquire the accretion efficiency:

$$\eta = \frac{GM}{c^2 R} \quad (3.6)$$

where all terms have been defined previously. From this, it is clear that the efficiency of accretion only depends on the ratio of the accretor's mass and radius—i.e. its compactness. Considering the case of an average neutron star of mass  $M = M_{\odot}$  and radius  $R = 10$  km, Eq. 3.6 gives an efficiency of  $\simeq 15\%$ . The efficiency of

accretion onto a black hole is made more complicated by the presence of an event horizon but is found to be  $\simeq 6\%$  for a non-rotating black hole [Thorne, 1974]. The distinction of a *non-rotating* black hole is actually an extremely important one, as the accretor’s spin (which is not taken into account in Eq. 3.6) has a significant effect on the accretion efficiency. In the case of a neutron star of maximally fast spin, the efficiency of accretion can be as high as 67% [Sibgatullin and Sunyaev, 2000]. Similarly, the efficiency of accretion onto a black hole of maximal spin can reach up to 32% [Thorne, 1974]. In any case, comparing the derived accretion efficiencies to that of fusion clearly shows accretion onto a neutron star or black hole to be a significant source of energy.

When considering interacting white dwarf binaries, however, this conclusion is not so simple. An average white dwarf with a mass  $M = M_\odot$  and a radius  $R = 7000$  km [Lamers and Levesque, 2017] in Eq. 3.6 suggests an efficiency of only 0.02%–35 times less than that of the nuclear fusion of hydrogen. However, just like neutron stars and black holes, white dwarfs do not actively produce any energy through nuclear fusion. Despite its limited efficiency, accretion therefore still stands as the primary means of energy production in interacting white dwarf binaries.

### 3.9.3 The Eddington Limit

In the above, it has been implicitly assumed that a compact object can accrete material from its companion without limitation. However, a limit does exist. The Eddington limit sets the maximum luminosity (the Eddington luminosity) of a star in hydrostatic equilibrium. Assuming spherical symmetry:

$$L_{\text{Eddington}} = \frac{4\pi GMc}{\kappa}$$

where  $G$  is the gravitational constant,  $c$  is the speed of light,  $M$  is the mass of the star, and  $\kappa$  is the electron scattering opacity [Sanyal et al., 2015]. Radiation propagating within the star is prone to scattering by free electrons, and so  $\kappa$  is set by the free electron density. If the rate of mass transfer in a given system is sufficiently large to generate flux in excess of the Eddington luminosity, the accretion efficiency is consequently lowered by radiation-driven mass loss away from the accretion surface (see Owocki et al. [2004] for a thorough review). The limiting rate of mass transfer is known as the Eddington mass-accretion rate [Podsiadlowski, 2014] and is an important indicator of whether a system’s mass transfer can be considered conservative. It is worth noting that we have said here that the Eddington luminosity can be exceeded, despite its definition as an *upper limit*. So-called super-Eddington

accretion is indeed possible and is thought to be caused by a non-spherical accretion geometry or various instabilities, although the exact details of this process are not well-understood [Brightman et al., 2019].

With the primary mechanisms that drive the formation and evolution of compact binaries illuminated, we can now explore the various kinds of systems that arise. The initial focus will be on compact binaries containing a white dwarf accretor.

## Chapter 4

# White Dwarf Binaries

### 4.1 Formation Channels

Figure 4.1 shows the major formation channels for white dwarf binaries (for those arising from a more massive initial configuration, see Fig. 5.1). The initial binary depicted here (a) consists of a more massive primary star (the leftmost star in all stages), which consequently evolves off of the main sequence faster than its lower mass companion to form a red giant. The resulting expansion of the primary component’s stellar envelope initiates mass transfer via Roche lobe overflow (a  $\rightarrow$  b), but it is important to note that the evolution of the donor in this stage is not necessary; the same state could be achieved through Roche lobe shrinkage. We then see the importance of our previous considerations of mass transfer stability.

For dynamically stable mass transfer (b  $\rightarrow$  c), the system remains stable on a timescale set by the response of the orbit to mass loss (Eqs. 3.2 and 3.3). If the system’s response to mass transfer is to decrease its orbital separation, the result is a close binary in which the core of the primary star has shrunk to form a white dwarf (c  $\rightarrow$  g). In the opposite scenario, the orbital separation increases until neither component fills its Roche lobe. In this case, the system is ‘detached’ and mass transfer can only occur through the significantly slower mechanism of gravitational capture of the stellar wind (c  $\rightarrow$  e). If the timescale for significant orbital angular momentum loss is sufficiently short, it may once again be observed as a close white dwarf–main sequence binary (e  $\rightarrow$  g). Failing this, fusion in the secondary eventually ceases and, as  $M_1 \gtrsim M_2$ , the system becomes a wide, double-degenerate white dwarf–white dwarf binary (e  $\rightarrow$  h).

For dynamically unstable mass transfer (b  $\rightarrow$  d), a CE phase is initiated following rapid orbital shrinkage from runaway mass loss. If the envelope is ejected,

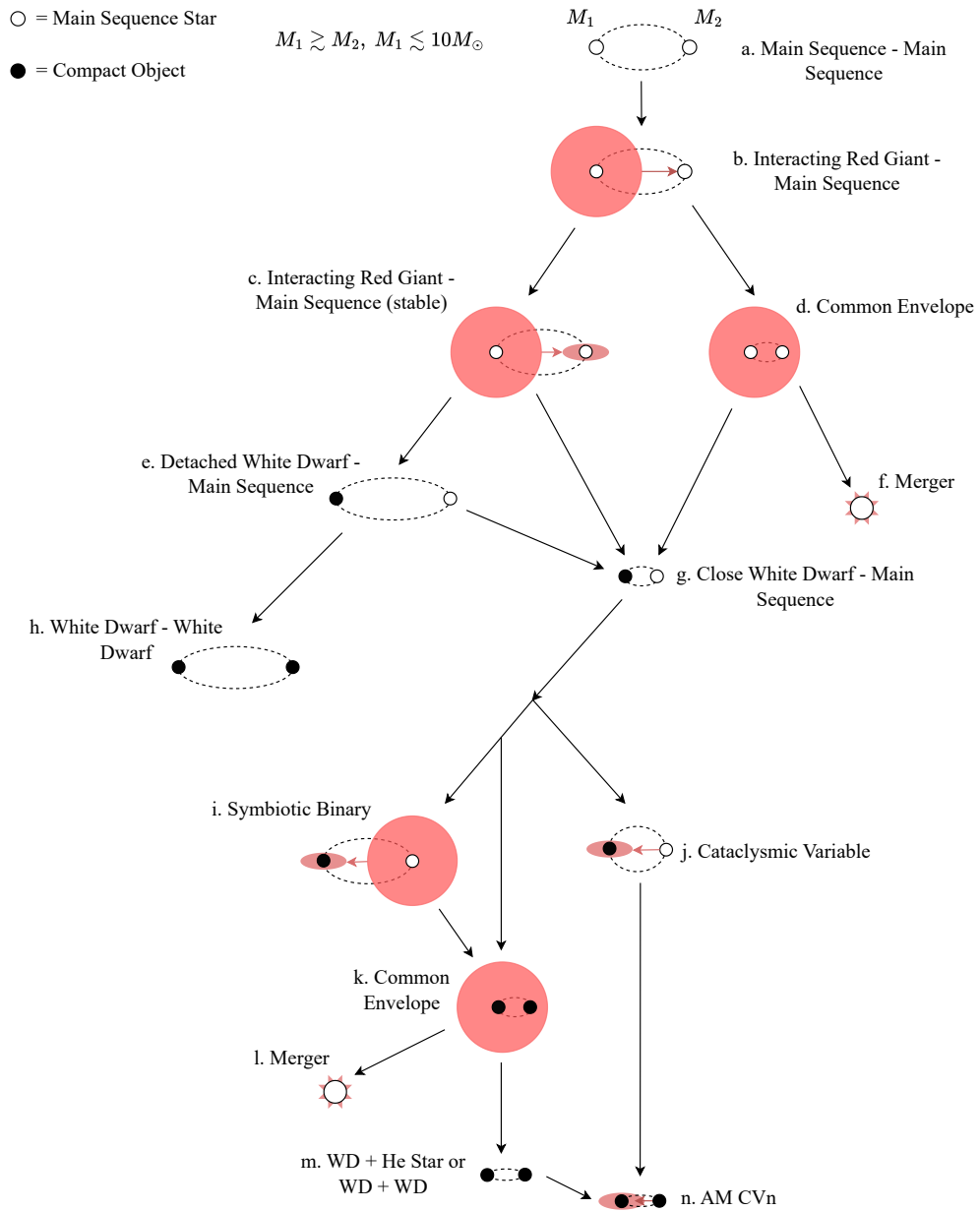


Figure 4.1: Possible evolutionary pathways of a main sequence–main sequence binary to form various types of compact binaries. The leftmost star in the initial binary configuration is more massive and hence evolves on a shorter timescale. Both stars have an initial mass  $\lesssim 10 M_\odot$ , and arrows denote transitions between stages of evolution. Information adapted from [Belloni and Schreiber, 2023].

orbital shrinkage is halted and a significantly tightened binary emerges. Fusion in the red giant eventually ceases, and a white dwarf–main sequence binary is born (d  $\rightarrow$  g). If the envelope is not ejected, orbital shrinkage continues until the two

components ultimately collide—a merger ( $d \rightarrow f$ ). Much like the initial onset of mass transfer, the period of unstable interaction from which a CE phase arises can be initiated either by Roche lobe shrinkage (in this case as a response to mass loss) or by the evolution of the primary. In most cases, any further evolution then stems from the now-familiar configuration of a close (near-interacting) white dwarf–main sequence binary ( $g$ ).

If the timescale for nuclear evolution of the secondary is sufficiently shorter than the timescale for orbital angular momentum loss, a symbiotic binary is born as the secondary evolves into a red giant without engulfing the white dwarf ( $g \rightarrow i$ ). For dynamically stable mass transfer, the timescale on which the system remains in this configuration is once again set by the response of the orbital separation to mass transfer.

If the mass transfer is instead dynamically unstable, a second CE phase is initiated following rapid orbital shrinkage ( $i \rightarrow k$ ). Again, it is important to remember that a second phase of CEE could also have been initiated were the orbit sufficiently close at the time of the secondary’s evolution—bypassing the formation of a symbiotic binary ( $g \rightarrow k$ ). If the system survives the resulting CE phase by ejecting the envelope, the result is a white dwarf–evolved secondary binary ( $k \rightarrow m$ ). Here, an ‘evolved secondary’ is either a helium star (the remains of a formerly massive star that has lost its hydrogen-rich envelope) or a white dwarf. If the envelope is not ejected, the components spiral in before colliding in a merger ( $k \rightarrow l$ ). Assuming the system survives the second phase of CEE and the secondary completes its evolution to form a white dwarf, the system becomes an AM CVn as mass transfer is initiated ( $m \rightarrow n$ ).

We return now to the alternative case in the original configuration of a close white dwarf–main sequence binary ( $g$ ). If the orbit instead shrinks sufficiently on a timescale shorter than the secondary’s nuclear timescale, a cataclysmic variable is born as mass transfer onto the white dwarf is initiated via Roche lobe shrinkage of the secondary ( $g \rightarrow j$ ). Once fusion eventually ceases in the secondary and it collapses to form a white dwarf, the endpoint of an AM CVn system is once again reached ( $j \rightarrow n$ ).

As was noted in the section on single stars, any white dwarf can only remain stable for as long as its mass remains below the Chandrasekhar limit. Many of the various forms of accreting white dwarf binary are therefore expected to be potential progenitors to Type Ia supernovae. See [Belloni and Schreiber, 2023] for a full review.

## 4.2 Symbiotic Stars

With an understanding of the main evolutionary pathways from which white dwarf binaries arise, we can now look at these systems in greater detail. The focus here will largely be on cataclysmic variables, but we should first consider the result of the alternative pathway: symbiotic binaries.

As established in the above discussion, symbiotic systems are wide binaries in which a compact primary accretes from an evolved secondary. Figure 4.1 only shows the formation of a symbiotic binary containing a white dwarf, but similar systems have also been found to support a neutron star accretor [Bozzo et al., 2022]. In this case, the system is known as a symbiotic X-ray binary. The evolved secondary is a typical red giant [Mikolajewska, 2002] in approximately 80% of symbiotic systems, with the remaining 20% being primarily Mira variables. These are cool red giants which emit radial pulsations, brightening by up to 2.5 mag on a period of 150 – 1000 d [Mattei, 1997], with a typical mass of  $\lesssim 2 M_{\odot}$  [Ireland et al., 2004]. Symbiotic systems typically have an orbital period on the order of hundreds to thousands of days and, like many other white dwarf binaries, are expected progenitors of Type Ia supernovae [Luna et al., 2013]. The rate of accretion onto the compact primary can be large enough to support stable nuclear burning on its surface, with the energy released by this process being radiated as X-rays. Accretion is rarely driven by Roche lobe overflow in these systems, instead resulting from gravitational capture of the giant companion’s stellar wind [Belloni and Schreiber, 2023]. As a result, the typical accretion rate in these systems is low:  $10^{-11} - 10^{-7} M_{\odot} \text{ yr}^{-1}$  [Lima et al., 2024].

## 4.3 Cataclysmic Variables

### 4.3.1 Properties and Evolution

Cataclysmic variables (henceforth CVs), named after the violent interactions that they exhibit, are the most abundant form of interacting compact binaries [Belloni and Schreiber, 2023]. Figure 4.1 shows the formation pathways that lead to a CV, with the majority of these systems being formed from a CE phase in which the core of a red giant shrinks to a white dwarf in a tight binary. Many of the resulting systems are initially in a detached state upon ejection of the envelope, until mass transfer is initiated through orbital shrinkage. The system then evolves as a CV, with magnetic braking and gravitational wave radiation further decreasing the orbital separation (and hence the orbital period) [Warner, 1995].

A key manifestation of the angular momentum-driven evolution of a CV is the existence of a period gap and a period minimum.

#### 4.3.1.1 The Period Gap

The period gap—an observed lack of CVs with orbital periods in the range  $2 \sim 3$  h—can be explained through the mechanism driving angular momentum loss: magnetic braking. As noted previously, the orbital period of a CV continues to decrease after its initial formation due to magnetic braking. Once the orbital period reaches  $\simeq 3$  h, the effect of magnetic braking is thought to be significantly reduced by a reconfiguration of the donor’s magnetic field [Rappaport et al., 1983]. The donor, which is larger than it would be at thermal equilibrium due to prior angular momentum loss, then shrinks back to its equilibrium radius and mass transfers ceases as it no longer fills its Roche lobe. Since the system is no longer interacting during this phase, it will not be observed as a CV. The range of orbital periods for which this occurs is largely set by analysis of known CV populations, with recent observations finding a significant lack of systems in the period range of  $2.15 \lesssim P_{\text{orb}} \lesssim 3.18$  h [Knigge, 2006]. Gravitational wave radiation supersedes magnetic braking as the dominant driver of angular momentum loss as systems tend towards shorter orbital periods, resulting in much slower evolution. The separation (and hence the orbital period) in these systems continues to decrease until mass transfer is reinstated and the system re-emerges as a CV with a period below the period gap [Knigge et al., 2011].

#### 4.3.1.2 The Period Minimum

As discussed in Paczynski and Sienkiewicz [1983], the period minimum is a result of the donor’s response to mass transfer. The thermal timescale of the donor increases as its mass decreases ( $\tau_{KH} \propto M^{-2}$ ) until, similarly to what occurs at the upper edge of the period gap, it can no longer adjust its radius on a sufficiently short timescale. The donor therefore becomes ‘bloated’ as its radius is left too large for its mass. At roughly the same point in the evolution of the system, the mass of the donor drops to  $\lesssim 0.08 M_{\odot}$  at which point the core can no longer sustain hydrogen burning. This robs the star of its source of thermal energy, and the core begins to become electron degenerate. The radius of electron degenerate stars increases with decreasing mass, and hence the CV turns around in its period evolution—the radius and period now grow upon further mass loss. This sets an approximate minimum period below which the orbit ‘bounces’ back. Observations of CV populations place this minimum period at  $80 - 86$  min, owing to a significant spike in the number of

systems in this range [Gänsicke et al., 2009].

### 4.3.2 Classical Novae

Classical novae occur when accreted hydrogen builds up on the surface of the white dwarf, increasing the density and temperature of the innermost layers as more and more material accretes on top of it. Once this shell of material reaches a critical density, it ignites in a runaway hydrogen fusion reaction. The shell produces a vast amount of energy as it burns and rapidly expands, eventually being ejected from the system entirely [Chomiuk et al., 2021]. This may also affect the evolution of the system through frictional angular momentum loss [Schreiber et al., 2016]. Eruptions typically last a few to several hundred days and can increase the luminosity of a system by  $\Delta m = 8 \sim 15$  mag. When a classical nova has been observed to occur multiple times for a single system, the system is instead referred to as a recurrent nova.

## 4.4 Non-magnetic Cataclysmic Variables

Within the CV class, there are several subtypes with differing physical and observable properties. The presence of a strong magnetic field is particularly important when drawing distinctions between these subtypes, due to its effect on disc formation and the accretion geometry [Warner, 1995]. On account of this, the magnetic/non-magnetic subtypes will be discussed separately.

As noted above, CVs are named as such due to the violent (and in many cases frequent) interactions that take place within them. The observable manifestations of these interactions can be largely summarised as spikes in luminosity on varying timescales and of varying magnitude. One source of these spikes was seen in the eruptions of classical novae, for which the primary means of energy production is fusion. The second source, dwarf novae, are instead driven by gravity. Unlike classical novae, which can be observed equally in both magnetic and non-magnetic CVs, dwarf novae are largely restricted to non-magnetic systems.

### 4.4.1 Dwarf Novae

The dwarf novae class contains a number of subtypes and is the most abundant form of CVs. In the 1970s, two models were battling to explain frequent luminosity spikes (‘outbursts’) that were observed in known CVs [Yoji, 1996]. The first, Bath [1973], proposed that these outbursts are caused by an unstable rate of accretion

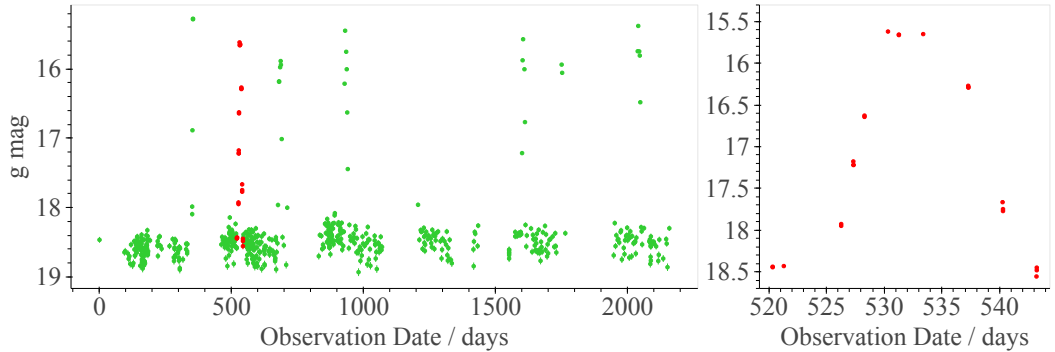


Figure 4.2: Left panel:  $g$ -band ZTF light curve of the dwarf nova J023517.98+411402.25, KW And. The light curve shows seven dwarf novae outbursts of  $\simeq 3$  mag, with one highlighted in red. Right panel: zoomed-in light curve of the highlighted outburst showing a rise and consequent decay to quiescence over  $\simeq 20$  d.

onto the white dwarf. In contrast, the second suggests that mass transfer rates from the secondary are in fact stable and that these spikes are instead caused by growing instabilities in the system’s accretion disc [Osaki, 1974]. After this instability reaches a maximum and causes the disc to outburst in a dwarf nova, the disc cools and the cycle repeats (see Fig. 4.2). Following the proposal of a solid mechanism for the thermal instability of the accretion disc in 1980 and further supporting discoveries shortly thereafter, the latter has since become the accepted mechanism of dwarf nova outbursts [Yoji, 1996]. The resulting spikes in brightness usually last  $\simeq$  days, and increase the magnitude of the system by  $\simeq \Delta m = 2 - 5$  [Warner, 1995] with a frequency of one per  $\simeq 10 - 200$  d [Osaki, 1974]. The following subtypes (SU UMa, ER UMa, WZ Sge, and Z Cam dwarf novae) are all forms of dwarf novae, with any remaining systems being classified as U Gem dwarf novae.

#### 4.4.1.1 SU UMa Dwarf Novae

The key property of SU UMa novae is the presence of occasional ‘superoutbursts’, which are greater in magnitude than standard outbursts by  $\simeq 1$  mag [Osaki and Kato, 2013b], and last weeks to months [Warner, 1995]. Superoutbursts typically occur before and after a phase of smaller outbursts: a ‘supercycle’, where the smaller outbursts are the disc instability novae described above [Osaki and Kato, 2013a]. These supercycles have a typical recurrence time of a few hundred days [Vogt, 1980]. Perhaps the most important characteristic of these superoutbursts is the presence of superhumps caused by tidal instability of the accretion disc, which are periodic oscillations in luminosity during the outburst decay [Warner, 1995]. These occur on

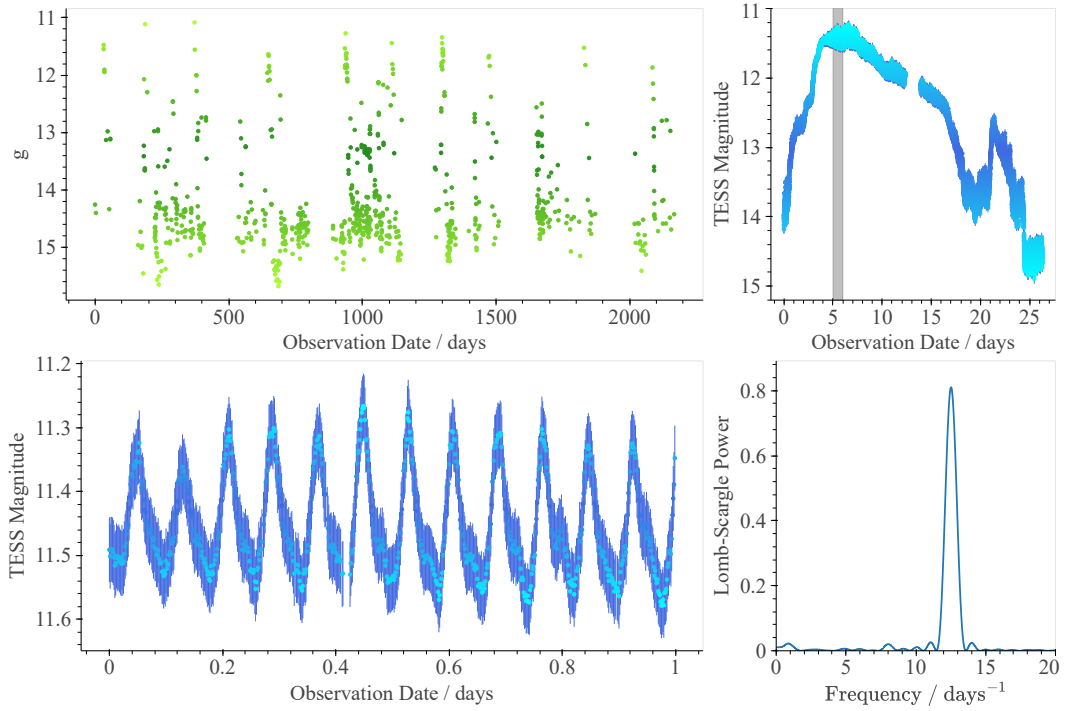


Figure 4.3: Light curves of J081228.27+623622.43, SU UMa—the prototype of its class. Top left panel:  $g$ -band ZTF light curve, showing frequent superoutbursts. Errors are too small to be seen. Top right panel: TESS light curve of one of its superoutbursts. Bottom left panel: TESS light curve, zoomed in on superhumps in the region indicated by the grey region in the top right panel. Bottom right panel: Lomb-Scargle power spectrum of these superhumps, suggesting a superhump period of  $\simeq 1.92$  h—4.9% longer than the system’s orbital period.

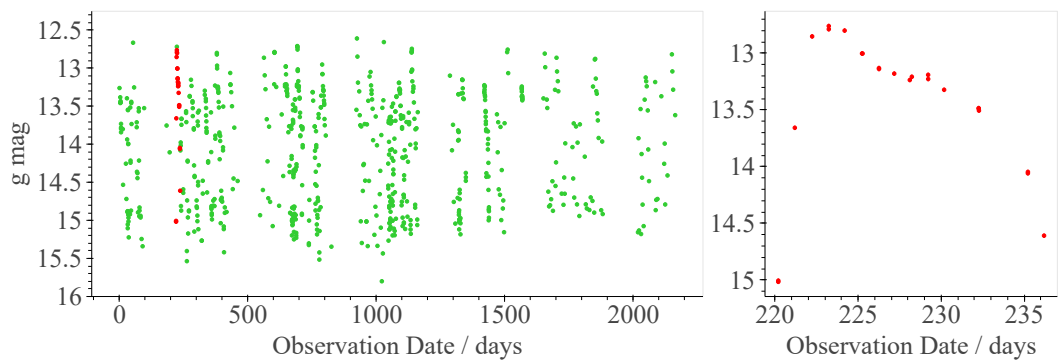


Figure 4.4: Left panel:  $g$ -band ZTF light curve of J094711.95+515408.9, ER UMa—the prototype of its class. Errors are too small to be seen. One of many visible superoutbursts is highlighted in red. Right panel: zoomed-in light curve of the rise and decay of the highlighted superoutburst.

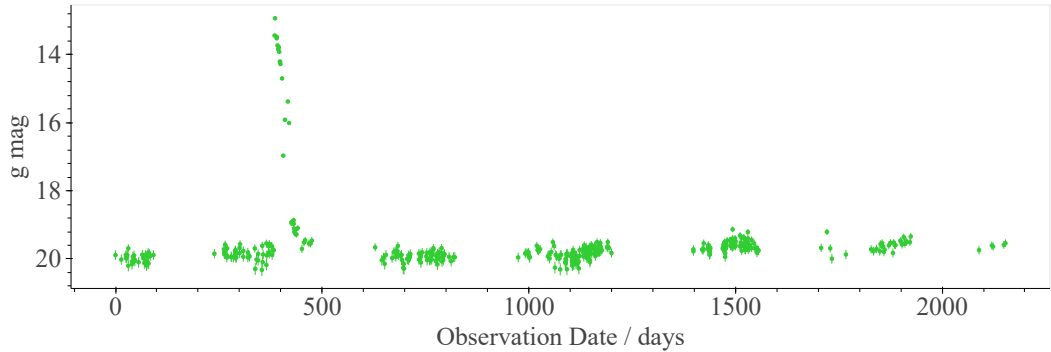


Figure 4.5: Left panel:  $g$ -band ZTF light curve of the WZ Sge dwarf nova J123225.80+142042.30, AL Com. The light curve shows one clear outburst of  $\simeq 7$  mag in the total coverage of  $\simeq 5.5$  years.

a period only fractionally ( $2 - 3\%$  [Osaki and Kato, 2013b]) higher than the orbital period (see Fig. 4.3).

The mechanism behind superoutbursts and supercycles in SU UMa stars is not fully understood, but there have been three proposed models. These are the thermal-tidal instability model, the enhanced mass-transfer model, and the thermal instability model [Osaki and Kato, 2013a]. No consensus on the most physically plausible mechanism has yet been reached. For further description of these models, see Osaki and Kato [2013a].

#### 4.4.1.2 ER UMa Dwarf Novae

ER UMa dwarf novae are a sub-set of SU UMa systems, with the defining characteristic of significantly more frequent superoutbursts and far shorter supercycles. The same supercycles that take place in SU UMa systems occur an order of magnitude more frequently, with a typical recurrence time of only  $19 - 44$  d. The standard (disc instability) outbursts within these supercycles also occur with a much shorter recurrence time of only  $3 - 4$  d [Kato et al., 1996] (see Fig. 4.4). This is thought to be caused by mass transfer rates up to an order of magnitude higher than what is observed in SU UMa systems, leading to greater thermal and tidal disc instabilities [Kato et al., 1996].

#### 4.4.1.3 WZ Sge Dwarf Novae

On the opposite end of the spectrum in terms of superoutburst frequency are WZ Sge systems, with a typical recurrence time of  $\simeq 10$  yr between superoutbursts. While infrequent, these superoutbursts are extremely bright—increasing the luminosity of

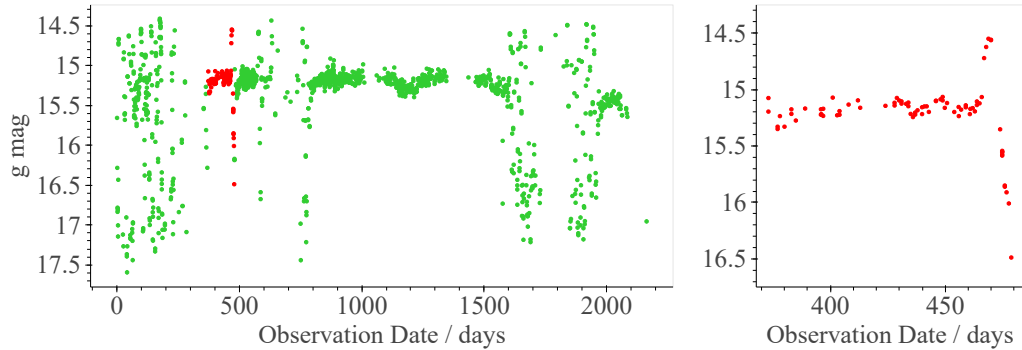


Figure 4.6: Left panel:  $g$ -band ZTF light curve of the ZCam dwarf nova J203104.53+472200.32, V507 Cyg. Errors are too small to be seen. The light curve shows three distinct periods of standstill and the start of a fourth at  $\simeq 2000$  d, with the third and longest such period lasting  $\simeq 800$  d. Right panel: zoomed-in light curve showing the first period of standstill, which is followed by an outburst and a consequent decay to quiescence.

the system by  $\Delta m \approx 8$  [Kato et al., 2002]. They are also often followed by smaller ‘echo’ outbursts which brighten the system by multiple magnitudes and occur  $\simeq$  days to months after the initial superoutburst [Patterson et al., 1998]. It has been proposed that these are caused by irradiation of the secondary following the increase in flux from the initial outburst [Buat-Ménard and Hameury, 2002]. An important point in support of this model is that it successfully predicts the observed decay pattern in these systems, which is essentially unchanged by the presence of echoes: the echoes simply appear to be superimposed on top of the outburst decay. This suggests that echoes are not caused by the same mechanism that drives the initial outburst, as the decay continues as it would if they were absent [Augusteijn et al., 1993]. In contrast to ER UMa systems, the infrequency of superoutbursts in WZ Sge systems is thought to be a result of a low mass transfer rate from a low-mass companion. A light curve of a known WZ Sge system is shown in Fig. 4.5.

#### 4.4.1.4 ZCam dwarf Novae

When the rate of mass transfer in a CV is high enough, the disc can become thermally stable [Kato, 2018]. In ZCam systems the mass transfer rate is thought to be near this critical level, resulting in temporary periods of thermal stability in the disc. This temporary stability manifests as ‘standstills’ in brightness between the quiescent and peak outburst luminosities [Warner, 1995] (see Fig. 4.6).

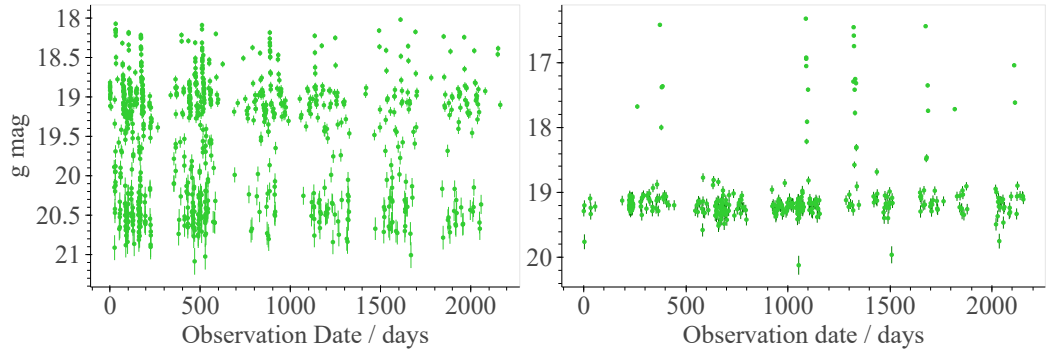


Figure 4.7: Left panel:  $g$ -band ZTF light curve of the AM CVn system J191905.18+481506.05, showing extremely frequent outbursts of  $\simeq 3$  mag. Right panel:  $g$ -band ZTF light curve of the AM CVn system J092638.73+362402.46, YZ LMi, showing infrequent outbursts of  $\simeq 2.5$  mag and eclipses of  $\simeq 1$  mag.

#### 4.4.1.5 U Gem dwarf Novae

The U Gem subtype encapsulates all systems that do not fall into the previously discussed (SU UMa, ER UMa, WZ Sge, and Z Cam) dwarf novae subtypes.

#### 4.4.2 Novalike Variables

As noted in the description of Z Cam systems, an accretion disc can become thermally stable given a high enough rate of mass transfer. This is also the case in novalike variables, where extreme mass transfer rates result in the disc being in a constant state of thermal stability [Kato, 2018]. Consequently, a key property of non-magnetic novalike variables is that no outbursts occur—they are non-eruptive [Fabian, 2009]. There are several subtypes within the non-magnetic novalike variable category, owing to particularities in observed luminosity variation [Warner, 1995].

#### 4.4.3 AM CVn

The key characteristic of AM CVn systems is accretion onto a white dwarf from a hydrogen-deficient donor, usually a lower mass white dwarf or an evolved and therefore helium-rich star [Ramsay et al., 2018]. In any case, the evolution of the donor requires the system to undergo significant orbital shrinkage in order for mass transfer to be initiated through Roche lobe overflow. As a result, AM CVn systems have very short orbital periods of  $\lesssim 65$  mins [Solheim, 2010]. While three different channels have been proposed for the formation of these systems, a consensus on the most physically plausible pathway has not yet been reached [Ramsay et al., 2018].

Depending on the orbital period (and hence orbital separation) of a given

AM CVn system, different structural properties arise. Due to similarities with the previously discussed CV subtypes, this can make the classification of AM CVn systems difficult. For systems with the shortest orbital periods ( $\lesssim 12$  min), no significant accretion disc can form. Systems with an intermediate orbital period of 12 – 20 min can support a large accretion disc and hence show fairly constant emission from the hot, stable disc, much like some novalike variables. For orbital periods of 20 – 40 min, the system supports the formation of a thermally unstable disc which may give rise to both outbursts and superoutbursts. The light curves of these systems are therefore very similar to those of SU UMa systems. The final group, with orbital periods of  $\gtrsim 40$  min, only support the formation of a cool, stable disc. The light curves of these systems are therefore similar to those of any dwarf nova in quiescence. Despite the apparent similarity of AM CVn systems to many non-magnetic CV subtypes, no analogue to strongly magnetic CVs (see below) has yet been found. This may be a result of the lack of a representative population, however, with only  $\simeq 60$  AM CVn systems being known [Inight et al., 2023]. See Solheim [2010] for a full review.

## 4.5 Magnetic Cataclysmic Variables

As noted at the start of this section, the presence of a strong magnetic field around the white dwarf is of particular importance to categorising CVs due to its effect on mass transfer and the accretion geometry. A strong magnetic field causes the inflowing ionised stellar material to be coupled to field lines, where it travels towards the white dwarf and is directly accreted onto its surface near one or both of its magnetic poles [Oliveira et al., 2017]. The formation of an accretion disc is therefore either disrupted or stopped entirely, with the former resulting in the truncation of the disc close to the white dwarf. A ‘strong’ magnetic field is typically considered to be  $B \gtrsim 1$  MG. While no consensus on the origin of these magnetic fields has yet been reached, a promising mechanism has recently been suggested by Schreiber et al. [2021]. This will be further discussed later.

### 4.5.1 Polars

The first polars were found as a result of polarisation measurements which suggested the presence of an unusually strong magnetic field [Smith, 2006]. Also known as AM Her type systems after their prototype star AM Herculis, polars are magnetic CVs with a typical magnetic field strength of more than 10 MG [Warner, 1995]. The strength of the field results in the Alfvén radius extending beyond the circulari-

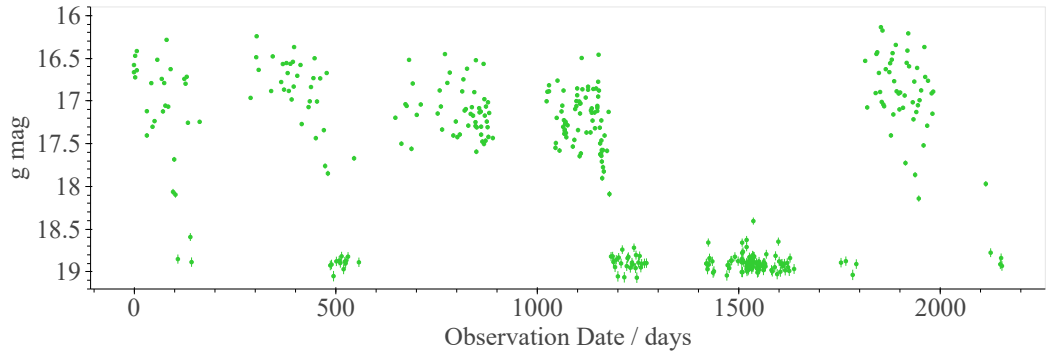


Figure 4.8: Left panel:  $g$ -band ZTF light curve of the polar J161007.50+035232.77, V519 Ser, showing transitions between two distinct brightness states. The presence of a strong magnetic field stops the formation of an accretion disc, resulting in a complete lack of outbursts.

sation radius, stopping the formation of an accretion disc as the trajectory of the infalling material is dominated by its motion along magnetic field lines [Cropper, 1990]. Accretion therefore follows the mechanism outlined above, with material being transported onto the magnetic poles of the white dwarf. As the infalling material is decelerated near the white dwarf surface, shocks develop which result in the emission of hard X-rays. Most of these are reprocessed by the white dwarf surface, and so are detected at much lower energies [Cropper, 1990]. The spiralling of charged particles along magnetic field lines releases optical cyclotron radiation which is strongly polarised, and it is this property that was responsible for the initial magnetic white dwarf detections mentioned above [Warner, 1995]. Another key observable property of polars is the presence of distinct high and low states in their luminosity variation, which is thought to be a result of changes in the rate of mass transfer [Wu and Kiss, 2008]. An example is shown in Fig. 4.8. These systems can also be identified through their orbital and white dwarf spin periods, due to interactions between the strong magnetic field of the white dwarf and the weaker magnetic field of the donor which cause the two to become synchronised [Smith, 2006]. Violent events such as novae outbursts and classical novae eruptions are thought to knock some polars slightly out of synchronisation, in which case the system is known as an asynchronous polar [Barlow et al., 2006].

#### 4.5.2 Intermediate Polars

In terms of the strength of their magnetic field, intermediate polars (also referred to as as DQ Her stars after their prototype star, DQ Herculis) sit between polars and non-magnetic CVs [Smith, 2006]. The reduced strength of the magnetic field results

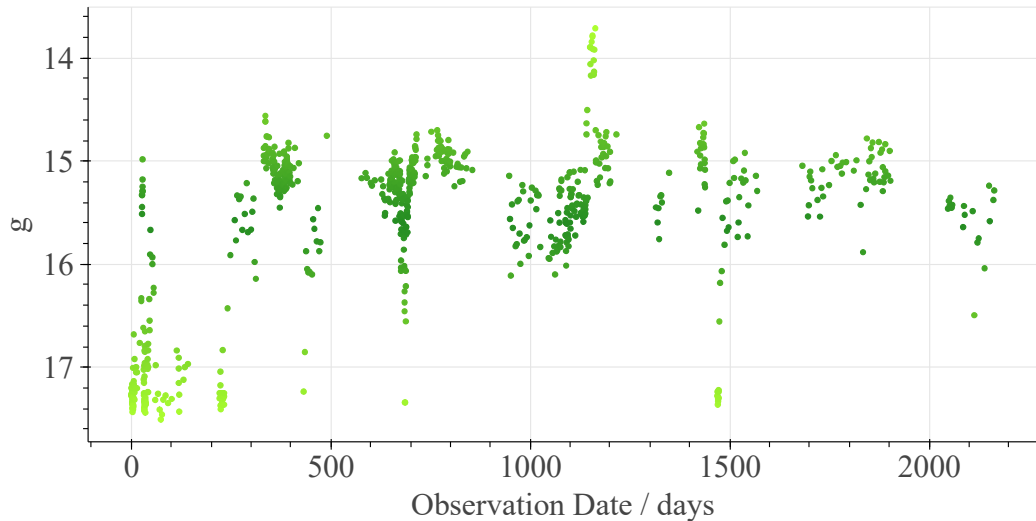


Figure 4.9: Left panel:  $g$ -band ZTF light curve of the intermediate polar J114338.49+714120.56, DO Dra, showing its distinct brightness states. The magnetic field is not strong enough to completely stop the formation of an accretion disc, leading to disc instability outbursts.

in the Alfvén radius extending beyond the white dwarf radius, but not reaching the circularisation radius. Infalling material then forms an accretion disc which extends inwards to the Alfvén radius, beyond which the motion of the material is dominated by the effect of the magnetic field. The disc is therefore truncated in these inner regions, with material being transported to the magnetic poles [Giovannelli, 2008]. As with their more magnetic counterpart, intermediate polars are therefore significant sources of X-ray emission [Warner, 1995]. The successful formation of the outer region of the disc means that, unlike polars, intermediate polars can support disc instability novae through the mechanisms discussed for non-magnetic CVs [Warner, 1995]. An example is shown in Fig. 4.9. Another important result of the weakened magnetic field is that the white dwarf spin is no longer synchronised to the orbital period, and so  $P_{\text{spin}} \ll P_{\text{orb}}$  [Giovannelli, 2008]. In many cases, the difference between these is up to an order of magnitude [Smith, 2006].

### 4.5.3 Pre-Polars

Also known as low-accretion rate polars, pre-polars are detached systems in which mass transfer only occurs via capture of the donor’s wind. As a result, the accretion rate is more than two orders of magnitude lower than in polars [Kafka et al., 2010]. The motion of captured material is once again dominated by the effect of the white dwarf’s strong magnetic field. There has been significant debate as to whether

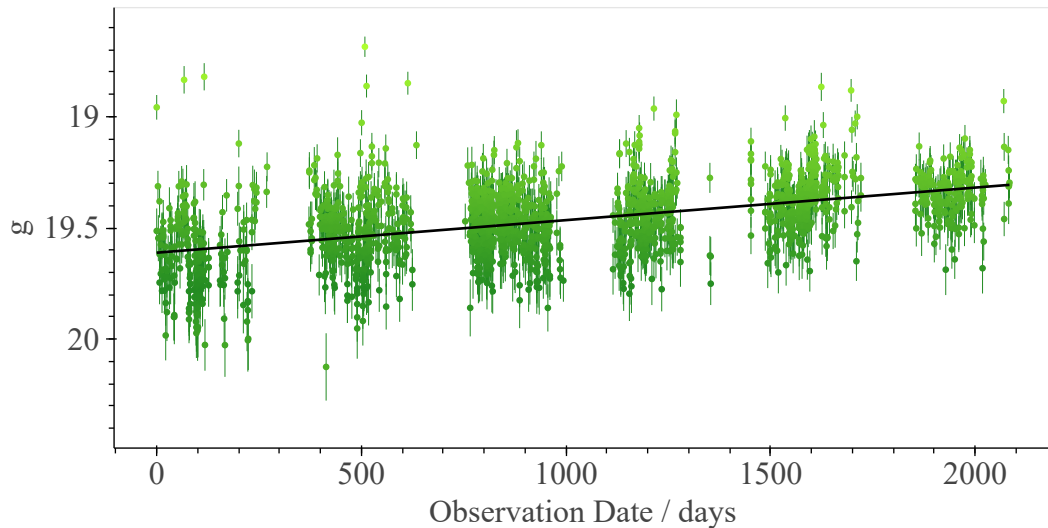


Figure 4.10:  $g$ -band ZTF light curve of the pre-polar J004924.50+222618.07, which has a low accretion rate due to mass transfer being driven by the capture of the donor’s stellar wind. Notably, the system is brightening at a rate of  $0.053 \text{ mag yr}^{-1}$ . A linear fit of the same rate is overlaid.

these systems are progenitors to polars, but it is now thought that the name holds. The current picture of pre-polars is that they were non-magnetic in the past, and acquired a strong magnetic field through a process that depends on a prior period of mass transfer—during which the orbital separation of the system grows until it is detached. Orbital shrinkage eventually re-initiates mass transfer via Roche lobe overflow of the donor, at which point the system is a polar [Wilson et al., 2021]. These systems exhibit cyclotron emission due to the presence of a strong magnetic field, but their luminosity in X-rays is very low [Inight et al., 2023]. Figure 4.10 shows an optical light curve for a known pre-polar system.

## 4.6 White Dwarf Pulsars

Until recently, the subtypes discussed above painted a fairly complete picture of the known CV zoo. 2016, however, brought to attention an elusive new subtype: white dwarf pulsars. The first white dwarf pulsar, AR Sco, was originally classified as a Delta Scuti variable [Marsh et al., 2016].

Delta Scuti stars are pulsating stars with a particularly fast pulsation period of  $\simeq 18 \text{ min} - 8 \text{ hr}$  [Handler et al., 2009]. The mechanism behind these pulsations is thought to be the  $\kappa$ -mechanism (‘kappa’ mechanism), where opacity effects within ionised zones of stars drive variability (see Dederick and Jackiewicz [2017] for a

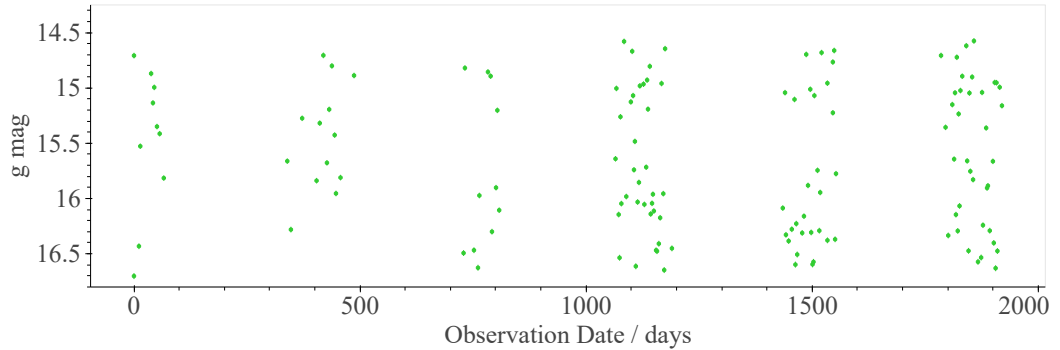


Figure 4.11:  $g$ -band ZTF light curve of the white dwarf pulsar J162147.28–225310.39, AR Sco, showing frequent pulsations in brightness of  $\simeq 2$  mag.

more in-depth discussion). However, Delta Scuti stars are not expected to be X-ray sources and yet AR Sco was detected by ROSAT—an all-sky X-ray survey. High-speed photometry then revealed large pulses in optical brightness on a timescale of only 1.97 min, quadrupling the optical flux in only 30 s [Marsh et al., 2016]. These pulses are detected across a very broad range of wavelengths, from the ultraviolet to radio. Despite white dwarf pulsars being a source of X-ray emission, the pulses have not been observed in X-rays [Marsh et al., 2016]. An optical light curve which shows the rapid modulation of brightness in AR Sco is shown in Fig. 4.11.

AR Sco has an orbital period of 3.56 h (see Fig. 4.12), placing it slightly above the period gap. The pulse frequency quoted above is a reprocessed frequency resulting from the interaction of the 1.95 min spin period of the white dwarf with the system’s 3.56 h orbital period, which suggests that the pulses are caused by an interaction between the white dwarf and its companion [Pelisoli et al., 2023]. White dwarf pulsars are therefore expected to necessarily exist as binary systems [Pelisoli et al., 2023]. The observed luminosity of the system exceeds that which would be expected from the combined luminosities of its components by a significant margin, suggesting the presence of an additional means of energy production. There are two possible mechanisms which could explain the observed luminosity of the system: accretion and spin-down luminosity [Marsh et al., 2016], where the latter refers to the energy released by the spinning down of a (usually compact) star. Marsh et al. concluded that this is only sufficient to produce the observed luminosity if the compact object is a white dwarf, while the former could power the system if the accretor was a neutron star.

Ultimately, the closeness to Earth of the system relative to known accreting neutron stars, the relatively low contribution of X-rays to the total luminosity of

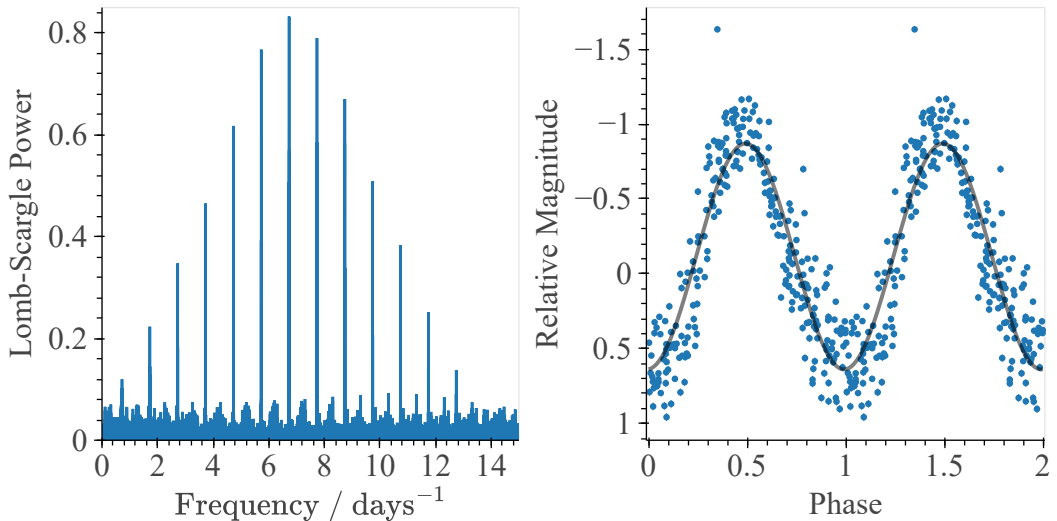


Figure 4.12: Left panel: Lomb-Scargle power spectrum of AR Sco’s ZTF photometry (all bands scaled and merged), suggesting an orbital period of 3.56 h. Right panel: Phase-folded ZTF light curve (all bands scaled and merged), folded on a period of 3.56 h. A sine wave of the same period is overlaid. Given magnitude values are relative to the median.

the system, the significantly longer spin period relative to any known millisecond pulsar (see the following section on pulsing X-ray binaries), and the mass constraints obtained for the system’s components all support the conclusion that the compact object is a white dwarf. More specifically, AR Sco is now known to be a white dwarf–M-dwarf binary. M-dwarfs are the most common form of star in our Galaxy, accounting for  $\simeq 70\%$  of observed stellar populations, and have typical masses of  $0.075 - 0.6 M_{\odot}$  [Bochanski et al., 2010; Rajpurohit et al., 2018].

The discovery of two further white dwarf pulsars followed that of AR Sco (Pelisoli et al. [2023], Segura Castro et al., in prep), establishing them as a new white dwarf binary subtype. The locations of the three known white dwarf pulsars in the Gaia Hertzsprung-Russell diagram are shown in Fig. 4.13, with a subset of known Delta Scuti stars overlaid.

As stated by Pelisoli et al. in their paper announcing the discovery of the second white dwarf pulsar, J191213.72–441045.08, “one of the main challenges to explain AR Sco is to reconcile the present fast spin-down rate with the rapid spin of the white dwarf”. AR Sco’s spin-down timescale of  $10^7$  yr [Marsh et al., 2016] suggests a magnetic field strength of 50–100 MG [Pelisoli et al., 2023], which results in the same spin-orbit synchronisation effect that is seen in magnetic CVs. In combination with the fact that the typical spin period of a newly formed white dwarf

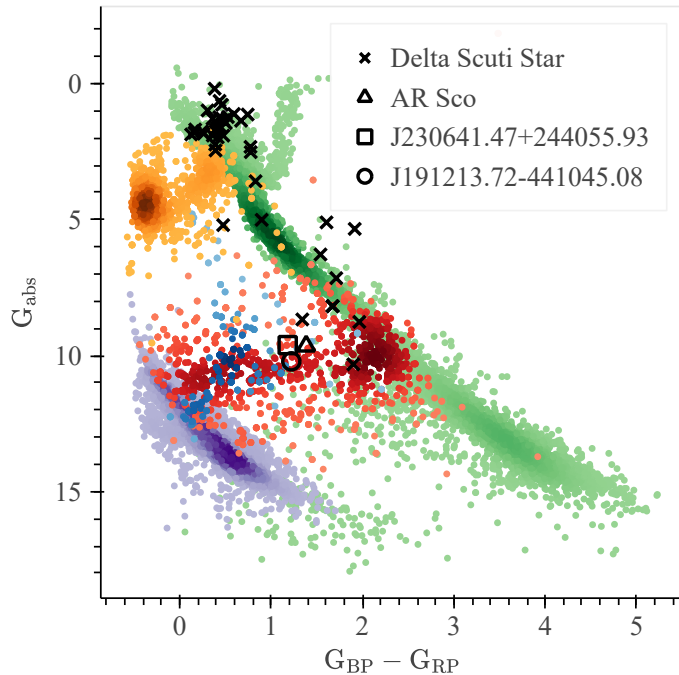


Figure 4.13: Gaia Hertzsprung-Russell diagram showing the locations of the three known white dwarf pulsars against known Delta Scuti stars. The background (coloured) is a 100 pc Gaia sample split into various sub-groups. Green: clean sample of stars, yellow: clean sample of spectroscopically confirmed subdwarfs, blue: clean sample of spectroscopically confirmed CVs, red: clean sample of spectroscopically confirmed white dwarf + M-dwarf binaries, purple: clean sample of white dwarfs. Background samples provided by B. Gänsicke.

is on the order of days [Pelisoli et al., 2023], AR Sco would therefore be expected to have a much slower spin than what is observed. Furthermore and unlike other CVs, AR Sco shows no signs of ongoing accretion by which it may have reached its current spin. However, a solution to this problem has been proposed which may also provide an answer to a long-standing question regarding observed magnetic CV populations.

It was noted in the discussion of magnetic CVs that no concrete mechanism for the generation of a strong magnetic field in white dwarfs has been found. As a result, the lack of strongly magnetic white dwarfs in detached systems with a young (non-compact) companion remains an unsolved mystery [Schreiber et al., 2021]. Many early suggestions involve the generation of the magnetic field during the formation of the system, e.g. via a magnetic dynamo which would operate during the CE phase. However, this fails to explain the aforementioned gap in observed magnetic CV populations. A mechanism proposed more recently by Schreiber et al.

[2021], which was also mentioned in the prior discussion of pre-polars, aims to solve this. In this scenario, the magnetic field is formed later in the white dwarf’s life cycle through the crystallisation of its core as it cools. The details of this mechanism will not be discussed here, but the result is similar to the dynamo mechanism that drives magnetic fields in main sequence stars and planets (see Isern et al. [2017] for a full review). The important feature of this mechanism is that the white dwarf initially lacks a strong magnetic field, as its generation now depends on the white dwarf’s age. This solves the long-standing mystery surrounding magnetic fields in young magnetic white dwarfs and simultaneously explains the present spin rates of white dwarf pulsars. In this picture, white dwarf pulsars ‘spin up’ to their observed spin rates via a phase of mass transfer prior to the generation of a significant magnetic field. The synchronising torque exerted by the magnetic field causes the rate of transfer of angular momentum from the spin of the white dwarf to the system’s orbit to increase as the field grows, gradually increasing the orbital separation [Pelisoli et al., 2023]. Mass transfer slows and eventually ceases, leaving the system in the detached state in which AR Sco is found. The loss of angular momentum to magnetic braking and gravitational wave radiation then shrinks the orbital separation until mass transfer is reinitiated, at which point the system will be detected as one of the previously known magnetic CV subtypes: a pre-polar, intermediate polar or polar. Unlike AR Sco, the second white dwarf pulsar, J191213.72–441045.08, does show signs of accretion. This system is therefore thought to be in an earlier stage of evolution, where the magnetic field is not yet strong enough to have caused the system to fully detach [Pelisoli et al., 2023]. This picture of white dwarf pulsars places them as an intermediary stage in the formation of polars, being the progenitors to pre-polars [Schreiber et al., 2021, Fig. 1].

## Chapter 5

# X-ray Binaries

Like CVs, X-ray binaries are binary systems in which a compact object accretes from a companion— usually a main sequence star. In these systems, however, the compact object is even more dense: a neutron star or black hole. X-ray binaries are the brightest X-ray sources in the sky beside the Sun, with the latter only being mentioned as a result of its proximity [Lewin et al., 1997].

### 5.1 The X-ray Binary Zoo

#### 5.1.1 Low-Mass and High-Mass X-ray Binaries

There are two fundamental classes of X-ray binary, which are separated by the mass of their donors. Low-mass X-ray binaries (henceforth LMXBs) contain a relatively low-mass donor ( $M_{\text{donor}} < 10 M_{\odot}$ , Lewin and van der Klis [2006]), and hence do not typically support a wind that is strong enough to drive the observed rate of accretion. Mass transfer is therefore instead driven by the Roche lobe overflow of the donor. The amount of energy released by infalling material is significantly higher than in white dwarf binaries (Eq. 3.6), resulting in even stronger X-ray emission. A small amount of this X-ray radiation is reprocessed as it travels through the disc or accretion stream, resulting in variable emission at optical wavelengths [Lewin and van der Klis, 2006; de Jong et al., 1996]. High-mass X-ray binaries (henceforth HMXBs) contain a more massive donor ( $M_{\text{donor}} > 10 M_{\odot}$ ), allowing observed X-ray luminosities to be achieved through only gravitational capture of the stellar wind. The optical emission from the significantly more massive donor in HMXBs surpasses their X-ray flux from accretion and hence dominates their total luminosity [Lewin and van der Klis, 2006]. While less common, it is important to note that some HMXB systems with particularly close orbits may exhibit mass transfer via Roche

lobe overflow of the donor [Fornasini et al., 2023].

This difference in configuration between the two classes has significant consequences for the properties and evolution of a given system, which can only exist as an X-ray binary for as long as it drives strong X-ray emission. The lifetime of a system in either class is therefore set by the timescale for which it can support mass transfer. In LMXBs, this is simply an inverse function of the mass transfer rate,  $\dot{M}$  [Lewin and van der Klis, 2006]. In HMXBs however, the evolution of the donor can disrupt the system before all of its material has been lost to the accretor. As a result, the lifespan of HMXBs is shorter by up to  $\simeq 2$  orders of magnitude [Lewin and van der Klis, 2006]. HMXBs are therefore primarily distributed among regions containing young stars, such as the Galactic plane.

The next step in exploring the X-ray binary zoo is to once again consider a fundamental property of interacting binaries: luminosity variation. As in CVs, the strength of the magnetic field is of particular importance here due to its effect on the accretion geometry. However, there is now an additional consideration to be made: the nature of the accretor. The presence of an event horizon around a black hole inherently complicates things, and as stated in Lewin and van der Klis [2006], “the main observational manifestation of these differences is the presence or absence of pulsations in the X-ray light curves of the systems, which reflects the strength of the magnetic fields of the central objects”. It is this, the presence or lack of X-ray pulsations, which will be used to further distinguish between the X-ray binary subtypes.

### 5.1.2 Pulsing X-ray Binaries

While the mechanisms that govern the formation and evolution of CVs are unlikely to be completely analogous to those in X-ray binaries, it is reasonable to expect that significant similarities will arise—especially in the case where the accretor is a neutron star. The primary differences that result from the more violent collapse through which a neutron star is formed are threefold: the accretor is far more dense, is spinning extremely rapidly, and hosts a far stronger magnetic field. The latter is thought to be due to the conservation of magnetic flux as the system collapses [Peng and Tong, 2007], resulting in magnetic field strengths of  $10^2 - 10^9$  MG [Reisenegger, 2003]. Besides the strength of the magnetic field, it is also important to consider its geometry. The exact geometry of the magnetic field around any accreting compact object is extremely complex due to the combination of the accretor’s magnetic field and contributions from material in the disc, but in both white dwarfs and neutron

stars the magnetic field largely originates from the compact object itself. This claim is not so easily made for a black hole, where the presence of an event horizon disrupts the structure of the external field generated by moving charged particles in its accretion disc (see, for example, Blandford and Znajek [1977]). Furthermore, the presence of the horizon in a black hole also necessarily leaves no ‘surface’ with which to interact. This clashes with accepted pulsation mechanisms, and hence any further discussion of pulsating X-ray binaries will only consider systems in which the accretor is a neutron star.

As expected, the effect of a strong magnetic field on the transfer of mass to an accreting neutron star is largely analogous to the case of an accreting white dwarf. Material in the disc that is travelling slowly enough to be captured by magnetic field lines will travel to the magnetic poles, where it is accreted onto the neutron star. The fate of material in the disc that is travelling too fast to be accreted onto the neutron star is not well known but is expected to be expelled via wind processes [Lewin and van der Klis, 2006]. Once again, the accretion disc around a neutron star is therefore truncated at its inner region or unable to form at all [Lewin et al., 1997]. Shocks develop in the high-velocity, columnated material near the accreting magnetic pole, resulting in significant X-ray emission. If the rotation axis of the neutron star is misaligned with its magnetic poles, this X-ray emission is cast across the Universe like a beam from a lighthouse as the viewing angle of the impact zone varies with time [Lewin and van der Klis, 2006]. This phenomenon is observed as a pulse in the X-ray luminosity as the beam sweeps over us at regular intervals, giving these systems their label as X-ray pulsars. Populations of known X-ray pulsars are dominated by systems in the HMXB class—i.e. those with high mass donors. The exact reason for this is not known, but many possible causes have been proposed. A full review of these can be found in Niang et al. [2024].

Naturally, an important property to consider for an X-ray pulsar is its spin. This parameter may experience both spin-up (spin acceleration) and spin-down (spin deceleration) states, with the prevalence of either being set by the interaction of the neutron star’s magnetic field with its disc. As in magnetic braking, the neutron star’s magnetic field lines sweep out a circle as they are dragged by the neutron star’s spin. Material in the disc is carried by these lines, coupling the disc to the surface of the neutron star [Lewin and van der Klis, 2006]. It is this coupling that decides whether the pulsar is spinning up or down. If the spin rate of the neutron star is greater than that of its disc, it loses angular momentum to the disc to synchronise its rotation: the pulsar spins down. In the opposite case, the disc loses angular momentum to the neutron star: the pulsar spins up. Inner regions of the disc necessarily orbit more

slowly than its outer regions, and so in a given system both of these effects will be occurring at the same time. The balance of these therefore produces the net result of a spin-up/spin-down state [Lewin and van der Klis, 2006]. It then follows that there must be an equilibrium where these opposite torques balance and the pulsar’s spin essentially becomes static. As long as accretion is maintained, it is this state that accreting pulsars tend towards as they age [Lewin and van der Klis, 2006]. There are two classes of X-ray pulsars that are separated by their spin periods. Millisecond pulsars, as the name would suggest, are pulsars with spin periods on the order of milliseconds. These are generally found in close binaries, where the orbital period is very short. The second subtype, referred to only as ‘X-ray pulsars’, has slightly longer spin periods (on the order of a second) and is mostly found in HMXB systems [Lewin and van der Klis, 2006].

In the absence of accretion, e.g. in single systems, pulsars instead emit lower energy pulses at radio wavelengths. The pulsation mechanism is analogous to that described for X-ray emission above, resulting from misalignment of the magnetic and rotational axis, but a consensus on the exact cause of radio emission from these systems has not yet been reached [Philippov et al., 2020]. Radio pulsars gradually lose rotational energy to gravitational wave radiation and magnetic dipole radiation, with no counteracting spin-up via interaction with a companion. These systems therefore spin down as they age [Gunn and Ostriker, 1969]. An additional mechanism which is expected to contribute to the observed spin-down of these systems has also more recently been proposed, where a gradual change in the state of the neutron star’s core acts to slow its rotation [Ho and Andersson, 2012]. Despite the combined contributions of these three effects, the spin-down rate of radio pulsars remains extremely low. In fact, the pulse interval in these systems remains sufficiently consistent for use in ‘astronomical clocks’, with the first ‘pulsar clock’ being created using signals from six radio pulsars in Gdańsk, Poland in 2011 [Vidal, 2019]. Similarly to X-ray pulsars, radio pulsars have been observed to exhibit typical spin periods from milliseconds to seconds [Caleb et al., 2022].

While the distinction between pulsations occurring at X-ray and radio energies is not always a simple one, the general picture described here is typically fairly representative. It is also important to note that, regardless of the energies at which they operate, the aforementioned pulsations can only be observed if they happen to cross our line of sight. This is not always the case and is particularly unlikely in systems with an insignificant misalignment of the magnetic and rotational axes, or those in which the impact zones are obscured by the accretion stream or disc [Lewin and van der Klis, 2006].

### 5.1.3 Non-Pulsing X-ray Binaries

Even in systems in which there is ongoing accretion, the majority of X-ray binaries will not exhibit the pulsations discussed above. A significant contribution to this arises from the absence of pulsations in accreting black holes, due to the lack of a surface from which these pulses could originate [Lewin and van der Klis, 2006]. As stated in Lewin and van der Klis [2006], the overarching problem is that the event horizon “does not allow any stable feature to be anchored to the rotation of the compact object”. The pulsation mechanism in such a system would therefore have to differ greatly, and hence no ‘black hole pulsar’ has been found to date [Levin et al., 2018]. When the accretor is a neutron star, however, X-ray pulsations will inevitably arise as long as there is accretion onto the magnetic poles. For this reason, any non-pulsing X-ray binary in which the accretor is a neutron star must necessarily have a weak magnetic field ( $\lesssim 10^8$  G, Lewin and van der Klis [2006]).

#### 5.1.3.1 Transient and Persistent Sources

There are two further subtypes to consider within the non-pulsing X-ray binary class: transient and persistent sources. The former exhibit extremely rare but large X-ray outbursts, similarly to WZ Sge CVs. These outbursts increase the system’s X-ray flux by several magnitudes and do not recur for anywhere from months to decades [Lewin and van der Klis, 2006]. The latter, as their name would suggest, consistently emit in X-rays. The X-ray flux of these systems can still be highly variable, however, generally varying within factors of a few on a period of milliseconds to months. Even ignoring the violent outbursting observed in transient sources, this makes X-ray binaries some of the most variable systems in the sky. This consistent variability is thought to arise from non-uniformity in the timescales that govern the system’s emission, which can vary by several orders of magnitude [Lewin and van der Klis, 2006].

One of the primary parameters establishing into which subtype a system falls is the compactness of its accretor, with neutron stars dominating persistent sources and black holes dominating transient sources [Lewin and van der Klis, 2006]. The outbursting mechanism in transient systems is thought to be the same as in dwarf novae CVs, in which a growing thermal-viscous instability causes the disc to outburst. The disc then cools, resulting in intermittent phases of quiescence between outbursts [Lewin and van der Klis, 2006]. Similarly to WZ Sge systems, these outbursts are sometimes followed by a number of smaller outbursts which are thought to arise from irradiation of the companion [Augusteijn et al., 1993]. The

frequency of outbursts depends heavily on the temperature of the disc and hence the degree of illumination from the compact object, which unsurprisingly is expected to be significantly lower for black holes. This is once again a result of the event horizon, which traps much of the accretion luminosity and prevents the storage of latent heat. Transient systems in which the accretor is a black hole are therefore fainter than those containing a neutron star by  $\simeq 1$  magnitude in quiescence and exhibit longer but significantly less frequent outbursts [Lewin and van der Klis, 2006].

#### 5.1.4 X-ray Binary Formation Channels

The formation channels leading from a main sequence–main sequence binary to a white dwarf–main sequence binary and beyond were shown in Fig. 4.1. However, the pathway followed by a system whose primary star is massive enough to collapse beyond a white dwarf has not yet been discussed. Figure 5.1 shows the possible formation channels for various X-ray binary systems, starting with a system in which the more massive primary is in the process of collapse (a). This is the same close compact object–main sequence configuration from which most evolution stemmed in Fig. 4.1. It is important to note that in any of the following configurations, any neutron star that has not experienced a long period of spin-down may be observed as a pulsar—typically pulsing in X-rays in the presence of accretion, or radio waves in its absence.

The formation of a neutron star or black hole is significantly more violent than that of a white dwarf, giving rise to a core-collapse supernova. Consequently, it is important to first consider whether the binary survives the collapse of the primary. If the force of the explosion is sufficient to overpower the binary coupling, the result is a high-velocity compact object and a runaway main sequence star (a  $\rightarrow$  c). This outcome is highly likely, as reflected by the dominance of single pulsars in observed pulsar populations [Lorimer, 2008]. If the compact component formed by the collapse is a neutron star, it will gradually spin down due to the lack of ongoing accretion. Once the spin is no longer sufficient to drive significant radio emission, the system can no longer be observed as a pulsar—the pulsing mechanism ‘turns off’. The spin evolution of black holes is a much more complicated problem, but it is expected that their spin rates remain largely unchanged in the absence of accretion. A full review can be found in King and Kolb [1999]. For systems in which there is no potential for future mass transfer, this is the final evolutionary stage of the compact component. In the case where the binary coupling is strong enough to survive the collapse, the result is a widened (detached) binary in which the newly formed neutron star or black hole continues to exist as a binary system (a  $\rightarrow$  b). The

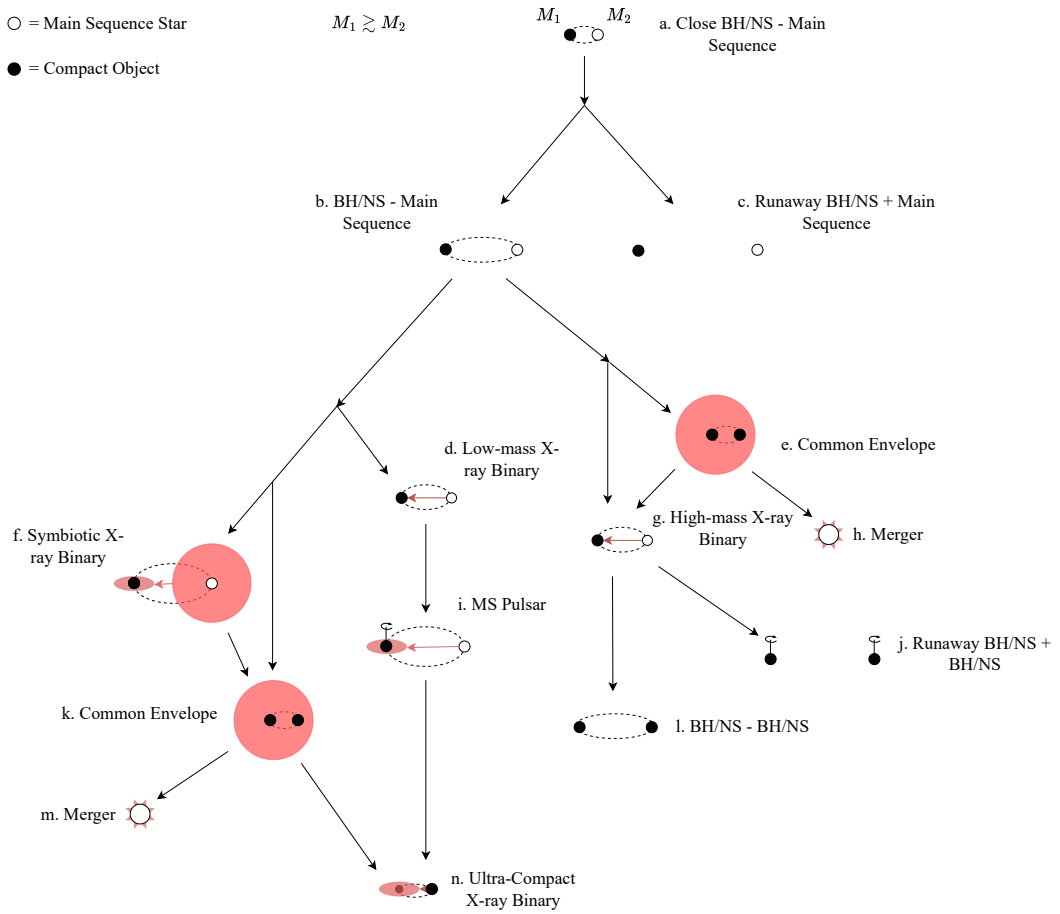


Figure 5.1: Possible evolutionary pathways followed by a main sequence-neutron star/black hole binary. In the initial state, the more massive primary component has just collapsed to form a neutron star, which the system may or may not survive. Arrows denote transitions between stages of evolution. Information adapted from Belloni and Schreiber [2023] and Lorimer [2008].

system may remain in a detached state for  $\simeq 10^7 - 10^8$  yr [Lorimer, 2008].

For those systems that do survive, the evolutionary pathway then depends on the mass of the donor. For configurations in which the secondary is of high enough mass to cause a second core-collapse supernova, the system follows the HMXB pathway. Mass transfer is then initiated via gravitational capture of the donor’s stellar wind or its evolution—in this case forming a supergiant [Belloni and Schreiber, 2023]. For dynamically unstable mass transfer, rapid orbital shrinkage leads to the initiation of a CE phase (b  $\rightarrow$  e). Depending on the ejection of the envelope, the two components either collide in a merger (e  $\rightarrow$  h) or emerge from the expelled envelope in a significantly tightened configuration—at which point the system is a HMXB

(e → g). For dynamically stable mass transfer, the system is observed as a HMXB in an initially wider configuration—with no phase of CEE occurring (b → g). Upon the collapse of the secondary, the survival of the system must once again be considered. If the system survives the resulting core-collapse supernova, the system becomes a neutron star/black hole–neutron star/black hole binary (g → l). Failing this, both components are once again propelled apart as they would have been if the system did not survive the collapse of the primary (g → j) [Lorimer, 2008].

If the donor is instead of lower mass, the available pathways are largely analogous to those in CVs—with the next stage of evolution being set by the nuclear timescale of the donor. If this is sufficiently shorter than the timescale for orbital angular momentum loss, a symbiotic X-ray binary is born as the donor evolves into a red giant without engulfing the accretor (b → f). For more information on these systems, see the previous section on symbiotic binaries and symbiotic X-ray binaries. For dynamically stable mass transfer, the timescale on which the system is observable in this configuration is set by the response of the orbital separation to mass transfer. For dynamically unstable mass transfer, a phase of CEE is once again initiated (f → k) with the now familiar outcomes of a merger (k → m) or significant tightening of the binary configuration. Fusion in the low-mass donor eventually ceases, and its core shrinks to form a white dwarf. Once the transfer of mass is reinitiated via orbital shrinkage (and hence Roche lobe overflow of the white dwarf), the system is observed as an ultra-compact X-ray binary (k → n) [Belloni and Schreiber, 2023]. Similarly to what was seen in Fig. 4.1, this phase of CEE could also have been reached if the orbital separation was small enough at the time of the donor’s evolution—bypassing the formation of a symbiotic X-ray binary (b → k).

If the transfer of mass is instead initiated by Roche lobe overflow on a timescale shorter than the donor’s nuclear timescale, an LMXB is born (b → d). Since the lifetime of a star is a strong inverse function of its mass (Eq. 2.2), the low mass of the donor allows for the accretor to be significantly spun up—often to periods of  $\sim 10^{-3}$  s. This is therefore the expected formation pathway for millisecond pulsars (d → i) [Lorimer, 2008]. If the pulsar had previously been ‘turned off’ due to deceleration of its spin, this long period of mass transfer may rejuvenate its pulsation mechanism—in which case the system is known as a ‘recycled’ pulsar. Once fusion eventually ceases in the donor, its core once again shrinks to form a white dwarf and the system is then observed as an ultra-compact X-ray binary (i → n).

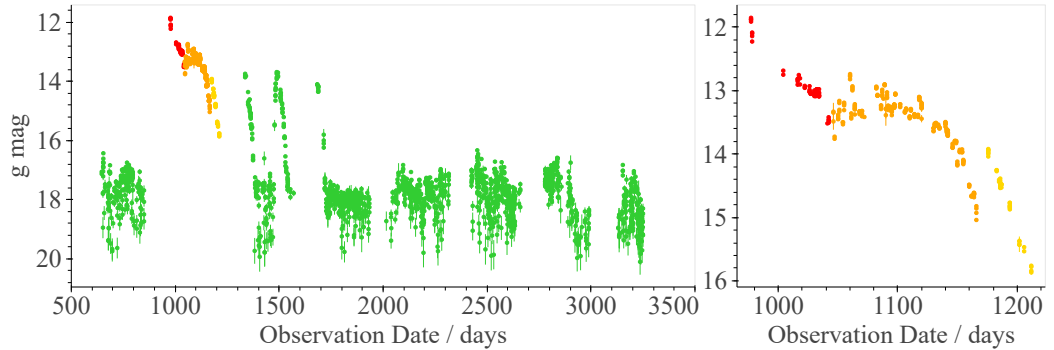


Figure 5.2:  $g$ -band ATLAS light curve of the low-mass black hole X-ray binary J182021.94+071107.28. Left panel: full light curve showing the transient outburst in 2018, followed by a long period of quiescence. Right panel: zoomed-in light curve of the initial outburst (red), showing two echo outbursts (orange and yellow, respectively) during its decay to quiescence.

## 5.2 Observations at Longer Wavelengths

Despite the majority of this discussion being centred around observations in X-rays, longer wavelength observations cannot be ignored. These provide access to fundamental properties of the underlying system, such as its orbital period, the masses and elemental abundances of its components, and the rate of mass transfer [Lewin and van der Klis, 2006]. As has already been noted, X-ray binaries emit a significant amount of optical flux. In LMXBs this is largely a result of the reprocessing of X-rays by the infalling material, while in HMXBs this originates primarily from the optical luminosity of the giant companion. In any case, the reprocessing of X-rays into optical flux results in the two typically being positively correlated with one another. An example of this is shown in Fig. 5.2, which shows the optical light curve of an X-ray binary in outburst.

## Chapter 6

# The Compact Binary Landscape

### 6.1 Gaps in our Current Understanding

Despite the great strides in our understanding of compact binaries in recent decades, the current picture remains incomplete. Some key examples of this can be found in CVs. One such example is the distinct lack of ‘period bouncers’, i.e. CVs that have bounced back from the period minimum and are hence evolving towards longer orbital periods [Schreiber et al., 2023]. Recent predictions suggest that over half (even as high as 75%) of CVs should be observed in this state [Goliasch and Nelson, 2015; Belloni et al., 2018], and yet the observed fraction is as low as a few percent [Inight et al., 2023]. In fact, Schreiber et al. [2023] states that “this discrepancy between theoretical prediction and observations might be the most important problem in our understanding of CV evolution”. Another problem is the average mass of white dwarfs in CVs, which is observed to be significantly higher than that of single white dwarfs ( $0.8 - 1.2 M_{\odot}$  compared to  $0.6 M_{\odot}$ , respectively [Warner, 1973; Koester et al., 1979]). Flipping this problem on its head, many of the known detached white dwarf–M-dwarf binaries (of which there are plenty) do not host a sufficiently massive white dwarf to be true progenitors of the CVs that are observed today [Wijnen et al., 2015]. Similar problems are also present in the mechanisms that drive CV evolution, with a key example being magnetic braking. As discussed previously, magnetic braking is a significant driver of angular momentum loss in compact binary systems, and this is particularly true in those with short periods. Despite this, it remains poorly understood. Due to the empirical nature of its description and difficulties in extrapolating early models (which were derived from single, Sun-like stars) to compact binary systems, the estimated magnitude of the magnetic braking torque can differ by several orders of magnitude across available

literature for a given system [El-Badry et al., 2022].

### 6.1.1 Observational Bias

Due to the potential for observational bias, the above (and any similar) problems are only made worse in classes for which there are a limited number of known systems. As an example: while the discrepancy between expected and observed white dwarf masses in CVs is now known to be a true (but not well-understood) bias of these systems, it was originally suggested to be a result of a selection effect. Ritter [1976] proposed that CVs hosting higher mass white dwarfs would be far brighter due to both the greater energy release per unit of accreted mass and the size of the resulting accretion disc, and would hence be more easily observed. Only with observations of significantly more faint CVs was this hypothesis proven to not be the case [Wijnen et al., 2015]. Another example of observational bias in the history of CV research is discussed in Gänsicke [2005], which explores the impact of X-ray instrumentation on known CV populations. The arrival of wide-coverage X-ray surveys in recent decades brought with them the discovery of the first X-ray-bright (and often magnetic) CVs, ushering in a significant expansion of the models of CV formation and evolution. Importantly, Gänsicke [2005] notes a significant bias in the populations of CVs returned by different observational approaches. In a sample of 525 known CVs, those identified through their variability were dominated by dwarf/classical novae, while those identified through their X-ray emission were primarily magnetic systems. Providing an answer to even the seemingly simple question of the relative abundances across the CV subtypes would therefore be impossible using either of these populations in isolation.

### 6.1.2 The Most Problematic Compact Binary Subtypes

While the challenges highlighted above were discussed in the context of CVs as a whole, the prevalence of such issues is heightened within individual subtypes due to the more limited number of known systems. Perhaps the most significant example of this is that of white dwarf pulsars, of which there are only three known systems due to the recency of their discovery (Marsh et al. [2016], Pelisoli et al. [2023], Castro Segura et al., in prep). These challenges are of course also experienced in the higher-mass counterparts of CVs, particularly in those that host a black hole accretor due to the complexity of their evolution. Similarly to white dwarf pulsars, the number of known systems in this class remains small, with only 19 dynamically confirmed black hole X-ray binaries at the time of writing [Corral-Santana, 2024].

It is important to note that this population is also strongly biased towards transient systems owing to the relative likelihood of identifying systems in outburst compared to those in quiescence.

### 6.1.3 The Way Forward

From the above discussion, it is clear why expanding upon the known populations of compact binaries is of great importance. A significant source of this expansion is likely to come from improvements in X-ray instrumentation. This is particularly true in the case of black hole X-ray binaries, as illustrated by Figure 1 in Corral-Santana et al. [2016]. This figure shows the history of advancements in X-ray instrumentation and the resulting increase in the number of known black hole binaries (both candidates and those that have been dynamically confirmed). A more up-to-date version can be found in Corral-Santana [2024]. As would be expected, the trend is clearly positive. However, this figure does not yet include a recent advancement: eROSITA. The Extended ROentgen Satellite with an Imaging Telescope Array (eROSITA), which launched in 2019, is the successor to the ROSAT satellite which began its operation nearly 30 years prior in 1990. ROSAT marked a great advancement in X-ray astronomy during its time, essentially setting a new standard with its unprecedented sensitivity and coverage of the X-ray sky [Trümper, 1993], and the same is expected to be achieved by eROSITA. While the focus of many recent advancements in X-ray astronomy has been on sensitivity, this has so far come at the cost of sky coverage. eROSITA aims to solve this problem, by obtaining the most complete map of X-ray sources in and beyond our Galaxy—with no compromise on the sensitivity of its detections [Predehl et al., 2021]. eROSITA released its first set of data in January of this year, although it is important to note that at the time of writing only half of the data (eROSITA-DE) has been released—covering regions in the range  $180 \leq l \leq 360$  deg where  $l$  is the Galactic longitude.

The goal of this work is therefore to expand upon the existing populations of two classes of compact binaries for which the number of known systems is most severely lacking. As noted above, these are white dwarf pulsars and black hole X-ray binaries. Due to the time constraints of an MSc, the search for the latter will be more explorative and will hence largely focus on highlighting the difficulties faced by searches of this kind through the use of the first data release of eROSITA-DE.

# Chapter 7

## Methods

### 7.1 Observational Techniques

It is clear from the discussion so far that the main properties of interest when identifying compact binary systems are: the system's brightness variation, the orbital period,  $P_{\text{orb}}$ , the rate of mass transfer,  $\dot{M}$ , the strength of the accretor's magnetic field,  $B$  and—particularly in X-ray binary systems—the nature of the compact accretor.

#### 7.1.1 Observing a System's Brightness through Time

The utility of outburst observations as a means of classification has already been shown in Figs. 4.2–4.10, and Fig. 5.2. The light curves included here, however, are fairly ideal cases; in reality, their interpretation is often significantly more complicated. An example of this can be found in the light curves of transient X-ray binaries and WZ Sge systems, whose outbursts have a typical recurrence frequency of only one per  $\simeq 10$  yr. Available light curves of these systems (as shown in Figs. 5.2 and 4.5) typically cover a period of  $\lesssim 10$  yr, and may contain significant gaps between periods of observation—with these gaps often being longer than the typical outburst duration. Consequently, a given WZ Sge/transient X-ray binary system may show no recorded outburst in any available light curves.

More generally, the recurrence times, durations and magnitude ranges of outbursts discussed for various cataclysmic variable subtypes are only typical values. For example, AM CVn light curves can often be very difficult to distinguish from those of other subtypes. Figure 4.7 shows light curves for two different AM CVn systems, with the left panel being visually similar to the ER UMa system in Fig. 4.4, and the right panel being visually similar to the dwarf nova system in Fig. 4.2; the

magnitude and frequency of outbursts, in either case, are essentially the same. The distinction between the light curves of various subtypes is therefore often blurred, and so their inspection is rarely a sufficient means of classification in isolation from other methods.

### 7.1.2 Estimating the Orbital Period

However, the time dependence of light curve photometry also provides insight into another fundamental property that separates the many subtypes of compact binary. An example of this distinction is evident in the orbital periods of polars and intermediate polars, with the former often being  $\lesssim 2$  h and the latter typically being  $\gtrsim 3$  h [Warner, 1995]. ‘Time series analysis’ is the practice of revealing periodicities (such as orbital periods and spin periods) in a system’s brightness variation via the analysis of its time-dependent photometry.

#### 7.1.2.1 Power Spectra and the Lomb-Scargle Periodogram

An example of a power spectrum was shown previously in Fig 4.12, where AR Sco’s orbital period was derived. The method used here was the Lomb-Scargle periodogram [Lomb, 1976; Scargle, 1982], which is particularly effective in the analysis of unevenly spaced data. The method fundamentally works by least-squares fitting a number of sine waves to a given data set, with each of these sine waves taking the form:

$$y(t, f) = A_f \sin(2\pi f(t - \phi_f)),$$

where  $y$  is some parameter (in this case the system’s brightness) as a function of time,  $t$  [VanderPlas, 2018]. The quality (‘power’) of a given sine wave is then given by the standard  $\chi^2$  statistic, i.e.

$$\chi^2(f) = \sum_n (y_n - y(t_n, f))^2.$$

The amplitude,  $A_f$ , and phase,  $\phi_f$  of this sine wave are optimised via the minimisation of  $\chi^2$ , and hence the maximum power at the current frequency is obtained. By carrying out this process across a number of discrete frequencies,  $N$  (typically  $N \simeq 10^5$ ), a power spectrum is obtained, with the frequencies of greatest power (as well as their closest integer harmonics) revealing the strongest periodic signals in the data.

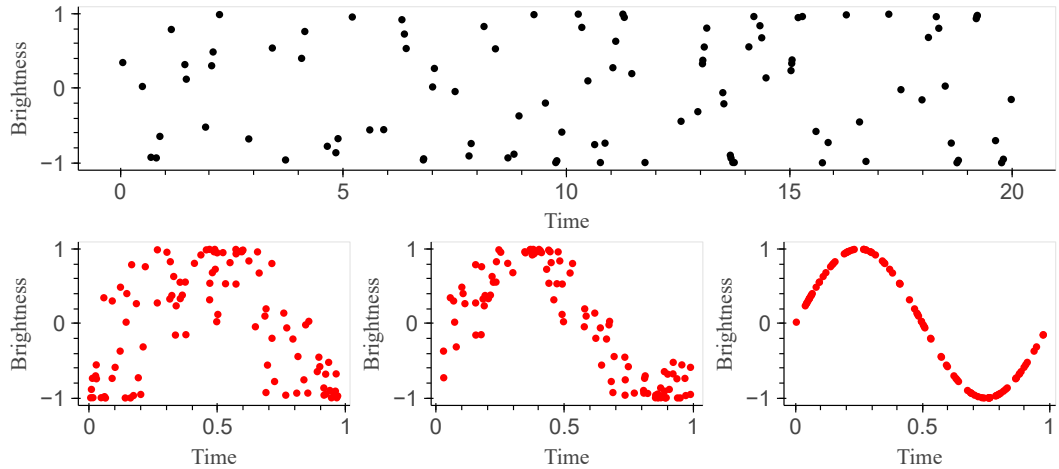


Figure 7.1: An example of the process of phase-folding in time-dependent data. Top panel: 100 randomly sampled points on a sine wave with a period  $P = 1$ . Bottom-left panel: data folded on a a period  $P = 0.98$ . Bottom-middle panel: data folded on a period of  $P = 0.99$ . Bottom-right panel: data folded on the true period of  $P = 1$ .

### 7.1.2.2 Phase Folding

Another way in which the periodicities of a system can be explored is via phase-folded light curves. Here, the system’s time-dependent photometry is ‘folded’ onto a chosen period, with the time dimension now being represented by ‘how far’ into a cycle each observation falls. Mathematically, folding is done by replacing the time component of a dataset with  $T \% P$ , where  $T$  represents the time of a given observation and  $P$  is the period on which the data is being folded. A demonstration of this is shown in Fig. 7.1. Here, 100 data points have been randomly sampled from a sine wave with a period  $P = 1$ , with no clear periodicity in the initial ‘light curve’. These points are then folded on periods 2%, 1% and 0% below the true period in the bottom-left, bottom-middle and bottom-right panels, respectively. This highlights the importance of using an accurate estimation of  $P$ , with these small offsets causing a significant reduction in the clarity of the resulting phase-folded light curves. Assuming  $P$  has been accurately determined, however, phase-folded light curves provide a clear means of enhancing the apparent signal-to-noise ratio in a given time-dependent data set, hence revealing the periodicities within.

### 7.1.3 Estimating the Rate of Mass Transfer

Another important parameter in compact binaries is the rate of mass transfer. In order for this to be relevant, the system must of course show some sign of

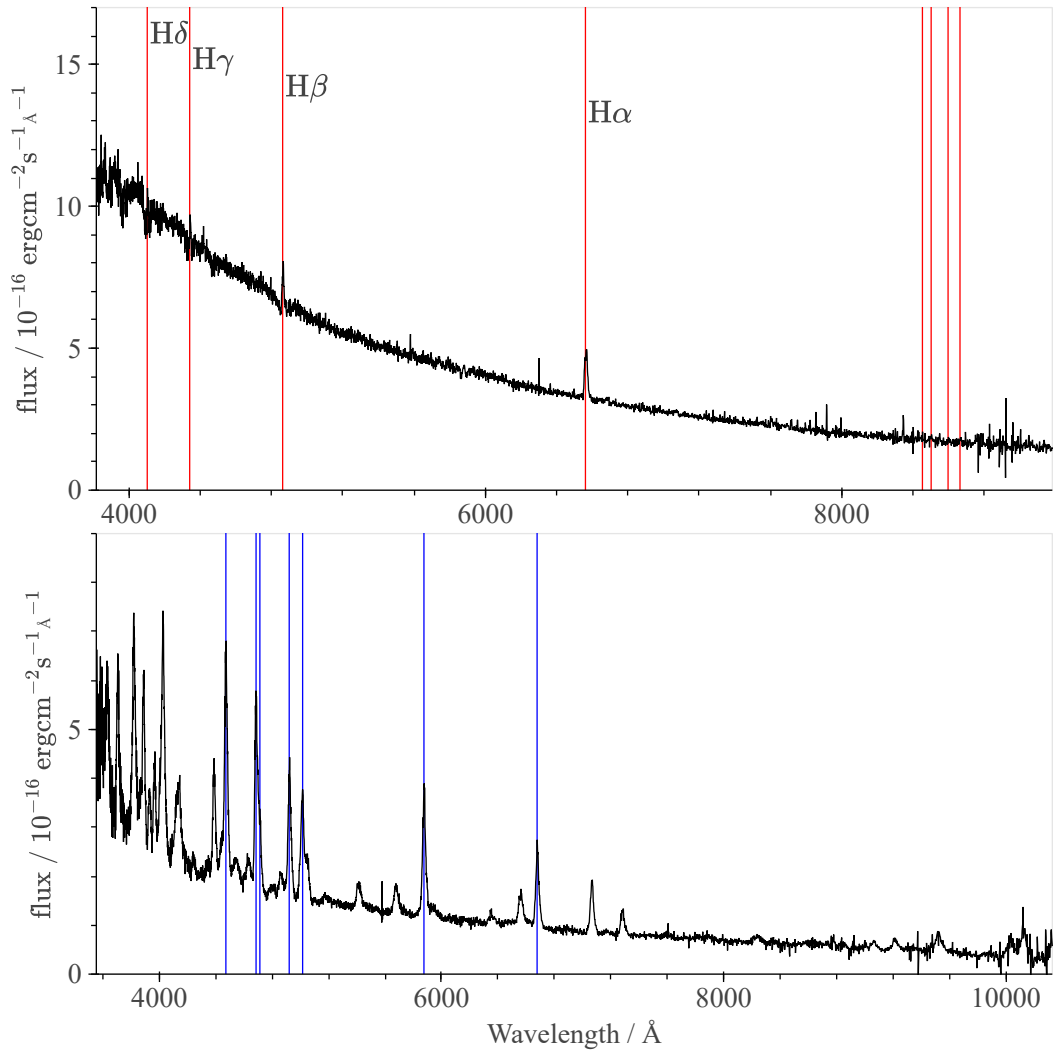


Figure 7.2: Top panel: SDSS spectrum of the novalike variable J075808.82+104345.50, which is dominated by the presence of a hot stable disc and hence exhibits  $H\alpha/H\beta$  emission lines and  $H\gamma/H\delta$  absorption lines. Bottom panel: SDSS spectrum of a known AM CVn system, J080449.49+161624.87, showing strong helium emission lines as a result of mass transfer from a helium-rich companion.

interaction—whether this be in its light curves (e.g. flickering, outbursts, pulsations) or in its spectroscopic properties (strong hydrogen emission lines, a significant disc component, high-energy emission, etc.). Given the role of mass transfer as a driver of these observable phenomena, a quantitative treatment of those that are present (i.e. a consideration of the frequency/magnitude of outbursts, the strengths of the emission lines/disc component or the magnitude of any high-energy emission) is key

to estimating the rate at which it occurs.

Another important property which wasn't mentioned above (but that does play a role in all of those which were due to its effect on the accretion geometry) is the magnetic field strength.

#### 7.1.4 Measuring the Magnetic Field Strength

The key to accessing a system's magnetic field strength can be found in spectral analysis. A spectrum shows a system's flux across a broad range of wavelengths, revealing information on its nuclear evolution through emission/absorption lines at characteristic wavelengths that indicate its temperature and elemental composition. The state of a system is reflected in its spectroscopic appearance, which differs during phases of quiescence/outburst. Furthermore, as the flux contributions from each component may dominate across different wavelength ranges, spectra can be used to reveal the identity of both components in a binary system—along with their relative contributions to the system's total luminosity. An example of this is shown in the top panel of Fig. 7.2, the spectrum of a known novalike variable [Inight et al., 2023]. This panel shows the spectrum of a hot accretion disc, exhibiting relatively weak Balmer line emission which, in  $H\gamma$  and the higher lines of the series, is embedded in absorption troughs. These arise from the optically thick disc, the spectrum of which can resemble that of hot stars (e.g. B-type stars or B-type subdwarfs). The fairly flat Balmer decrement (i.e. the relative strength of the Balmer lines towards the higher lines of the series) is another indication of a high-temperature gas, which results in the higher levels of hydrogen atoms being well-populated with electrons. The bottom panel of the same figure shows the spectrum of a known AM CVn system, which exhibits strong helium emission lines due to interactions with a hydrogen-deficient (and hence helium-rich) companion.

A further example is shown in Fig. 7.3, which is the spectrum of the same pre-polar featured in Fig. 4.10. This figure highlights the utility of spectra as a tool for identifying the nature of a given binary component, with the 'sawtooth'-like structure from  $\simeq 7000 - 9000\text{\AA}$  suggesting the presence of titanium oxide and vanadium oxide (TiO and VO, respectively). While the actual abundance of either of these molecules is rather small, both are very opaque and hence strongly absorbent. The morphology of this region is a strong indicator that the companion is an M-dwarf, as the hotter envelopes in larger, more massive stars do not allow the formation of these diatomic molecules [Rajpurohit et al., 2018].

Focusing now on the utility of spectra in probing magnetic fields, the Zeeman effect must be considered. The Zeeman splitting of spectral lines is a result of

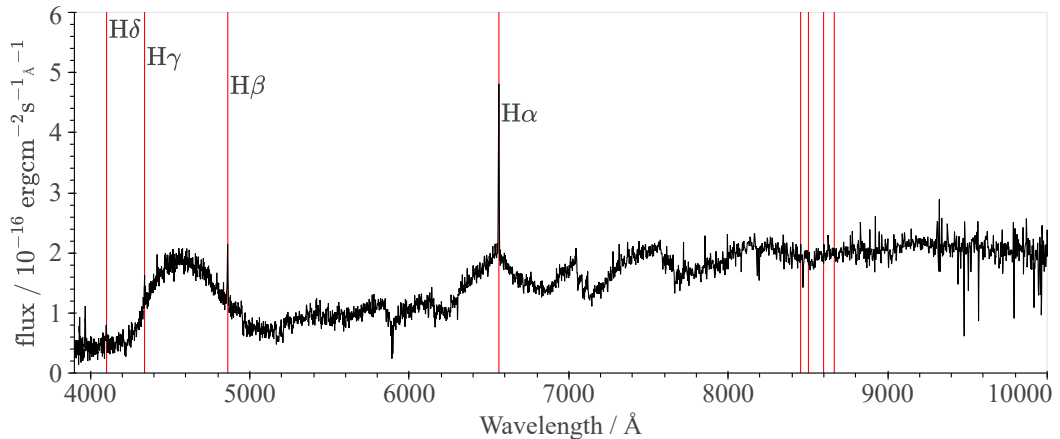


Figure 7.3: SDSS spectrum of the pre-polar J004924.50+222618.07, with a cyclotron feature at  $\simeq 4300 \text{ \AA}$  due to the presence of a strong magnetic field. The spectrum has a sawtooth-like structure in the range  $\simeq 7000 - 9000 \text{ \AA}$  as a result of absorption by titanium and vanadium oxides in the atmosphere of the M-dwarf companion.

a quantum-mechanical interaction of light with a strong magnetic field, with the magnitude of this splitting increasing with the magnetic field strength. An example is shown in the top panel of Fig. 7.4, which shows the spectrum of a strongly magnetic white dwarf. The bottom left and bottom right panels show Zeeman splitting of the  $H\alpha$  and  $H\beta$  absorption lines, respectively, by a magnetic field of  $B \gtrsim 1 \text{ MG}$  [Ny et al., 2017]. Figure 11 in Inight et al. [2023] shows how the observed magnitude of Zeeman splitting can be used to derive the magnetic field strength of a system.

Another indication of a strong magnetic field is the presence of cyclotron humps in a system’s spectrum. As noted in the discussion of magnetic cataclysmic variables, the deflection of charged particles by a strong magnetic field causes the emission of cyclotron radiation. This radiation occurs at the fundamental cyclotron frequency and its low-order integer multiples (harmonics). The particles that drive this emission are near-relativistic, and non-uniformity in their velocity relative to the observer causes Doppler broadening of these emission lines into ‘humps’ [Cropper et al., 1990]. The frequency of these cyclotron harmonics (and hence the central wavelengths of the cyclotron humps in a system’s spectrum) can be used to probe the magnetic field strength. Figure 7.5 shows cyclotron humps in the spectrum of a strongly magnetic cataclysmic variable. The lower panel of Figure 3 in Littlefield et al. [2023] shows how the modelling of cyclotron emission against the positions of cyclotron humps can be used to estimate the strength of a system’s magnetic field. The system featured here is the same as in Fig. 7.5.

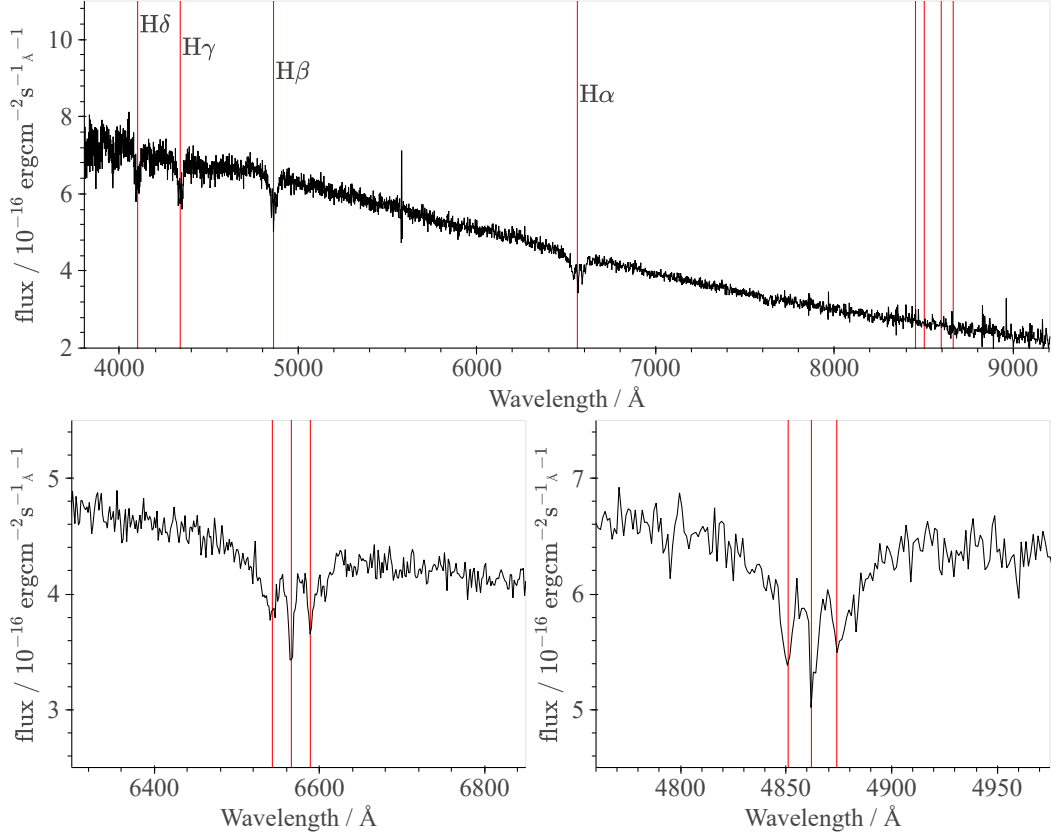


Figure 7.4: Top panel: SDSS spectrum of the magnetic white dwarf J085830.85+412635.12. Red lines show hydrogen absorption lines. Bottom-left panel: Zoomed in H $\alpha$  absorption line showing Zeeman splitting to form a triplet. Bottom-right panel: Zoomed in H $\beta$  line showing the same Zeeman splitting. The splitting of absorption/emission features is characteristic of a star with a strong magnetic field. Ny et al. [2017] suggest that the extent of Zeeman splitting in this system indicates a magnetic field strength of over 1 MG (an order of magnitude estimate).

### 7.1.5 Constraining the Mass of the Accretor

Given its utility as a separator between the different forms of compact accretors (white dwarfs, neutron stars and black holes), accurately estimating the accretor mass is of clear importance to system identification. This can be achieved via the binary mass function.

#### 7.1.5.1 The Binary Mass Function

Resulting from Kepler’s third law when the system’s orbital period and one of its components’ radial velocity is known, the binary mass function allows for the mass

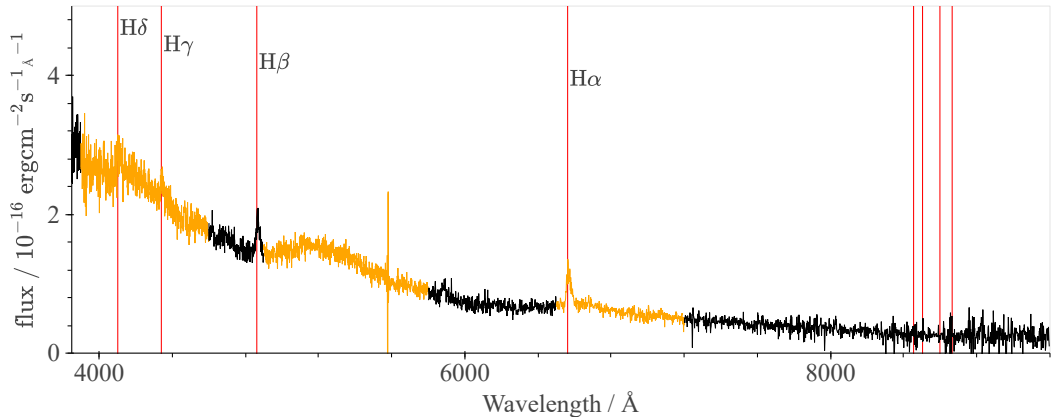


Figure 7.5: SDSS spectrum of the short-period magnetic cataclysmic variable J134441.83+204408.30. Orange: three cyclotron harmonics near 4200, 5200 and 6600 Å resulting from a magnetic field with an estimated strength of  $\simeq 56$  MG [Littlefield et al., 2023]. Red vertical lines: hydrogen emission lines.

of an unseen object in a binary to be constrained:

$$\frac{M_c^3 \sin^3 i}{(M_c + M_d)^2} = \frac{PK_d^3}{2\pi G}. \quad (7.1)$$

Here,  $M_c$  is the mass of the compact object and  $M_d$  is the mass of its companion,  $i$  is the orbital inclination,  $P$  is the orbital period,  $G$  is the gravitational constant and  $K_d$  is the semi-amplitude of the radial velocity of the donor star. The latter is typically measured through the Doppler shifting of spectral lines in the donor’s phase-resolved spectra. This equation sets a minimum mass on the compact object, which is reached for  $i = 90^\circ$  and  $M_d = 0$  [Marsh et al., 2016]. The reason for this being a lower limit is that in reality, the mass of the secondary in a binary system cannot actually be zero. Furthermore, it is extremely unlikely that the orbital inclination will take a value which exactly maximises  $\sin^3(i)$ . Any deviation from these extremes therefore necessarily increases the difference between the estimated mass and the true mass of the accretor. Of course, if the orbital inclination and/or the mass of the secondary is known then these assumptions need not be made. As the donor in a compact binary is usually a main sequence star, its mass can be estimated via its spectral type or the relevant mass-luminosity relation [Salaris and Cassisi, 2005].

### 7.1.5.2 Gravitational Wave Detections

Gravitational waves also provide a means of estimating the accretor mass, although the sensitivity of current detectors limits the applicability of this approach to only the strongest sources. This, combined with the fact that masses determined through extra-galactic detections are subject to large uncertainties as a result of cosmological redshift (redshift caused by the expansion of space as the wave propagates), means that the number of mass estimations via gravitational wave detections is currently very small. Nevertheless, the number of systems to which this method is applicable will grow as the sensitivity of detectors improves.

### 7.1.5.3 Limitations

Despite the utility of mass estimations in system identification, there are important limitations which must be highlighted. As noted previously, the mass limits in white dwarfs and neutron stars are set by the Chandrasekhar limit of approximately  $1.4 M_{\odot}$ , and an empirically derived (and hence ill-constrained) limit of  $\simeq 2.01 - 2.16 M_{\odot}$  [Rezzolla et al., 2018], respectively. The uncertainty in the latter results in the nature of accretors of mass  $2.01 \lesssim M_c \lesssim 2.16 M_{\odot}$  being difficult to confirm via mass estimation alone. Another limitation arises from the lower mass limit of neutron stars, which is similarly ill-constrained. Suwa et al. [2018] gives this lower limit as  $1.17 M_{\odot}$ , closely matching that of the least massive known neutron star (the theoretical lowest mass of a neutron star is actually expected to be around  $0.1 M_{\odot}$ , but no known mechanism could produce such an object and none have been observed to exist [Kaper et al., 2006]). Given that this is less than the maximum mass of a stable white dwarf, identifying the nature of a compact accretor with a mass  $1.17 M_{\odot} \lesssim M_c \lesssim 1.4 M_{\odot}$  can also be difficult. A final limitation is the paucity of compact objects in the ‘mass gap’ between neutron stars and black holes, leading to difficulties in the identification of accretors with masses in the range  $2 M_{\odot} \lesssim M_c \lesssim 5 M_{\odot}$  [Schochet et al., 2024; Barr et al., 2024]. Combined with their typically large uncertainties, mass constraints are therefore not always a sufficient means of identifying the nature of the accretor in isolation from other techniques (such as spectral profiles, or the presence/characteristics of pulsations).

## 7.2 The AstroToolkit Package

The goal of this work requires the analysis of an assortment of archival data for thousands of candidate systems. To facilitate this analysis, a Python package ‘As-

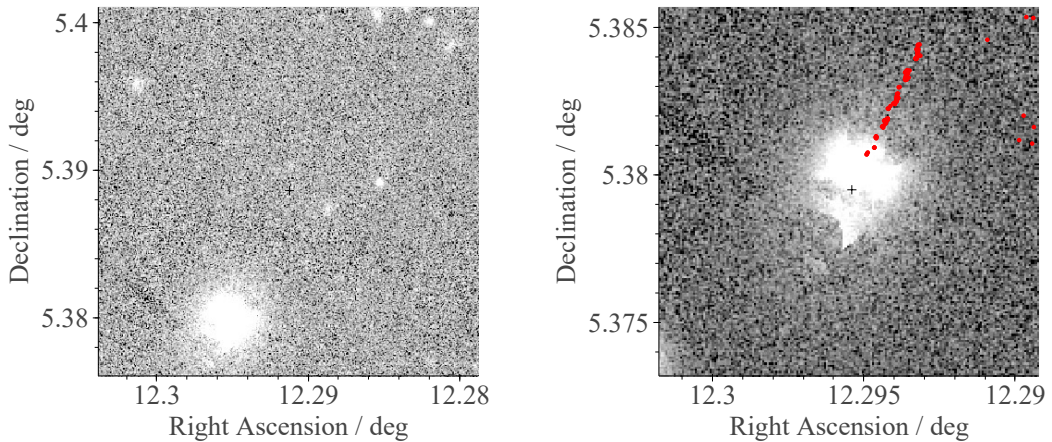


Figure 7.6: Images of the closest known single white dwarf to the Sun, J004909.90+052318.99, vMa2 [Burleigh et al., 2008]. This object has a total proper motion of  $2.98 \text{ arcsec yr}^{-1}$ , making matching of positional data difficult. Left panel: 90 arcsec Pan-STARRS image centred on the system’s J2000 coordinates. Right panel: 45 arcsec Pan-STARRS image using a Gaia source ID to target the system through the AstroToolkit package, which uses proper motion measurements to re-centre the image. An overlay of CRTS photometry is included, showing the system’s path through time.

troToolkit’ (henceforth ATK) was developed, which employs many of the above observational techniques<sup>1</sup>. The development of this package continued throughout the MSc and is still ongoing. ATK allows for the fetching, plotting and analysis of archival data from a variety of surveys, with the backbone of these being the Gaia survey.

With the launch of Gaia in 2013 by the European Space Agency, and its first data release in 2016 [Gaia Collaboration et al., 2016], a new era of astronomical data science began. Gaia provides positions, parallaxes, and proper motions of unprecedented precision in its mapping of nearly two billion objects in and beyond our Galaxy. The measurements of proper motion are of particular utility to ATK, as they are used throughout to more accurately map positional survey data to its host system. The amount of time for which positional data remains in alignment with the system to which it pertains is heavily dependent on the system’s proper motion. For systems with extreme proper motion, positional data can become unmatchable (without any correction) within a matter of only a few years. To target a given system, ATK therefore requires either its ‘position’ (right ascension and declination) or a Gaia DR3 (third data release) source ID. The latter is a unique identifier given

<sup>1</sup>The package is publicly available via [GitHub](#) or the [Python Package Index](#).

to each system by Gaia and is used by ATK to correct for any proper motion between the epochs of various surveys. An example is shown in Fig. 7.6, in which ATK corrects for proper motion between J2000 coordinates and the time at which a Pan-STARRS image was taken. This idea is used throughout ATK to ensure the retention of positional data for a given system, regardless of the epoch in which it was recorded. The following is a summary of the main ATK tools that were used in this work.

### 7.2.1 The Query Tool

This tool allows for the fetching of various types of archival data from many different surveys. Each type of query returns its data in a specific structure, which has been designed for use throughout the rest of the package. As noted above, all queries that are performed using a Gaia source ID to target a given system are corrected for proper motion to maximise the amount of returned data.

#### 7.2.1.1 Data Queries

These return all data for a given target, as listed in any Vizier catalogue. Vizier [CDS, 2024b] is the largest and most complete library of astronomical catalogues, currently providing access to over 25 000 catalogues. As an example, ATK can be used to retrieve Gaia data (astrometry, photometry, etc.) at a given position or for a given Gaia source ID. A number of commonly used surveys are built into ATK: The Panoramic Survey Telescope and Rapid Response System (Pan-STARRS), SkyMapper, Galaxy Evolution Explorer (GALEX), ROSAT, Sloan Digital Sky Survey (SDSS), Wide-Field Infrared Survey Explorer (WISE), Two Micron All Sky Survey (2MASS) and eROSITA.

#### 7.2.1.2 Reddening Queries

ATK also supports reddening queries from two different sources: SStructuring by Inversion the Local Interstellar Medium (STILISM) and Galactic Dust Reddening and Extinction (GDRE) [de Paris, 2024; IRSA, 2024]. While both of these tools aim to provide a reddening/extinction map, the method through which they achieve this differs. The former measures reddening as a function of distance primarily using stars with well-defined Gaia parallaxes [Capitanio et al., 2017], and hence the accuracy of its extinction map varies with the available number of suitable stars along a given line of sight. The latter uses dust emission to estimate the total

emission along every possible line of sight, but the accuracy of these measurements can once again vary.

### 7.2.1.3 HRD Queries

Hertzsprung-Russell diagrams (henceforth HRDs) are a key tool in astronomical data analysis, as they allow for the simple separation of different types of systems. An example was already seen in Fig. 4.13, where the three known white dwarf pulsars were shown to occupy a different region of the HRD to Delta Scuti stars—the classification which was initially given to AR Sco. ATK makes the generation of Gaia HRDs (i.e. HRDs that use Gaia’s photometry and astrometry) very easy, as it simply takes a set of Gaia source IDs and overlays these systems onto a clean 100 pc background sample (provided by B. Gänsicke).

### 7.2.1.4 Light Curve Queries

As has already been demonstrated, the analysis of light curves is an essential process in the classification of astronomical systems. This is even more so the case when the target is a binary system, as light curves reveal a great deal of information pertaining to outbursts, eclipses and other characteristic behaviour. Furthermore, the utility of time-dependent photometry in time series analysis allows for the orbital period, spin period and other periodicities present in a given system to be revealed. At the time of writing, ATK supports light curve queries to the Zwicky Transient Facility (ZTF), the Asteroid Terrestrial-impact Last Alert System (ATLAS), the All Sky Automated Survey for SuperNovae (ASAS-SN), the Catalina Real-Time Transient Survey (CRTS), the Transiting Exoplanet Survey Satellite (TESS) and Gaia. While most of these provide their photometry in magnitudes, TESS only provides fluxes in units of electrons (‘counts’) per second. These are then calibrated into magnitudes via

$$m_{\text{TESS}} = -2.5 \log_{10} f_{\text{TESS}} + 20.44, \quad (7.2)$$

where  $m_{\text{TESS}}$  is the apparent magnitude of the system in TESS and  $f_{\text{TESS}}$  is its reported flux in counts per second. This conversion uses a zero point of 20.44, which is derived from the fact that an object of magnitude  $m_{\text{TESS}} = 10$  is expected to be observed as a count rate of  $f_{\text{TESS}} = 15\,000$ . More information can be found in Fausnaugh [2025].

The primary time series photometry surveys used in this work are ZTF, ATLAS and TESS. ZTF queries use the ZTF API (see IRSA [2025]), which defaults to

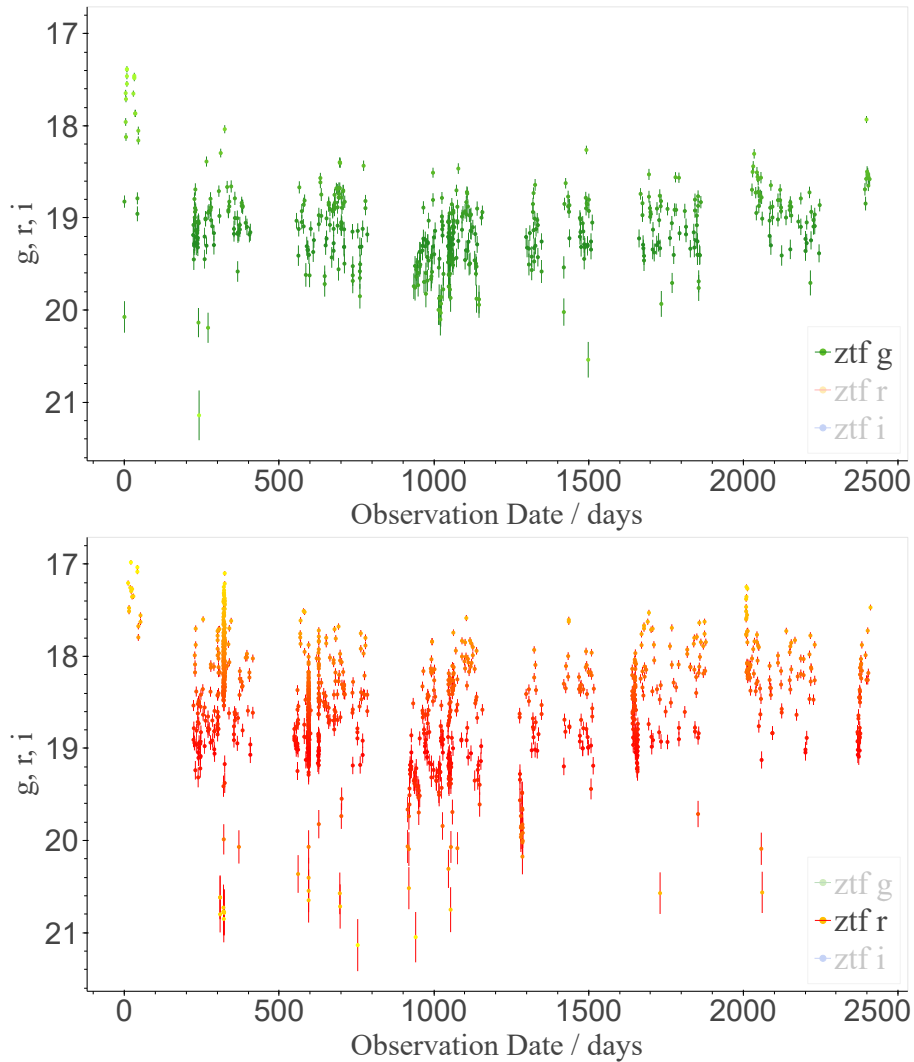


Figure 7.7: ZTF light curves of the cataclysmic variable J092444.48+080151.00, HU Leo, obtained and plotted using the AstroToolkit package. In the Bokeh version of this plot, each band can be interactively toggled using the figure legend. Top panel:  $g$ -band light curve. Bottom panel:  $r$ -band light curve.

the most recent public data release. At the time of writing, this is data release 22. ATLAS photometry is queried via the ATLAS Forced Photometry Server (see ATLAS [2025]). This is updated each day as new observations are made available, and hence ATLAS light curves span from the survey’s start date to the present day. TESS splits the sky into sectors, and hence the availability and recency of photometry for a given system depends on the sector in which it is located (see TESS [2025] for a full description). TESS queries support the retrieval of photometry up to the most recent data ingest in each sector (see STScI [2025c]).

All single-band light curves shown so far were collected using ATK, but the interactive plots produced by the package can display multiple bands at once which can be toggled using the legend. An example is shown in Fig. 7.7, where the ZTF  $g$  and  $r$ -band light curves of a cataclysmic variable are shown. These have been split into two plots here for visibility.

ATK also has built-in Lomb-Scargle periodogram routines which can be used to probe any periodicities in the time-dependent photometry of a given system. These were used in Fig. 4.12, which showcases the power spectrum and phase-folding functionality. Alongside these are the PyAOV routines, which have been integrated into ATK to provide access to alternative methods of time series analysis [Schwarzenberg-Czerny, 2024]. Of particular utility here is the analysis of variance (AOV) method. As with the Lomb-Scargle periodogram, this method is used to derive periodicities in unevenly sampled data. However, it is also effective in the analysis of data in which only a small number of observations are available [Schwarzenberg-Czerny, 1989]. PyAOV uses a variation of this method, namely the multi-harmonic analysis of variance (AOVMHW) routine, a full description of which can be found in Schwarzenberg-Czerny [1996]. PyAOV also supports other useful tools for time series analysis, such as detrending, which is used to remove long-term or instrumental trends in the data, and pre-whitening, which is used to identify lower amplitude frequencies by removing those which are more dominant.

### 7.2.1.5 Image Queries

ATK supports image queries to Pan-STARRS, SkyMapper and the Digitized Sky Survey (DSS). Pan-STARRS queries use the PS1 Image Cutout API (see STScI [2025b]), SkyMapper queries use the SkyMapper Image Cutout Service (see Australian National University [2025]) and DSS queries use the STScI DSS Form (see STScI [2025a]). Photometry from any supported photometry surveys can then be overlaid onto these images as a series of detections. An example has already been shown in Fig. 7.6, which uses a time-dependent photometric (‘tracer’) overlay. A further example is shown in Fig. 7.8, which utilises Gaia and GALEX photometric detections. The proper motion of the system is accounted for in both detections. For non-Gaia detections, this is done by ‘piggybacking’ them using any available Gaia astrometry. Here, e.g. for the GALEX detections seen in Fig. 7.8, the coordinates of all Gaia detections in the image are first transformed from Gaia’s epoch back to GALEX’s epoch. A search within a small radius (by default, 5 arcsec) is then performed at the coordinates of each of these detections, and any matching GALEX data is then carried with the Gaia detections to the epoch of the image.

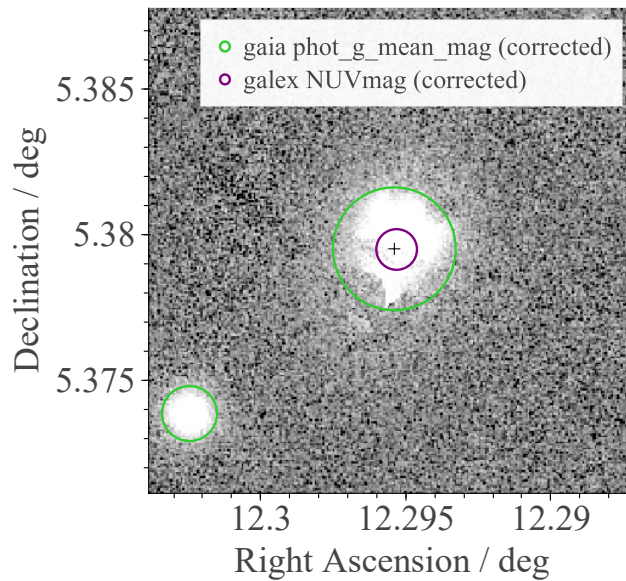


Figure 7.8: 60 arcsec image of the closest known single white dwarf to the Sun, J004909.90+052318.99,  $v\text{Ma}2$  [Burleigh et al., 2008]. This object has a total proper motion of  $2.98 \text{ arcsec yr}^{-1}$ , making matching of positional data difficult. Gaia  $g$  and GALEX  $NUV$  detections are overlaid, which are both corrected for the proper motion of the system by the AstroToolkit package.

This allows for any non-Gaia detections to be corrected for proper motion—even if the survey to which they pertain does not provide proper motion measurements.

#### 7.2.1.6 Spectrum Queries

At the time of writing, ATK supports queries to SDSS data release 17. When plotted, the resulting spectrum can be overlaid with the main elemental emission/absorption lines to assist in their identification. An example is shown in Fig. 7.9. In the interactive plots produced by the package, these lines can all be displayed separately or simultaneously in a single figure via the legend. They are shown separately here for visibility.

#### 7.2.1.7 Spectral Energy Distribution Queries

A spectral energy distribution (SED) describes the flux emitted by an object at different distinct wavelengths. Since these wavelengths are typically irregularly spaced and relatively far apart, SEDs are displayed as a set of individual measurements along with their uncertainties. A common use of SEDs is therefore the extension of spectra, albeit at a much lower resolution. Due to the differences in the emission

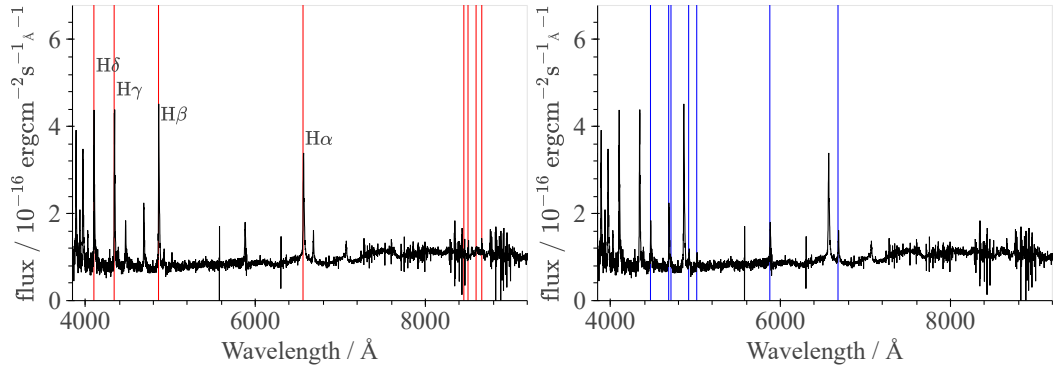


Figure 7.9: SDSS spectrum of the cataclysmic variable J092444.48+080151.00, HU Leo, obtained and plotted through the AstroToolkit package. Key spectral lines are overlaid, which can be interactively toggled using the figure legend in the Bokeh version of this plot. Left panel: spectrum with overlaid hydrogen lines. Right panel: spectrum with overlaid helium lines.

profiles of various stellar objects, SEDs offer particular utility in revealing the presence (and relative luminosity contribution) of a companion—much like their higher resolution counterpart. ATK facilitates the generation of SEDs using photometry from Gaia, Galex, SDSS, 2MASS, WISE, Pan-STARRS and SkyMapper Vizier catalogues, with included support for overlaying spectra. An example is shown in Fig 7.10.

## 7.2.2 The Bokeh Plotting Library

All ATK plotting functionality utilises the Bokeh plotting library [Bokeh, 2024]. There are two key reasons for this: interactivity and shareability. The former refers to the ability of Bokeh plots to be dynamically updated with user input. An example of this is the ability to hide legend elements (e.g. the different bands in light curve plots, spectral line identifiers in spectra, and detections in images) by clicking them in the legend. The legend itself can also be hidden dynamically to allow for unobstructed data analysis without introducing any ambiguity in what the data is showing. Further interactive features are included in most ATK plots, with a key example of this being implemented in images. Hovering over a detection marker in an ATK image reveals key information such as its position, magnitude and unique ID within the catalogue to which it pertains, and clicking on these markers opens the object in the SIMBAD database.

The latter, shareability, is also greatly enhanced by the ability for all Bokeh figures to be saved as static HTML documents. These can then be shared with others

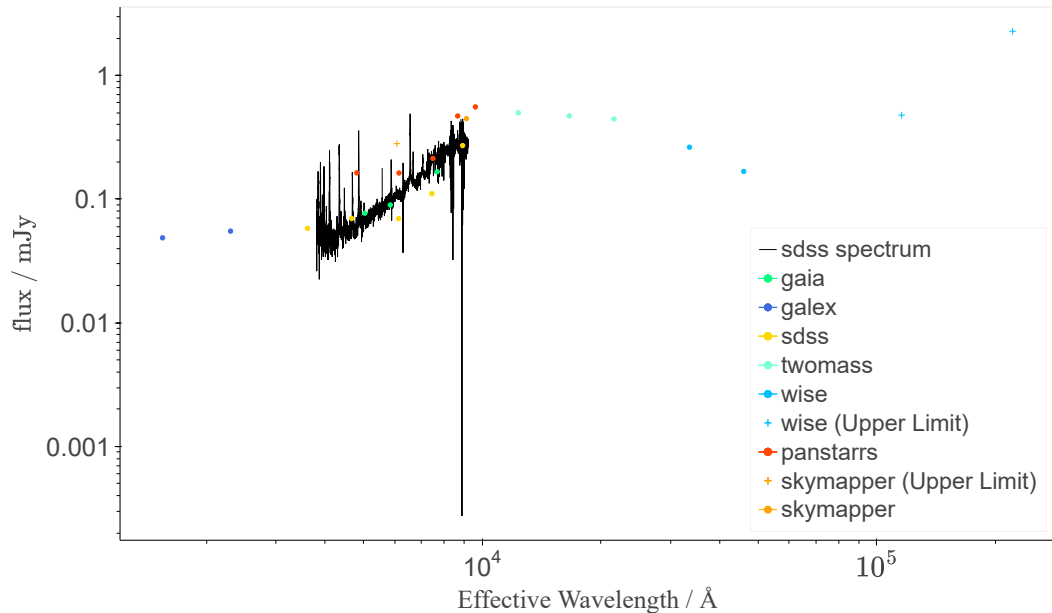


Figure 7.10: Spectral energy distribution of the cataclysmic variable J092444.48+080151.00, HU Leo, with an overlaid SDSS spectrum. Data was obtained and plotted through the AstroToolkit package.

while retaining all interactivity. This key difference in the retention of interactivity was the determining factor in the use of Bokeh over more commonly used plotting libraries.

One problem with Bokeh, however, is the size of its HTML pages when using large amounts of data—an often unavoidable complication. Examples include the plotting of power spectra in which a great number of sampling frequencies are used, HRD plotting and the plotting of light curves with a large number of photometric detections (such as those returned by TESS). This becomes especially relevant when multiple of these elements are combined in a single datapage. In this case, ATK can export any of its plots to PNGs using functionality provided by Bokeh, significantly reducing the file size at the cost of interactivity. This downside is generally not significant, however, as interactive elements in large HTML pages already become increasingly sluggish.

### 7.2.3 Matching Positional Data

Most of ATK’s queries are performed via a ‘cone search’ (i.e. the package searches for data within a given radius of the chosen position on the sky). As a result, if the radius of the query is large enough (or if the target region of the sky is sufficiently

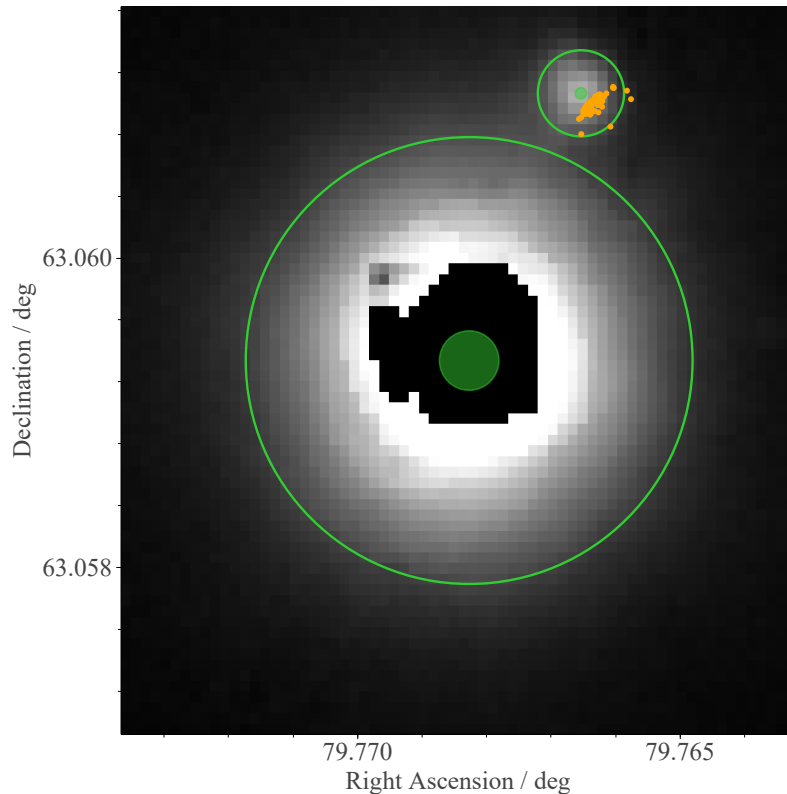


Figure 7.11: 27.5 arcsec Pan-STARRS image of J051903.99+630340.37 (top-right) and J051904.40+630334.14 (centre). The former is a cataclysmic variable which is in a hierarchical multiple with the latter, complicating the matching of positional data and leading to the contamination of available photometry. Gaia  $g$ -band detections are shown in green (radius scales with apparent brightness) and ZTF photometry (all bands) is shown in orange. The black region inside the central object is an artifact in the image, and has no physical meaning.

crowded), data for multiple sources may be returned. Fig. 7.11 shows one such system in which this may be the case: a CV (upper-right) and a bright star (centre) in a hierarchical multiple with a separation of only  $\approx 6$  arcsec. There are two main challenges that this system poses. Firstly, the distance between these objects means that even a relatively narrow query could return data that pertains to both. Secondly, the returned photometry itself may be contaminated by contributions from the nearby object—with the significance of this largely depending on the survey that is being used. For example, TESS has a pixel size of  $\approx 21$  arcsec [TESS Science Support Center, 2025], and hence its photometry would inevitably be affected by contamination in the case study presented here.

The accurate matching of positional data to a given source is a difficult and

nanced problem, and hence ATK cannot reasonably account for every challenge that may arise. The aforementioned tools, however, can assist the user in limiting their impact. The first of these problems can be minimised through the use of images with detection overlays, as featured in Fig. 7.11. For example, the Gaia and ZTF overlays used here reveal that both components have a Gaia detection, while only the CV has a ZTF detection. While this is already useful information, the interactive elements of ATK’s figures allow the user to push this further. As a reminder: in the interactive version of this image, hovering over a detection reveals its position, unique ID in the relevant catalogue/survey and some other basic information such as its magnitude. Clicking on these detections opens the object in the SIMBAD database, with the coordinates of this search being corrected to SIMBAD’s default epoch of J2000 to ensure consistent and accurate matching. By utilising these capabilities, data can be matched to its host system with far greater confidence—even in somewhat crowded regions. The second of the issues mentioned above (the contamination of photometry) is a more difficult one to solve, and this solution will largely depend on the catalogue being used. At the very least, however, the above steps help in making the user aware that this may be an important consideration.

#### 7.2.4 Datapages

While the various queries and plotting utilities outlined above simplify the gathering and analysis of astronomical data significantly, performing all of this separately for an object could still prove to be an arduous process. For this reason, ATK facilitates the generation of ‘datapages’ which allow for all of the above to be analysed simultaneously. These datapages can include any ATK figures (such as those discussed above) as well as any custom elements. ATK also includes some additional elements that are specifically intended for use in datapages, namely metadata tables and search buttons. The former stores any available data from ATK data queries, with default configurations containing basic astrometry and photometry being made available for simplicity. Any custom data may also be included. The latter provides buttons that search for a given system in SIMBAD [CDS, 2024a] or Vizier. SIMBAD, the Set of Identifications, Measurements and Bibliography for Astronomical Data, is a database of systems beyond our solar system. Where Vizier is a collection of catalogues, SIMBAD focuses on combining the most widely important data in these catalogues while also cross-referencing available literature. An example of a datapage which has been generated for the third white dwarf pulsar, J230641.47+244055.93, is shown in Fig. 7.12. The interactive version of this dat-

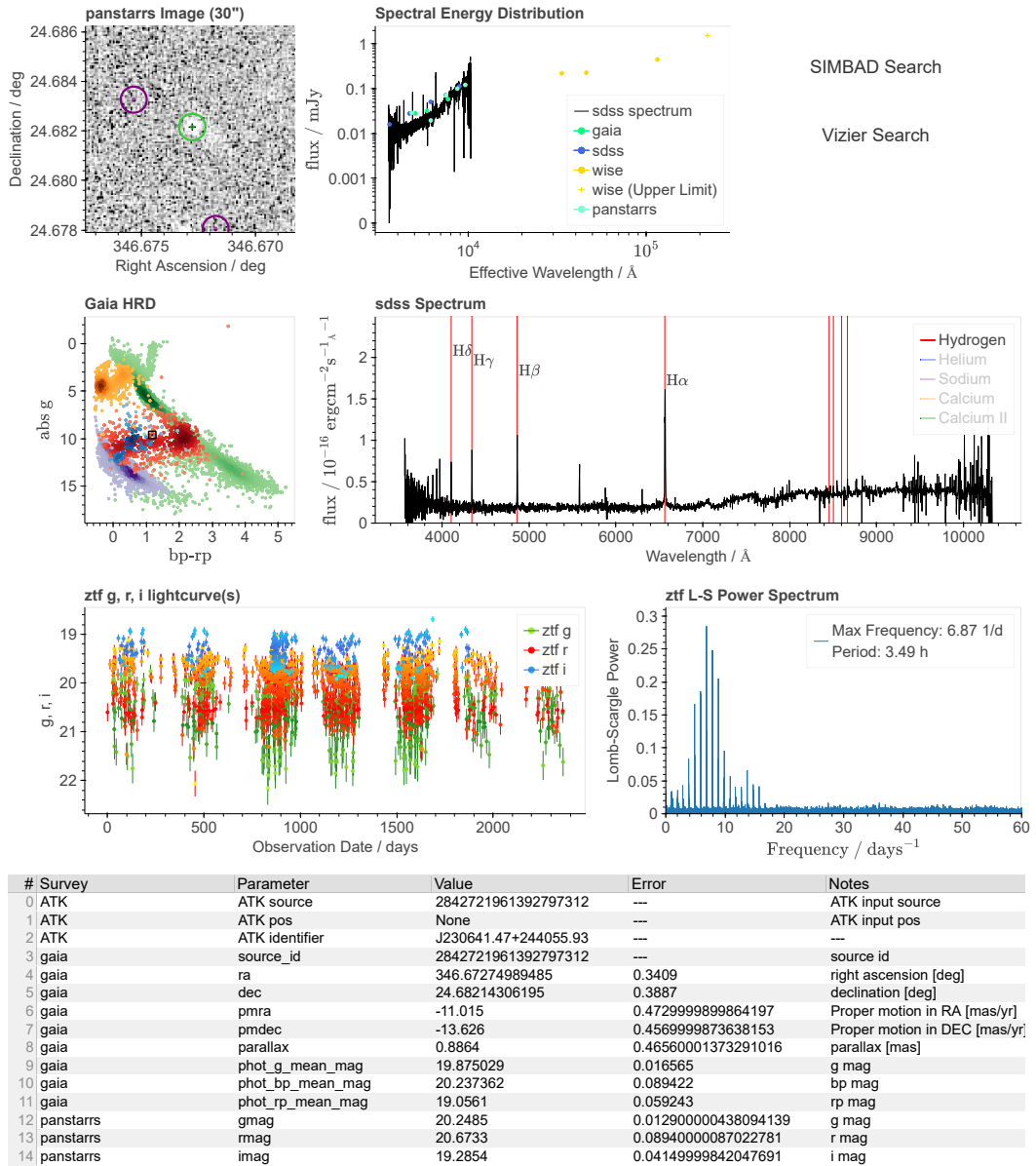


Figure 7.12: An example of a datapage for the third white dwarf pulsar, J230641.47+244055.93, generated by the AstroToolkit Python package. All panels and their interactive elements are described in the text.

apage includes all of the interactive elements that are featured in the individual panels.

### 7.2.5 Local Data Management

A further step towards the goal of shareability is taken with local file saving in ATK. Any data structure returned by any ATK query can be saved to local files, and these files can then be read back into ATK without any loss (i.e. the exact data structure that was used to generate the file is recreated upon reading it). Image data is saved as FITS files with any required information stored in the FITS image header, while other data types are instead saved as CSV files. This is of course also more widely useful outside of any collaborative purposes, allowing for data to be saved and reused at a later date.

### 7.2.6 Usability

More recent additions to the package have primarily been focused on improving both the package's ease of use and its applicability to various situations. One way in which this has been achieved is by introducing command-line integration and a graphical user interface (GUI). These make quickly retrieving, plotting and analysing any of the above data far easier, especially when handling a small number of systems. Scripts are then reserved for larger-scale or more specific use cases. Along with this, blank versions of all ATK data structures have been made accessible to the user. These can then be filled with relevant data from any source that is not directly supported by ATK, after which any of the package's plotting/analysis tools may be used.

For any further details, see ATK on [GitHub](#) or the [Python Package Index](#), where the package and its full documentation are publicly available.

## 7.3 STILTS

While ATK was used to carry out a great majority of this work, a small number of tasks required a tool that was specifically designed for the manipulation of extremely large tabular data: STILTS. The Starlink Tables Infrastructure Library Tool Set (STILTS) [Taylor, 2006] is a command line tool that allows for the processing and manipulation of tabular data. In particular, this work made use of its cross-matching and row-selection functionality. The former allows for two catalogues to be cross-matched by coordinates, combining any relevant data for a system if two matching observations are found within a given radius. The latter allows for the contents of these catalogues to be filtered by a given set of (numerical) criteria. A key reason for the use of STILTS is its speed, making it particularly useful in the initial selection of

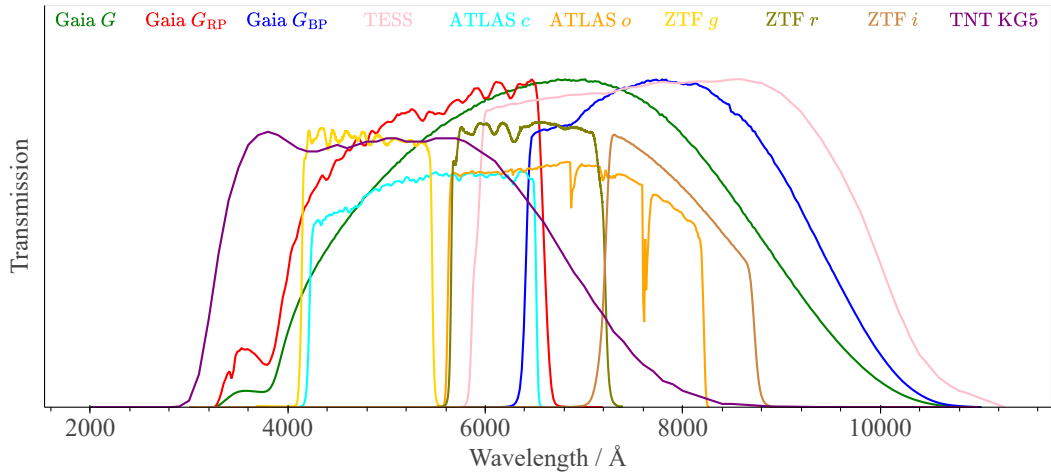


Figure 7.13: The transmission profiles of the main optical bands/filters used in this work.

systems from extremely large catalogues. As a reference, Gaia’s third data release contains nearly two billion rows. The tool and its documentation can be found at Taylor [2024].

## 7.4 Instrumentation

### 7.4.1 Optical Surveys

The primary optical surveys used in this work and their transmission profiles are shown in Fig. 7.13.

### 7.4.2 The Thai National Observatory

The Thai National Observatory hosts the Thai National Telescope (henceforth TNT), a telescope with a 2.4 m mirror used for optical astronomy. The TNT was used to gather ULTRASPEC high-speed photometry (a set of consecutive observations with a very small separation in time) for a number of candidates in the search for white dwarf pulsars. Here, the KG5 filter was used, the transmission profile of which is shown in Fig. 7.13. A full description of the telescope’s specifications can be found in TNO [2019], and a description of ULTRASPEC can be found in Dhillon et al. [2014].

All TNT photometry included in this work was gathered and reduced by Amornrat Aungwerojwit, Naresuan University, using the HiPERCAM pipeline (Marsh [2025]).

### **7.4.3 The Palomar Observatory**

The Palomar observatory hosts the Hale telescope, a telescope with a 5.1 m mirror that is used for a wide range of imaging and spectroscopic applications in the optical and near-infrared. In this work, the telescope was used to obtain optical spectra in the search for white dwarf pulsars. A full description of the telescope can be found in [Caltech, 2023].

### **7.4.4 The Lick Observatory**

The Lick Observatory is an astronomical observatory operated by the University of California. Among those hosted by the observatory is the Shane Telescope, a telescope with a 3 m mirror—making it the second largest telescope at the time of its construction, only behind the Hale Telescope discussed above. As with the Hale Telescope, the Shane Telescope was used to obtain optical spectra in the search for white dwarf pulsars. A full description of the telescope can be found in [Lick Observatory, 2021].

### **7.4.5 The BlackCAT Catalogue**

BlackCAT is a catalogue of X-ray binaries containing an expected or dynamically confirmed stellar mass black hole component, with the majority being detected via transient outbursts. The catalogue is updated regularly and can be found in [Corral-Santana, 2024]. As noted previously, the catalogue contains 53 expected and 19 dynamically-confirmed black hole X-ray binaries at the time of writing.

## Chapter 8

# The Search for White Dwarf Pulsars

### 8.1 Methodology

#### 8.1.1 Obtaining a Set of Candidates

The initial task in the search for white dwarf pulsars was to create a data set from which a set of candidates would be obtained. The ability of HRDs to separate astrophysical systems based on their observational properties showed significant utility as a starting point. Calculating the position of a system in the HRD requires an accurate estimation of its absolute magnitude and colour, with the former being given by

$$M = m + 5(\log_{10} \pi + 1)$$

where  $M$  is the system's absolute magnitude,  $m$  is its apparent magnitude and  $\pi$  is its parallax in arcseconds. As noted in chapter 7, all of these are provided by Gaia. The first step was therefore to locate the three known white dwarf pulsars in the Gaia HRD. As should be expected, all three systems are located in the region which is dominated by white dwarf–M-dwarf binaries. Utilising this, a ‘box’ in the HRD's parameter space was visually determined (see Fig. 8.1). Quantitatively, this took the form

$$\begin{aligned} 9 < G_{\text{abs}} < 11 \\ 1 < G_{\text{BP}} - G_{\text{RP}} < 1.5 \end{aligned}$$

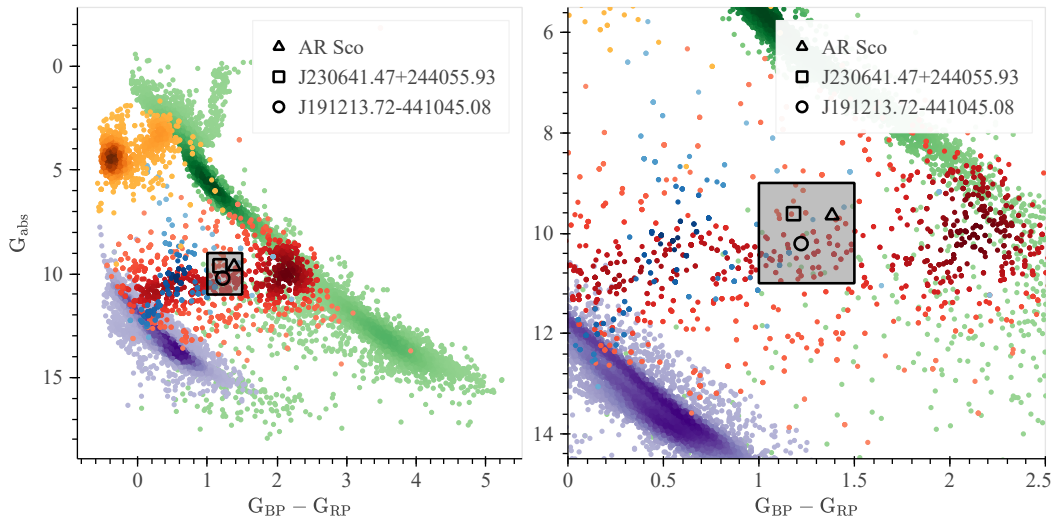


Figure 8.1: Left panel: Gaia Hertzsprung-Russell diagram showing the location of the three known white dwarf pulsars. A box is overlaid showing the selected region as described in the text. Right panel: the same figure as in the left panel, zoomed in on the selected region. The background (colour) sample is a 100 pc Gaia sample split into various sub-groups. Green: clean sample of stars, yellow: clean sample of spectroscopically confirmed subdwarfs, blue: clean sample of spectroscopically confirmed cataclysmic variables, red: clean sample of spectroscopically confirmed white dwarf + M-dwarf binaries, purple: clean sample of white dwarfs. Background samples provided by B. Gänsicke.

where  $G_{\text{abs}}$  is the system’s absolute Gaia G magnitude, and  $G_{\text{BP}}$  and  $G_{\text{RP}}$  are its apparent Gaia BP and RP magnitudes, respectively. This box encompasses the three known systems and defines the first cut which was applied to Gaia’s third data release.

Given the clear variability of the known white dwarf pulsars (Figs. 4.11 and 8.2), the next step was to remove non-variable systems. This was done through the use of the Gaia variability parameter, which was calculated as:

$$V_G = \frac{\sigma_G}{\bar{G}} n_{\text{obs},G}$$

where  $\bar{G}$  is the system’s mean flux in the G-band,  $\sigma_G$  is the error on this measurement, and  $n_{\text{obs},G}$  is the number of observations which contribute to the measured flux. The identity of the variability parameter as a measure of variability can be understood by considering the physical meaning of these measurements.  $\sigma_G$  is the standard deviation on the G-band flux normalized by  $\sqrt{n_{\text{obs},G}}$ , and so  $\frac{\sigma_G}{\bar{G}}$  provides a direct measurement of the ‘scatter’ of a system’s flux around its mean value—a mea-

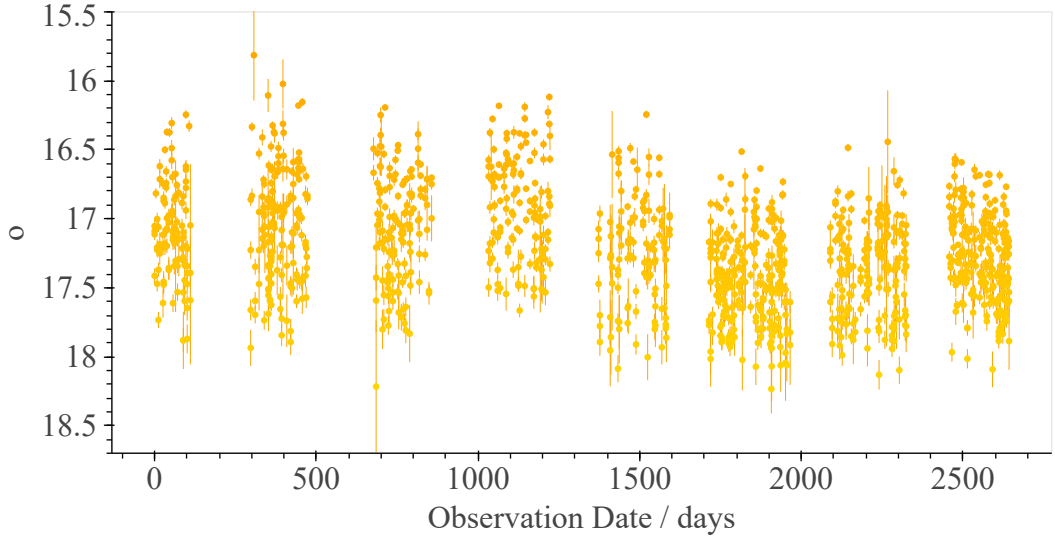


Figure 8.2:  $o$ -band ATLAS photometry of the second white dwarf pulsar to be discovered, J191213.72–441045.08, showing frequent pulsations in brightness of  $\simeq$  two magnitudes.

sure of variability by definition. As Gaia does not observe systems uniformly, the parameter is scaled by  $n_{\text{obs},G}$  to remove systems whose  $V_G$  is inflated by undersampled photometry. A discussion of the Gaia variability metric can be found in Guidry et al. [2021], but it is important to note that an additional factor of  $\sqrt{n_{\text{obs},G}}$  has been introduced here—placing greater emphasis on systems with a large number of observations and hence higher quality astrometry and photometry. This may lead to some systems of lower variability being included due to them having a larger number of observations, but the notably high values of  $V_G$  for the three known white dwarf pulsars (even if calculated according to Eq. 1 in Guidry et al. [2021]) suggests that this is unlikely to be a significant problem. For reference: if calculated using Eq. 1 in Guidry et al. [2021], the lowest value of  $V_G$  among the three known white dwarf pulsars is 0.294—almost double that of the most variable system shown in Fig. 1 of the same source.

A cut was defined using the Gaia variability parameters of the three known white dwarf pulsars as a reference, the values for which are shown in Table 8.1. The resulting cut took the form:

$$V_G > 3.$$

Further cuts were then imposed to ensure the removal of systems with poor astrometry. The first of these used the parallax significance and proper motion significance,

	<b>AR Sco</b>	<b>J191213.72–441045.08</b>	<b>J230641.47+244055.93</b>
ra	245.4471	288.0571	346.6727
dec	−22.8864	−44.1792	24.6821
$G_{\text{abs}}$	9.648	10.210	9.613
$G_{\text{BP}} - G_{\text{RP}}$	1.383	1.221	1.181
$V_G$	10.772	4.470	5.747
$\pi$	8.54	4.199	0.886
$\alpha_\pi$	227.226	51.394	1.904
$\mu$	52.393	19.930	17.521
$\alpha_\mu$	1366.289	180.675	38.170
RUWE	1.393	1.10	0.984
AEN	0.189	0.237	0.0

Table 8.1: Key Gaia parameters of the three known white dwarf pulsars. ra is the right ascension in degrees, dec is the declination in degrees,  $G_{\text{abs}}$  is the absolute Gaia  $G$  magnitude,  $G_{\text{BP}}$  and  $G_{\text{RP}}$  are the apparent Gaia  $BP$  and  $RP$  magnitudes, respectively,  $V_G$  is the Gaia variability parameter,  $\pi$  is the parallax in mas (milli-arcsec),  $\mu$  is the total proper motion in  $\text{mas yr}^{-1}$ ,  $\alpha_\pi$  is the parallax significance,  $\alpha_\mu$  is the proper motion significance, RUWE is the renormalised unit weight error and AEN is the astrometric excess noise. These were all used to define cuts in Gaia’s third data release.

given by

$$\alpha_\pi = \frac{\pi}{\sigma_\pi} \quad \text{and} \quad \alpha_\mu = \frac{\mu}{\sigma_\mu}, \quad (8.1)$$

respectively. Here,  $\pi$  and  $\mu$  are the parallax and total proper motion of the system, and  $\sigma_\pi$  and  $\sigma_\mu$  are the errors on these measurements. Through the corresponding values in Table 8.1, the following cuts were defined:

$$\alpha_\pi > 1.9$$

$$\alpha_\mu > 35.$$

The final two cuts used two further Gaia parameters: RUWE and astrometric excess noise. The former is the Renormalised Unit Weight Error, which describes the quality and reliability of a system’s Gaia astrometry. It is renormalised to account for the unit weight error’s strong dependence on a system’s brightness and colour. A full description of the parameter and its calculation can be found in Lindegren [2024]. The observed distribution of RUWE among Gaia sources (as shown in Fig. 12 of Lindegren [2024]) suggests a natural break point at  $\text{RUWE} \simeq 1.4$ . Gaia sources

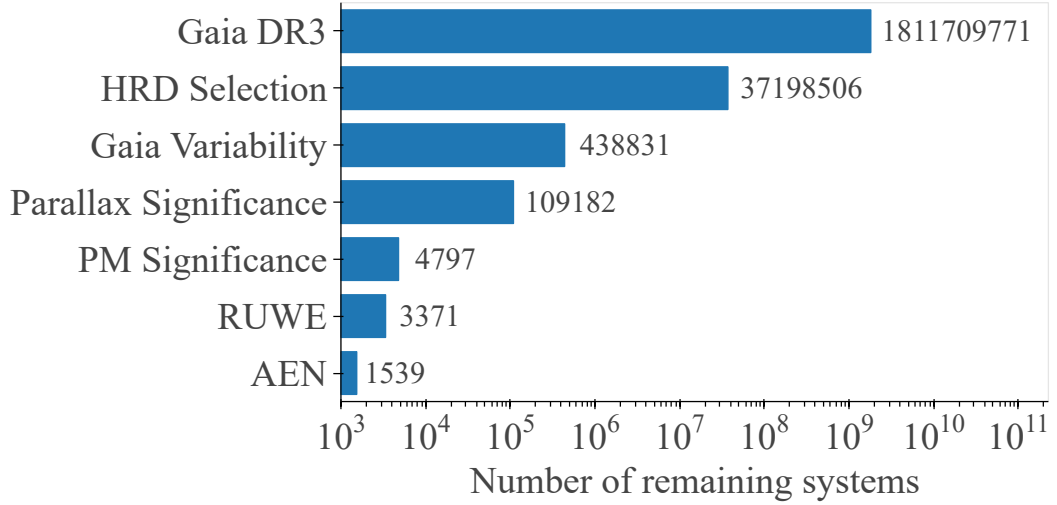


Figure 8.3: The number of remaining systems in the white dwarf pulsar search after each stage of filtering.

with a RUWE in the range  $0 \leq \text{RUWE} \leq 1.4$  are therefore expected to possess a ‘good’ astrometric solution and hence have well-defined astrometry. It is important to note, however, that a small RUWE does not necessarily indicate that the astrometric *uncertainties* of a system are similarly small (and vice versa) [Lindgren, 2024]. Hence, filtering systems by both the significance of their astrometric parameters ( $\sigma_\pi$  and  $\sigma_\mu$ ) and their RUWE is key to retaining only those with reliable astrometry of minimal uncertainty. Astrometric excess noise (henceforth AEN) is another parameter that measures the quality of the astrometric fit. This parameter is ideally zero, with positive values indicating disagreement of the astrometric fit with the observed astrometric parameters (within the confines of the assumed observational noise). However, as noted in Gaia Collaboration [2024], large AEN values alone do not *necessarily* indicate that a system is not astrometrically well-behaved. It is therefore important to define empirical cuts for any specific use case. The chosen values for the cuts in RUWE and AEN were once again derived from their corresponding values in Table 8.1. The following cuts were derived:

$$\text{RUWE} < 1.4,$$

$$\text{AEN} < 0.5.$$

The number of remaining systems following each cut in Gaia’s third data release is shown in Fig. 8.3, and the corresponding percentage decreases resulting from each

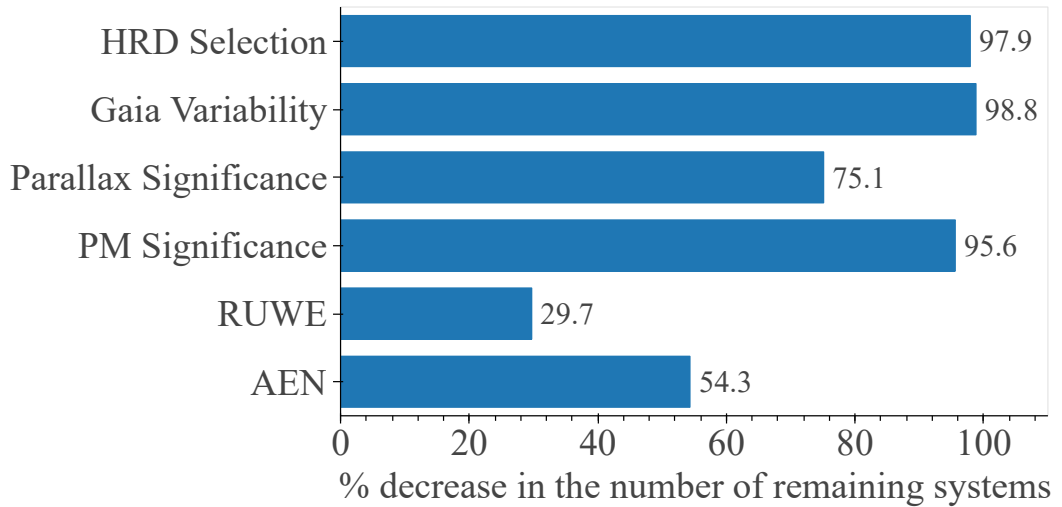


Figure 8.4: The decrease in the number of remaining systems caused by each criterion in the search for white dwarf pulsars, given as a percentage of the systems in the previous stage.

stage are shown in Fig. 8.4. The final set of candidate systems derived from these cuts was comprised of 1 539 systems.

### 8.1.2 Obtaining and Analysing Light Curves

Cone searches were then performed via ATK with a radius of 3 arcsec to retrieve any ZTF photometry among the candidate systems, of which 496 were successful. A large number of these queries returned no data, and this is largely due to ZTF’s declination limit of  $\gtrsim -30$  deg [Masci et al., 2020]. Of the 1 539 systems for which ZTF queries were attempted, 838 had a declination outside of ZTF’s detection limit. While this only explains around 80% of the 1 043 unsuccessful queries, it is likely an underestimate as the availability of photometry for systems approaching this limit becomes more sparse [Chen et al., 2020]. Any remaining queries failed due to their target system being too faint to be detected [Bellm et al., 2018]. Fig. 8.5 shows the number of successful/unsuccessful ZTF queries as a function of declination (top panel) and apparent Gaia  $G$  magnitude (bottom panel).

The light curves of the 496 remaining systems were then visually inspected, with any displaying behaviour similar to that of the known white dwarf pulsars being kept for further investigation. In particular, the most promising systems showed the same rapid, large amplitude ( $\sim 2$  mag) modulation in brightness. For reference: The light curves of AR Sco and J2306+2440 were shown in Figs. 4.11 and 7.12, and the light curve of J1912–4410 is shown in Fig. 8.2. Through this inspection, a set

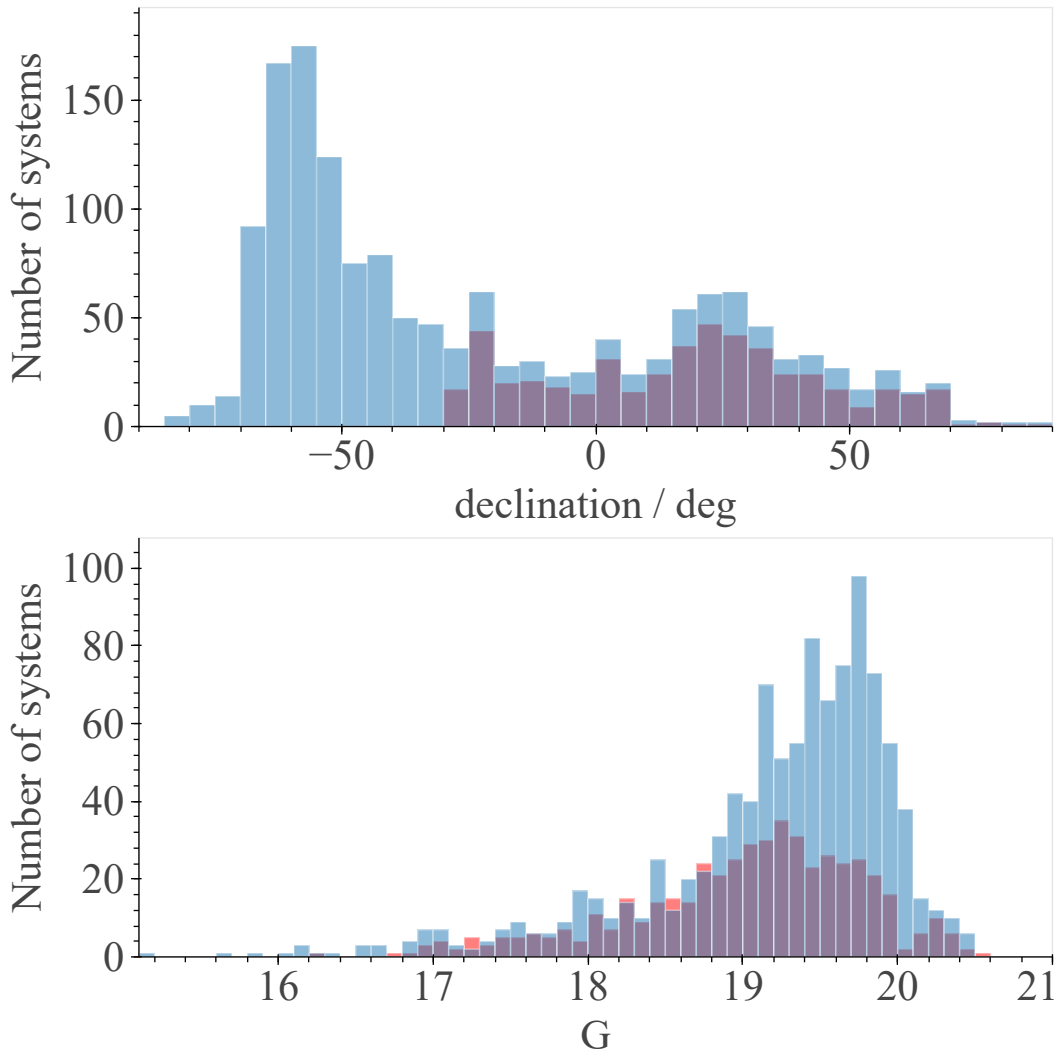


Figure 8.5: Top panel: distribution of the declination among systems with (red) or without (blue) available ZTF photometry. Bottom panel: distribution of the apparent Gaia  $G$  magnitudes in systems with (red) or without (blue) available ZTF photometry.

of 58 promising systems was derived. A full table of these systems can be found in Appendix A.

A datpage was then created for each of these systems through ATK, with each page being comprised of a 30 arcsec Pan-STARRS/SkyMapper image, a Gaia HRD (as in Figs. 4.13 and 8.1), an SED comprised of any available photometry (as in Fig. 7.10, see description of SEDs in ATK), an SDSS spectrum (if available), ZTF light curves in all three bands ( $g$ ,  $r$  and  $i$ ) and AOV MHW power spectra computed using PyAOV. The radius of all queries that were performed in this stage

System	Classification	Source
J022732.87+130617.09	Eclipsing Polar	Silva et al. [2015]
J035010.74+323229.72	Eclipsing Polar	Mason et al. [2019]
J065805.91−174424.97	Eclipsing Polar	Bernardini et al. [2019]
J095308.20+145836.44	Polar	Beuermann et al. [2021]
J103946.99−050658.32	Polar	Rawat et al. [2023]
J161007.51+035232.77	Polar	Rodrigues et al. [2006]
J172406.29+411407.69	Polar	Greiner et al. [1998]
J003854.80+611300.01	SU UMa CV	Boyd et al. [2010]
J013701.07−091234.72	SU UMa CV	Imada et al. [2006]
J170213.25+322954.16	SU UMa CV	Lukin et al. [2017]
J230538.37+652158.63	SU UMa CV	Thorstensen [2020]
J045944.04+192622.81	SU UMa CV	Kato et al. [2009]

Table 8.2: Known systems and their classifications identified in this work.

was 3 arcsec.

Finally, any published classifications across available literature were obtained through the use of SIMBAD’s bibliography tool. These were used alongside the above plots to further investigate each of the candidates, with the most promising or otherwise interesting systems being subjected to further analysis through high-speed photometry and optical spectra from the sources outlined at the end of Chapter 7.

## 8.2 Results

Among the final set of 58 candidate systems, twelve had published classifications. Seven of these were magnetic CVs (polars), while the remaining five were SU UMa systems (Table 8.2). Any remaining systems either had no corroborated classification or lacked details of how their classification was reached, with the majority having no literary information available at all. Two of the reference white dwarf pulsars (AR Sco and J230641.47+244055.93) were retained in the final set of candidates, with the third being lost due to a lack of coverage by ZTF. A selection of the most interesting candidate systems returned by this search will now be discussed. The orbital modulation, power spectrum and optical spectra of AR Sco are shown in Fig. 8.6 for reference.

### 8.2.1 J235354.93+415304.33

The first system identified in this work, GAIA DR3 1921680724575326464, is thought to be a low accretion rate polar (pre-polar). This system’s ZTF light curve is shown

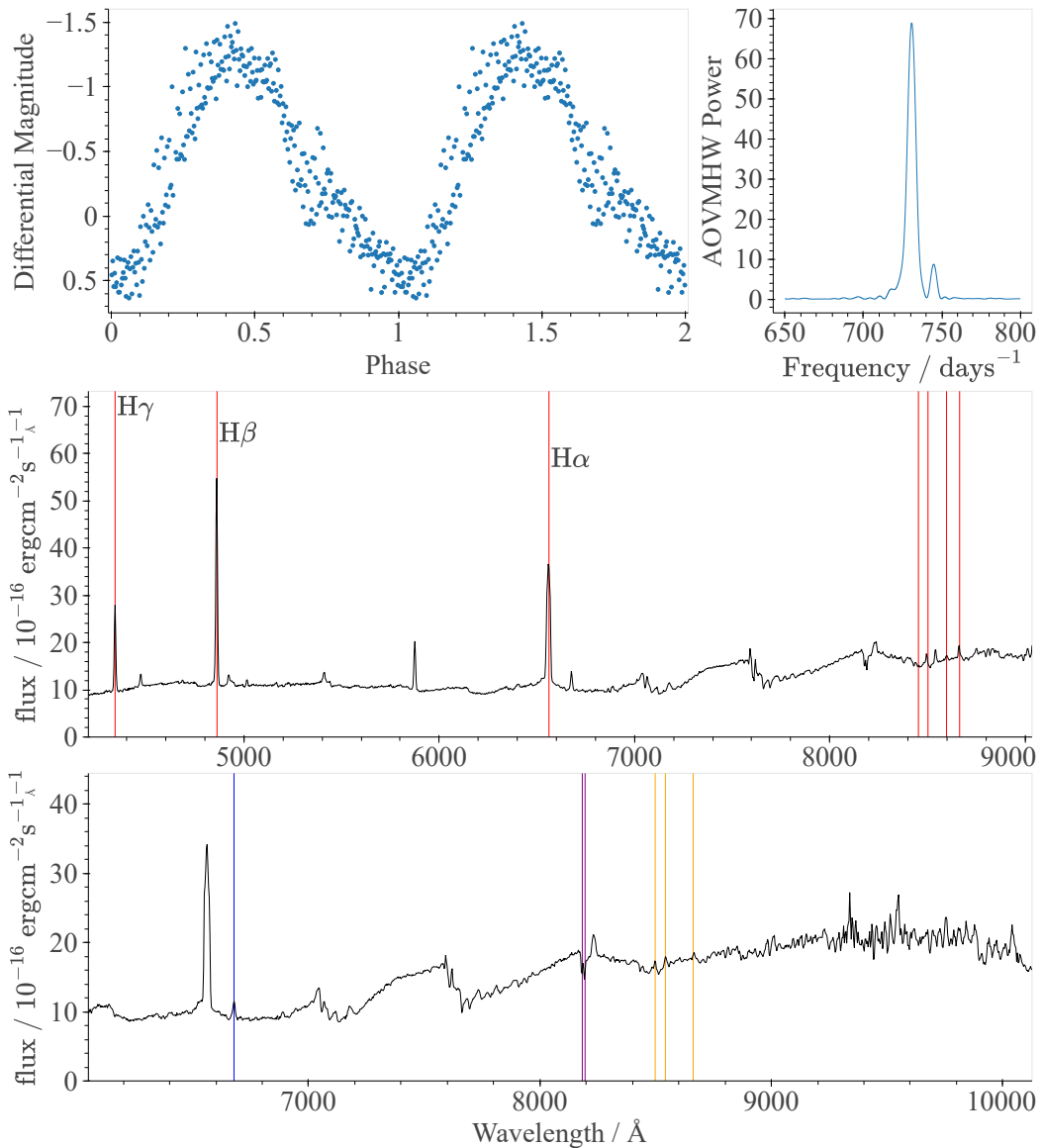


Figure 8.6: Various data of the first known white dwarf pulsar, AR Sco. Top left panel: TNT photometry, folded on the system’s orbital period of 3.56 h. Data is binned into 300 equally spaced bins in time. Top right panel: AOV MHW power spectrum of this TNT photometry, zoomed in on a signal of the white dwarf’s spin at 1.97 mins. Middle panel: Optical spectrum with hydrogen (Balmer) series overlayed. Bottom panel: Another optical spectrum, with helium (blue), sodium (purple) and calcium (orange) lines overlayed. In both spectra, the ‘sawtooth’-like structure resulting from absorption by titanium and vanadium oxides indicates the presence of an M-dwarf companion.

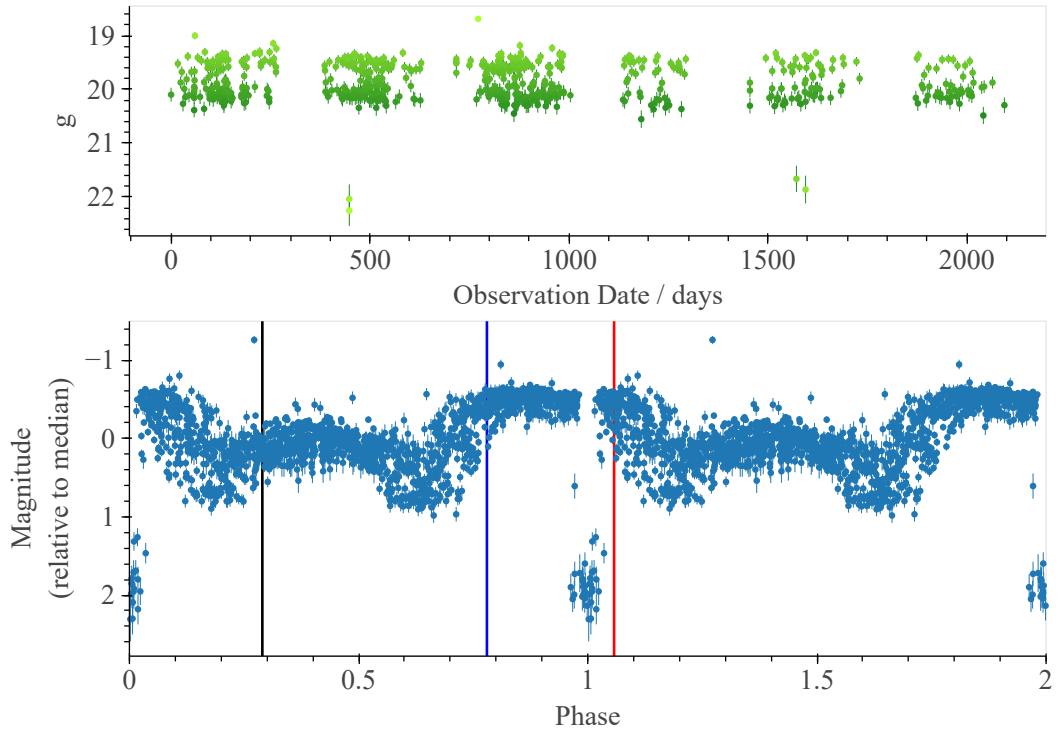


Figure 8.7: ZTF photometry of J235354.93+415304.33. Top panel:  $g$ -band light curve, showing its well-defined variation in brightness of  $\simeq 1 - 1.5$  mag, and eclipses of  $\simeq 2.5$  mag. Bottom panel: phase-folded light curve (all bands scaled and merged), showing its orbital modulation and eclipse. Photometry is folded on a period of 4.16 h using the Lomb-Scargle periodogram. Vertical lines indicate the orbital phases corresponding to the spectra that are shown in (Fig. 8.8).

in Fig. 8.7, which displays a well-defined range in brightness—much like the known white dwarf pulsars. Its orbital period was determined to be  $\simeq 4.17$  h through AOV<sub>MHW</sub> time series analysis. Its light curves are folded on this period in the bottom panel of Fig. 8.7, showing two sharply defined brightness states and eclipses of  $\simeq 2$  mag. The system shows little to no flickering—an accretion-induced phenomenon which is thought to arise from the dynamics of the disc. As a result, the accretion rate in this system is thought to be low.

At the time of writing, the system is not listed in SIMBAD. It has near-UV ( $NUV$ ) detections in GALEX, but a Vizier search returned no X-ray detections. This may be due to the position of the system, however, which has not been covered by any major X-ray survey which operates at a suitable sensitivity. The system is not listed in the latest Fermi [Abdollahi et al., 2020] (gamma-ray) source catalogues.

Initially, this system was thought to be a redback millisecond pulsar candidate due to the double-peaked, well-defined brightness states in its modulation—a

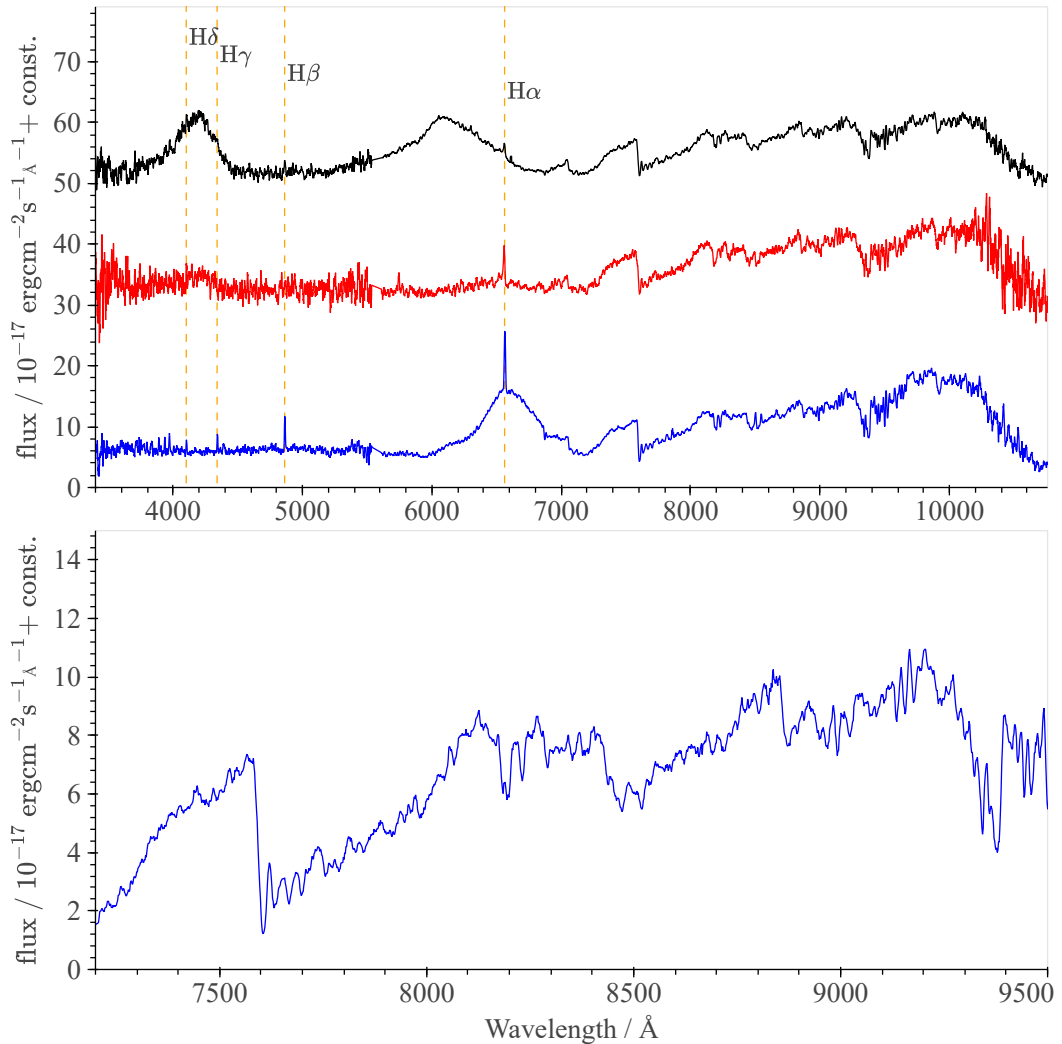


Figure 8.8: Top panel: phase-resolved spectra of J235354.93+415304.33, taken using the double spectrograph (DBSP) [Caltech, 2020] on the P200 (Hale) telescope [Caltech, 2023]. Data was gathered and reduced by Tony Rodriguez, Caltech, using the DBSP data reduction pipeline (Caltech [2025]). Each spectrum is the result of a 600 s exposure. The phase corresponding to the barycentric-corrected mid-exposure of each spectrum is represented in Fig. 8.7 by a vertical line of matching colour. The spectrum shown in red is scaled by a factor of three due to it being significantly more faint than those shown in blue and black. This is due to an overlap of the exposure with the eclipse, leading to a loss in flux. Hydrogen lines are overlaid. Bottom panel: Zoomed-in spectrum showing the ‘sawtooth’-like structure resulting from absorption by titanium and vanadium oxides in the atmosphere of the M-dwarf companion.

feature that is not typical of polars (e.g. Joshi et al. [2020]). Redbacks are mil-

lisecond pulsars with a young, low-mass companion ( $\lesssim 1 M_{\odot}$  [Strader et al., 2019]) and are hence a subtype of LMXB. Examples of the light curves of these systems are shown in Strader et al. [2019] and Salvetti et al. [2015]. Due to the closeness of their configuration, the surface of the companion in  $\simeq 50\%$  of redbacks is significantly irradiated by relativistic high-energy winds driven by the neutron star. This sheds material from its stellar envelope—in some cases destroying the star entirely [Turchetta et al., 2023]. Irradiation-dominated optical light curves typically show only one well-defined, high-amplitude maximum and minimum per orbital phase, as the companion shows its irradiated/non-irradiated side at the superior/inferior conjunction. Since this is not the case in Fig. 8.7, the degree of irradiation in this system is unlikely to be significant.

Phase-resolved spectra were then taken for the system using the 5 m Hale telescope, Palomar Observatory (Fig. 8.8). The spectrum shown in black displays a clear cyclotron hump at  $\simeq 6\,100 \text{ \AA}$  and a possible cyclotron hump at  $10^4 \text{ \AA}$ —indicating the presence of a strong magnetic field. The bottom panel of Fig. 8.8 highlights the ‘sawtooth’-like structure of the optical regions of the system’s spectra, indicating the presence of titanium and vanadium oxides. The system is therefore interpreted as having an M-dwarf companion—much like the known white dwarf pulsars. For reference, AR Sco’s optical spectra were shown in the bottom two panels of Fig. 8.6. The presence of cyclotron humps in this system’s optical spectra indicates without ambiguity that the system contains a strongly magnetic white dwarf, as cyclotron features in neutron stars are typically found at X-ray wavelengths [Staubert et al., 2019].

### 8.2.2 J045254.56+301718.00

Another system identified in this work is GAIA DR3 159891122647000192. The ZTF  $g$ -band light curve of this system is shown in the top panel of Fig. 8.9, showing well-defined variability of  $\simeq 1.5$  mag. There is also significant flickering in its phase-folded light curve (bottom panel of the same figure), and hence the system appears to support a high rate of mass transfer. AOVMHW analysis of the system’s ZTF photometry suggests an orbital period of 1.32 h, but the true period is expected to be double this for reasons that will be explained below. At the time of writing, the system is not listed in SIMBAD. It has both  $NUV$  and far-UV ( $FUV$ ) detections in GALEX, but there were no X-ray detections listed in VizieR and no gamma-ray detections in the latest Fermi catalogues.

Further photometry was obtained for this system through the TNT, which is shown in the top panel of Fig. 8.10. This photometry is folded on a period of 2.68 h

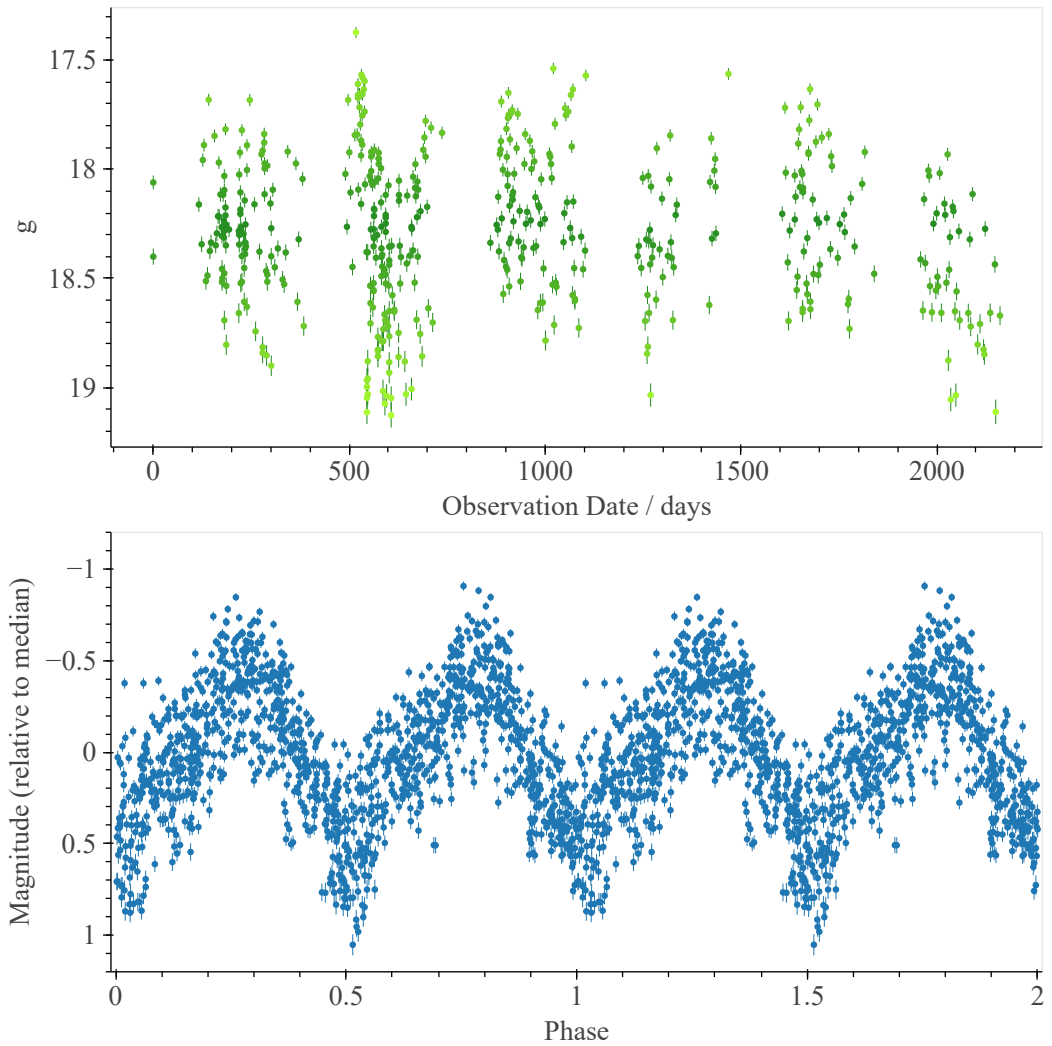


Figure 8.9: Top panel: ZTF  $g$ -band light curve of J045254.56+301718.00, showing its well-defined variability of  $\simeq 1.5$  mag. Bottom panel: phase-folded ZTF light curve, folded on a period of 2.64 h.

in the bottom panel of the same figure, which is expected to be the true orbital period of the system due to the clear asymmetry in consecutive quadratures (peaks in brightness as the binary components are side-by-side relative to the observer). Time series analysis of the TNT photometry obtained for this system did not reveal any strong signal of the accretor’s spin. As highlighted by the grey regions in Fig. 8.10, there are distinct steps in its modulation. While the cause of this is not immediately apparent from the top panel of Fig. 8.10, its phase-folded light curve reveals that this may be a sharp eclipse in the orbital modulation. A spectrum was then obtained for this system using the 3 m Shane Telescope, Lick Observatory,

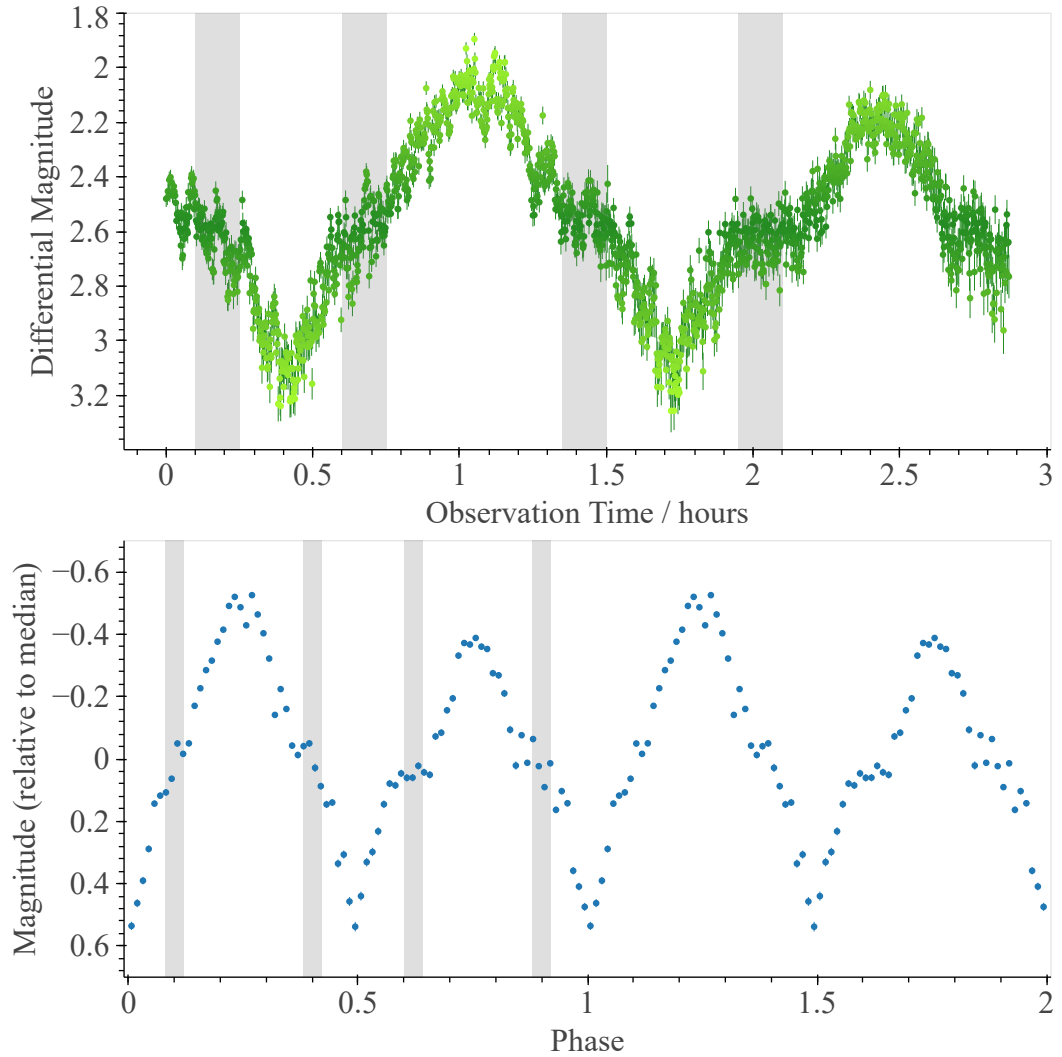


Figure 8.10: Top panel: TNT light curve of J045254.56+301718.00. Bottom panel: phase-folded TNT light curve, folded on a period of 2.68 h. Data is binned into 80 equally spaced bins in time. Grey regions highlight distinct steps in the system's rise and fall in brightness.

which is shown in Fig. 8.11. Hydrogen (Balmer) and helium lines are present and are broadened by the large velocity dispersion in the disc/accretion stream (e.g. compared to those of AR Sco in Fig. 8.6, which are significantly more narrow due to their chromospheric origin). This further supports the conclusion that this system is interacting.

Despite the similarity of its light curves to those of AR Sco, the lack of a signal from the rapid spin of the white dwarf suggests that this system is some other form of interacting, eclipsing white dwarf binary.

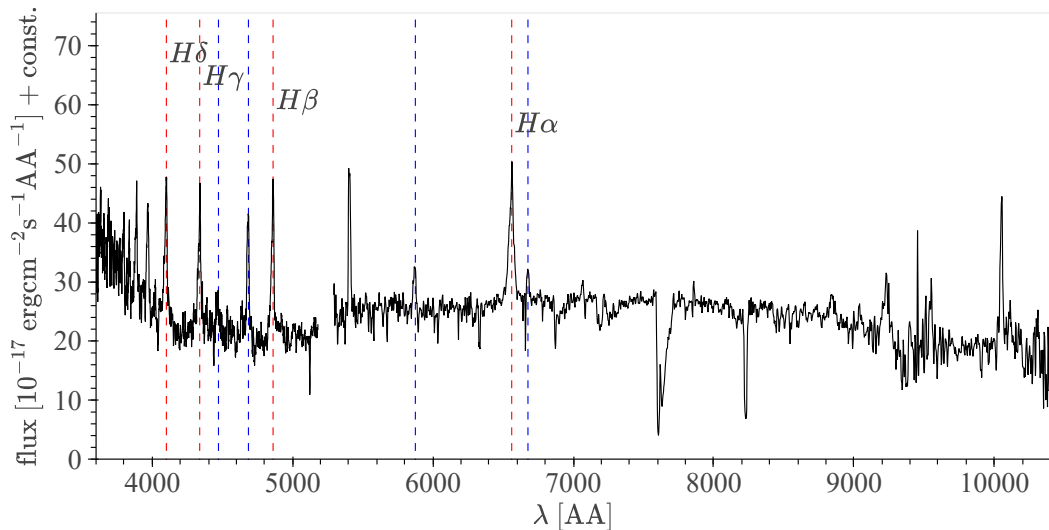


Figure 8.11: Spectrum of J045254.56+301718.00, taken using the Kast double spectrograph on the 3 m Shane telescope, Lick Observatory, with a 1 200 s exposure [Lick Observatory, 2021]. Data was gathered and reduced by Tony Rodriguez, Caltech. Hydrogen (Balmer) and Helium spectral lines are overlaid.

### 8.2.3 J035055.99–204815.82

A third system identified in this work is GAIA DR3 5093945085525624448, which is thought to be a young stellar object (YSO). The system has GALEX *NUV* and *FUV* detections, but no X-ray or gamma-ray detections are listed in Vizier. Its ZTF and TESS light curves were fetched via ATK with a search radius of 3 arcsec, and are shown in the top and middle panels of Fig. 8.12. These exhibit significant variability of up to four magnitudes. Notably, time series analysis of either set of photometry reveals no periodicity. The system appears to have been in a state of standstill for  $\gtrsim 7.5$  d (Fig. 8.12, bottom panel), which is followed by a significant outburst of over three magnitudes. Beyond this, the system does not recover to a comparably stable state.

Based on the extreme frequency and magnitude of its brightness variation, the system was initially thought to be an ER UMa candidate. However, its position in the Gaia HRD does not support this conclusion (Fig. 8.13). It was then realised that this system was flagged in Pala et al. [2020] as a YSO that had previously been mistakenly identified as a CV. Further investigation was then carried out to confirm or refute this classification. Since YSOs are formed in dense star formation regions, the position of a system in space relative to these regions can be a strong indicator of the likelihood of it being a YSO. Zari et al. [2018] provides a catalogue of YSOs,

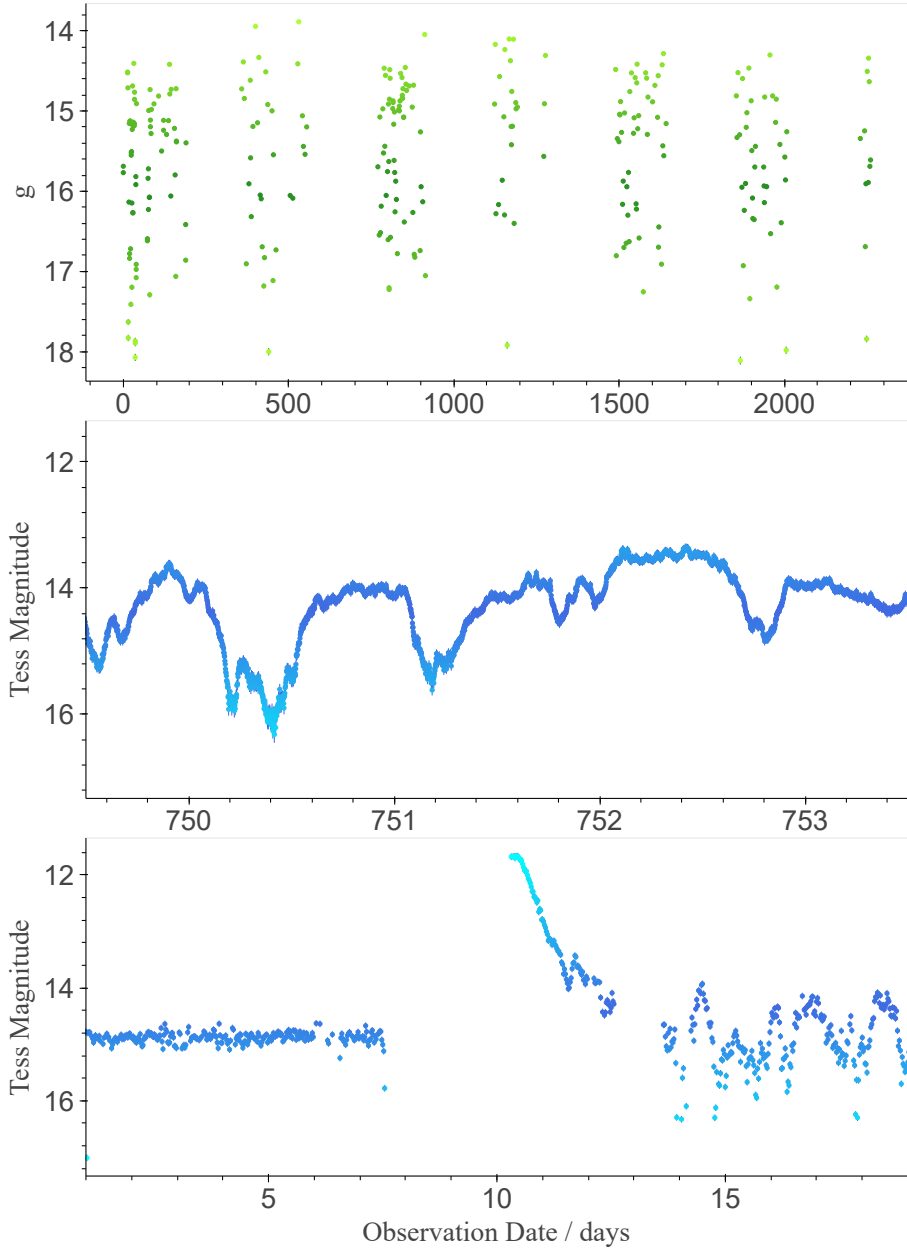


Figure 8.12: Light curves of J035055.99–204815.82, an expected young stellar object identified in this work. Top panel: ZTF *g*-band light curve, showing well-defined variability of  $\simeq 4$  mag. Middle panel: TESS light curves showing the system’s unpredictable short-term variability. Bottom right panel: TESS light curve focused on a large outburst of  $\simeq 3.5$  mag following a period of (relative) standstill.

and these are mapped in Fig. 8.14. The location of this system with a distance of  $\frac{1}{\pi} \simeq 126$  pc places it directly in a cluster of YSOs. As a result, the classification given to the system in [Pala et al., 2020] appears to be correct.

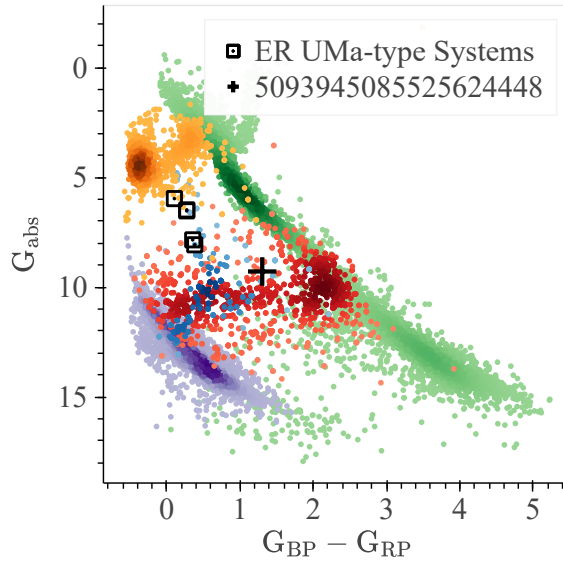


Figure 8.13: Gaia HRD showing the positions of known ER UMa-type systems and J035055.99–204815.82, a system identified by this work. The background (colour) sample is a 100 pc Gaia sample split into various sub-groups. Green: clean sample of stars, yellow: clean sample of spectroscopically confirmed subdwarfs, blue: clean sample of spectroscopically confirmed cataclysmic variables, red: clean sample of spectroscopically confirmed white dwarf + M-dwarf binaries, purple: clean sample of white dwarfs. Background samples provided by B. Gänsicke.

Despite the classification of this system being known, the question remains as to the nature of its extreme brightness variation. As discussed in Cody et al. [2017], YSOs are thought to exhibit the same disc instability outbursts as in dwarf novae and XRBs. Based on its morphology, the spike in brightness shown in the bottom panel of Fig. 8.12 appears to be one such outburst. While the duration of this outburst is within the expected range for YSOs [Cody et al., 2017], its magnitude is extreme.

Another known source of variability in YSOs is extinction by circumstellar material, which causes the brightness of the system to ‘dip’ from its baseline [Cody et al., 2014]. Importantly, this ‘dipping’ has been observed to occur aperiodically—much like the variability exhibited by this system. Figure 11 in Cody et al. [2014] shows the light curves of aperiodically dipping YSOs. The similarity to what is observed for this system is clear, although it is important to note that the observed magnitude of these variations is once again extreme. While not conclusive, this prescription does successfully describe the aperiodicity, frequency and apparent randomness in the system’s brightness variation. Whether or not the initial outburst is responsible for the onset of this behaviour (as perhaps suggested by the bottom

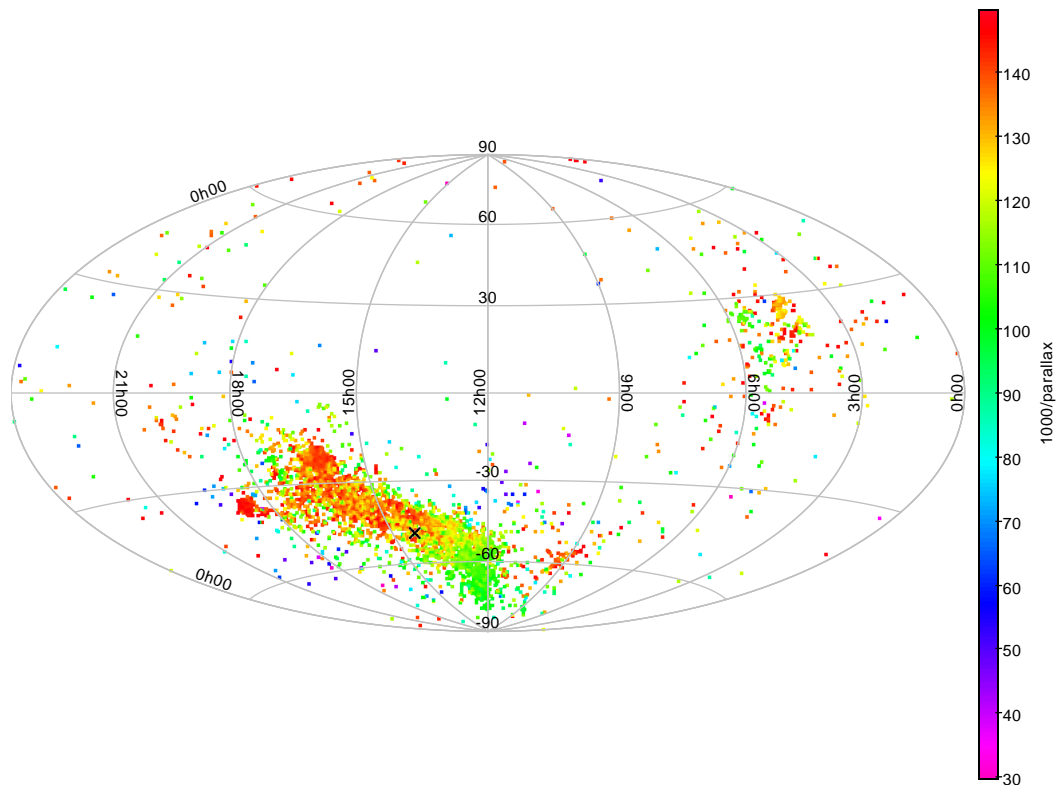


Figure 8.14: Position of J035055.99–204815.82 (black) relative to a set of young stellar objects, which are coloured by their distance. The distance of J035055.99–204815.82 is  $\simeq 126$  pc, placing it in a cluster of young (pre-main sequence) stars.

panel of Fig. 8.12) remains unclear.

#### 8.2.4 J201135.84–021340.49

This system, Gaia DR3 4223502720986764672, is a promising white dwarf pulsar candidate. At the time of writing, this system is not listed in SIMBAD. It has no known GALEX or X-ray detections and no gamma-ray detections are listed in the most recent Fermi catalogues. The ZTF  $g$ -band light curve of this system is shown in the top panel of Fig. 8.15, exhibiting well-defined variability of a similar magnitude to AR Sco. Its phase-folded light curve is shown in the bottom panel of the same figure, which is folded on a period of 3.73 h as suggested by its AOVMMHW power spectrum. Its modulation shows no clear asymmetry when folded on the first harmonic of this period, so this may be the true orbital period of the system. The modulation of this system is noisy, particularly near its maxima. If this is a result of

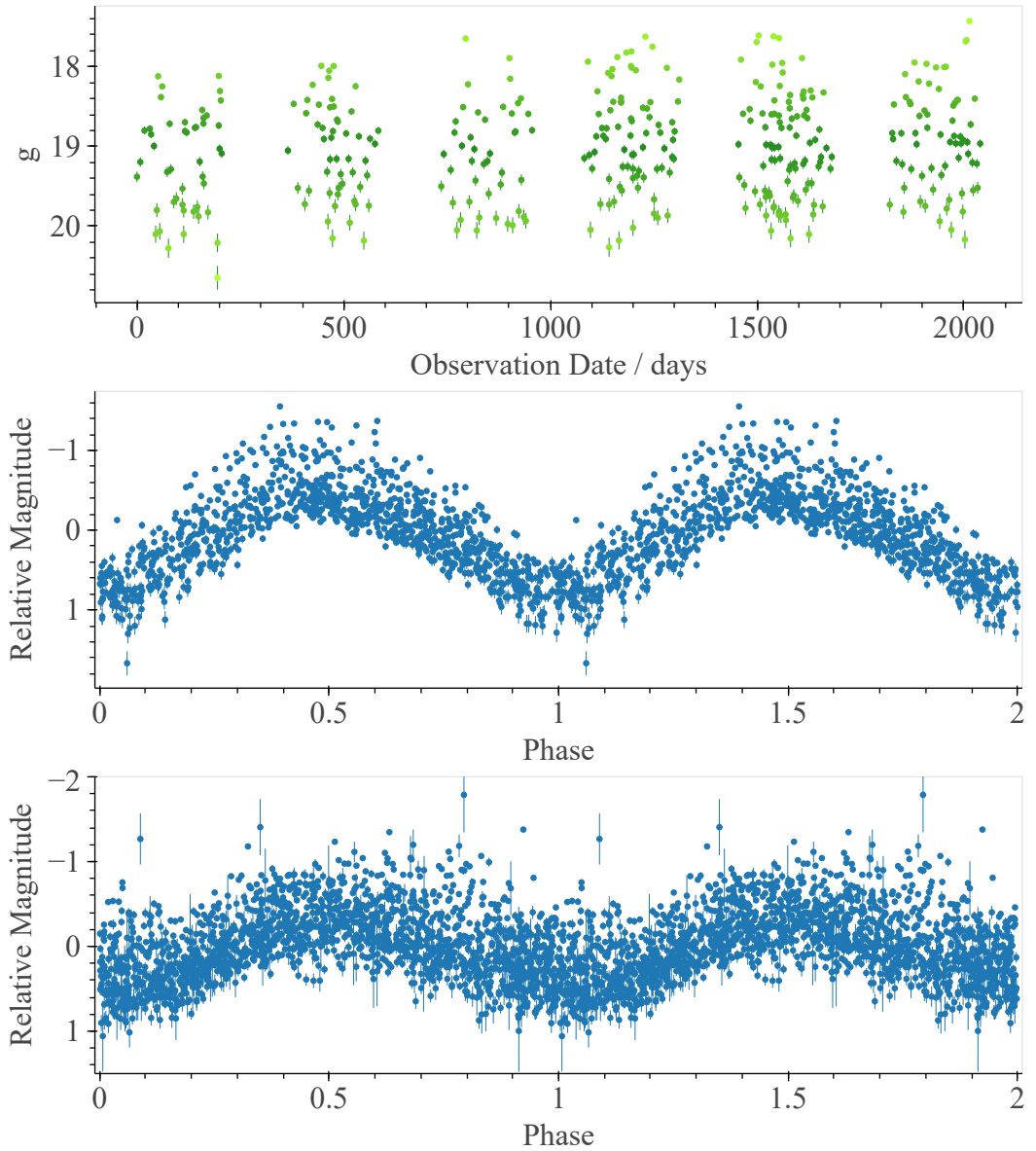


Figure 8.15: ZTF photometry of J201135.84–021340.49. Top panel:  $g$ -band light curve, showing its well-defined brightness variation of  $\simeq 2.5 - 3$  mag. Middle panel: phase-folded light curve (all bands scaled and merged), showing the system’s orbital modulation. The photometry is folded on a period of 4.16 h using the Lomb-Scargle periodogram. Bottom panel: Phase-folded ATLAS  $\alpha$ -band light curve of J191213.72–441045.08, the second white dwarf pulsar to be discovered. The photometry is folded on a period of 4.03 h using AOVMHW analysis.

interaction, this system may be in a similar state to the second white dwarf pulsar (J191213.72–441045.08)—whose phase-folded light curve is shown in the bottom panel of Fig. 8.15. The presence of flickering in this system’s modulation, which is

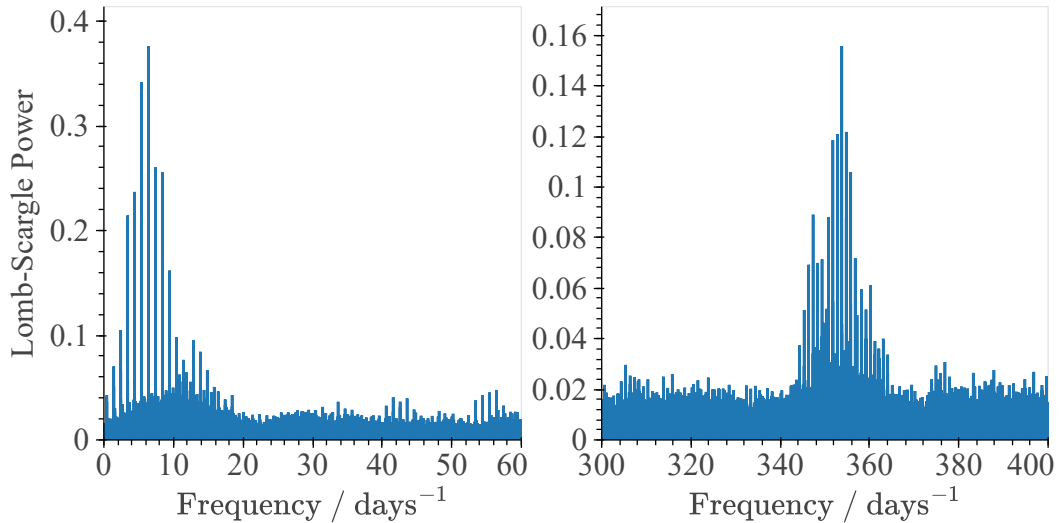


Figure 8.16: Lomb-Scargle power spectra derived from the ZTF photometry of J201135.84–021340.49. Left panel: Power spectrum calculated between the frequencies 0 – 60 d<sup>-1</sup>, suggesting an orbital period of 3.73 h. Right panel: Power spectrum calculated between frequencies of 300 – 400 days<sup>-1</sup>, showing a signal of the white dwarf’s spin at 4 min.

particularly evident near its maxima, suggests that it is interacting. If the system is in fact a white dwarf pulsar, this likely places it at a similar evolutionary stage to the second white dwarf pulsar. The phase-folded light curve of J191213.72–441045.08 is similarly noisy, and is shown in the bottom panel of Fig. 8.15. Much like AR Sco (see the top panel of Fig. 8.6), the power spectrum of this system contains a signal of the white dwarf’s spin—in this case at  $\simeq 4$  min (Fig. 8.16, right panel).

We are in the process of acquiring spectroscopy to confirm (or refute) this system as a fourth white dwarf pulsar.

### 8.2.5 J235354.93+415304.33

This system, GAIA DR3 616146181399718528, is a known polar which was re-identified in this work. This system has a one-pole geometry—i.e. accretion only occurs onto a single pole [Beuermann et al., 2021]. TNT photometry was retrieved for this system, which is shown in Fig. 8.17. The accreting pole is visible between  $\simeq 0.1$  and 1.2 h, and again between  $\simeq 1.8$  and 2.9 h. The lowest point in each dip occurs when the angle between the line of sight and the accretion funnel is at its minimum [Beuermann et al., 2021].

The clear double-humped morphology of this system’s light curves is a result of cyclotron beaming, where varying alignment of the white dwarf’s magnetic field

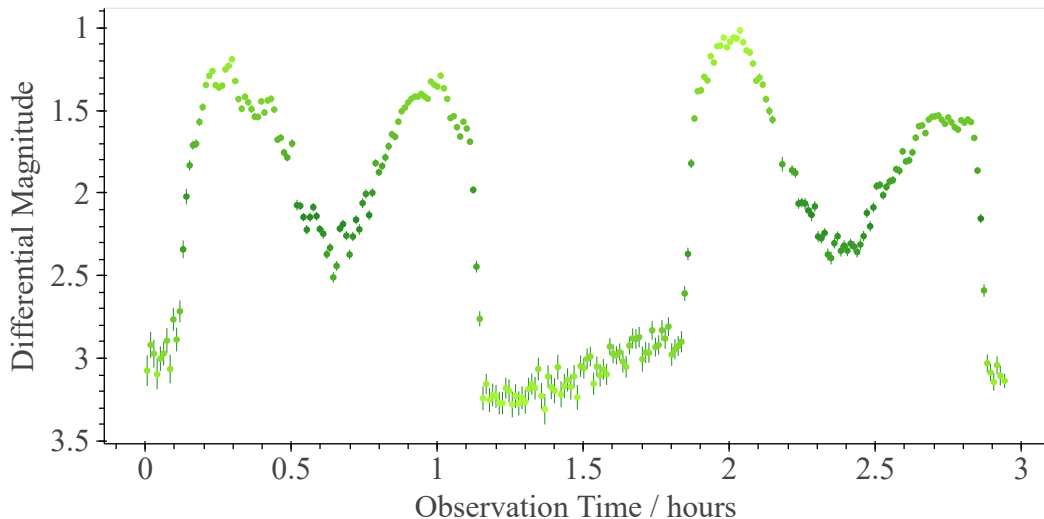


Figure 8.17: Top panel: TNT light curve of the polar J095308.20+145836.44, a system identified in this work. Data is binned into 260 equally spaced bins in time. The light curve of this system exhibits a clear double-humped morphology due to cyclotron beaming resulting from interactions with its strong magnetic field.

with the line of sight causes a distinct modulation in the received intensity of beamed radiation Bailey et al. [1984]; Gänsicke et al. [2001]. The observed modulation of systems in which cyclotron beaming is present is therefore a combination of orbital modulation and beaming-driven brightness variation, and this system is a great example.

### 8.2.6 J142438.93–022739.25

J142438.93–022739.25, GAIA DR3 3646410775989868800, is thought to be a polar. The ZTF  $g$  and  $r$ -band light curves and the ATLAS  $o$ -band light curves of this system are shown in the top and bottom panels of Fig. 8.18, respectively. The system shows sporadic variability of  $\simeq 1.5 - 3$  mag across these bands, with two well-defined brightness states being particularly visible in its ATLAS photometry. The system is identified as a polar with a quoted orbital period of 3.84 h in [Harrison and Campbell, 2015], although no such periodicity is derivable from the photometry featured in Fig. 8.18. The system has GALEX  $NUV$  and  $FUV$  detections, and an X-ray detection via XMM-Newton.

Further photometry was retrieved for this system through the TNT, which is shown in the top panel of Fig. 8.19. AOVMHW period analysis on this photometry reveals an orbital period of 4.06 h, longer by  $\simeq 13 - 20$  min than prior estimates in published literature. The system’s TNT photometry is phase-folded onto this

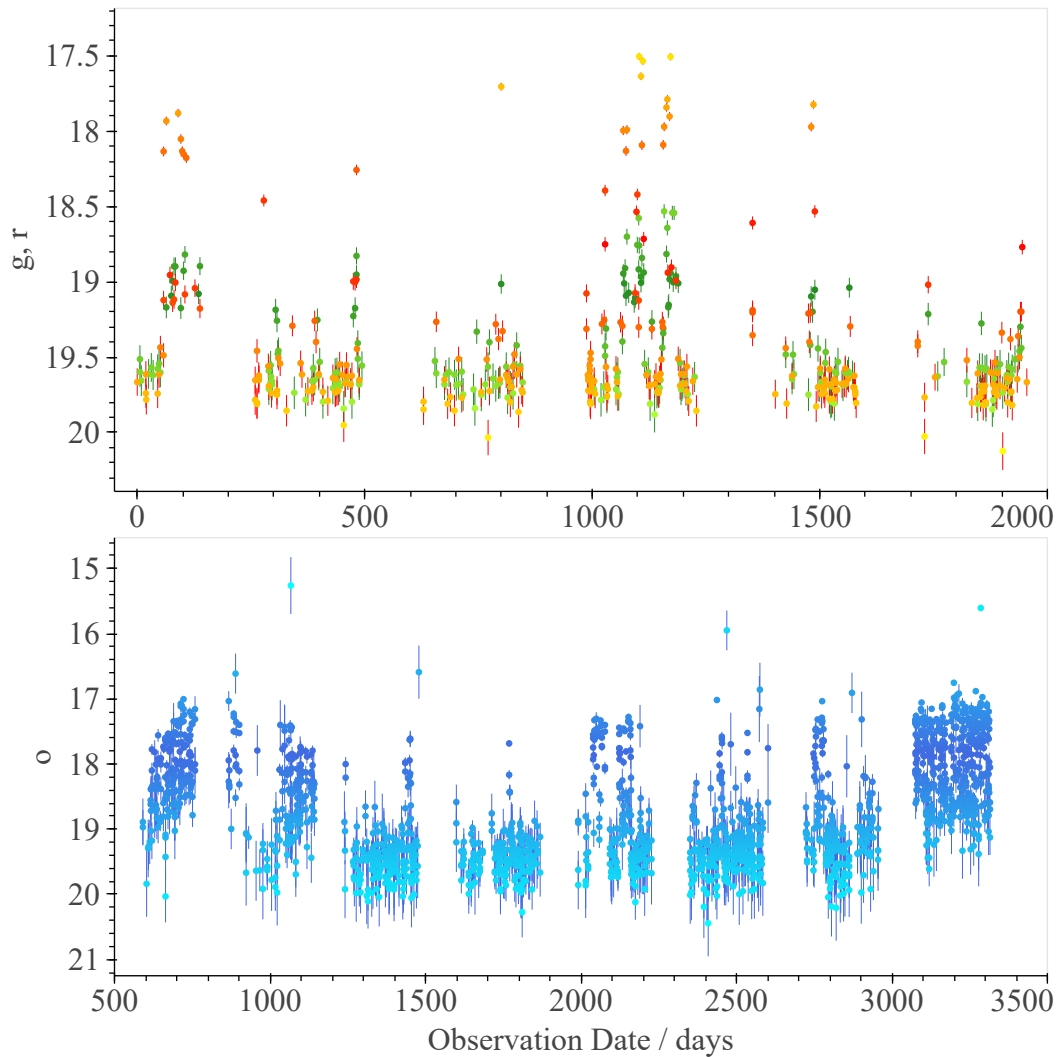


Figure 8.18: Light curves of J142438.93–022739.25. Top panel: ZTF  $g$  (green) and  $r$ -band (red) light curves of J142438.93–022739.25, showing its sporadic brightness variation of  $\simeq 1.5$  mag in  $g$ , and  $\simeq 2.5$  mag in  $r$ . Bottom panel: ATLAS  $o$ -band light curve, showing more clearly the well-defined brightness states of the system.

period in the bottom panel of Fig. 8.19. Similarly to what was seen in the known polar (J235354.93+415304.33) above, this reveals clear ‘dipping’ in the system’s modulation at each maximum (as indicated by yellow regions). This is interpreted as being a result of a combination of cyclotron beaming and eclipsing of the accretion zone from which much of the system’s luminosity originates [Dillon et al., 2008]. Given that beaming-induced modulation is typically more noisy than its orbital counterpart, the former appears to be the primary driver of modulation in this system. As was observed in J045254.56+301718.00, this system exhibits distinct

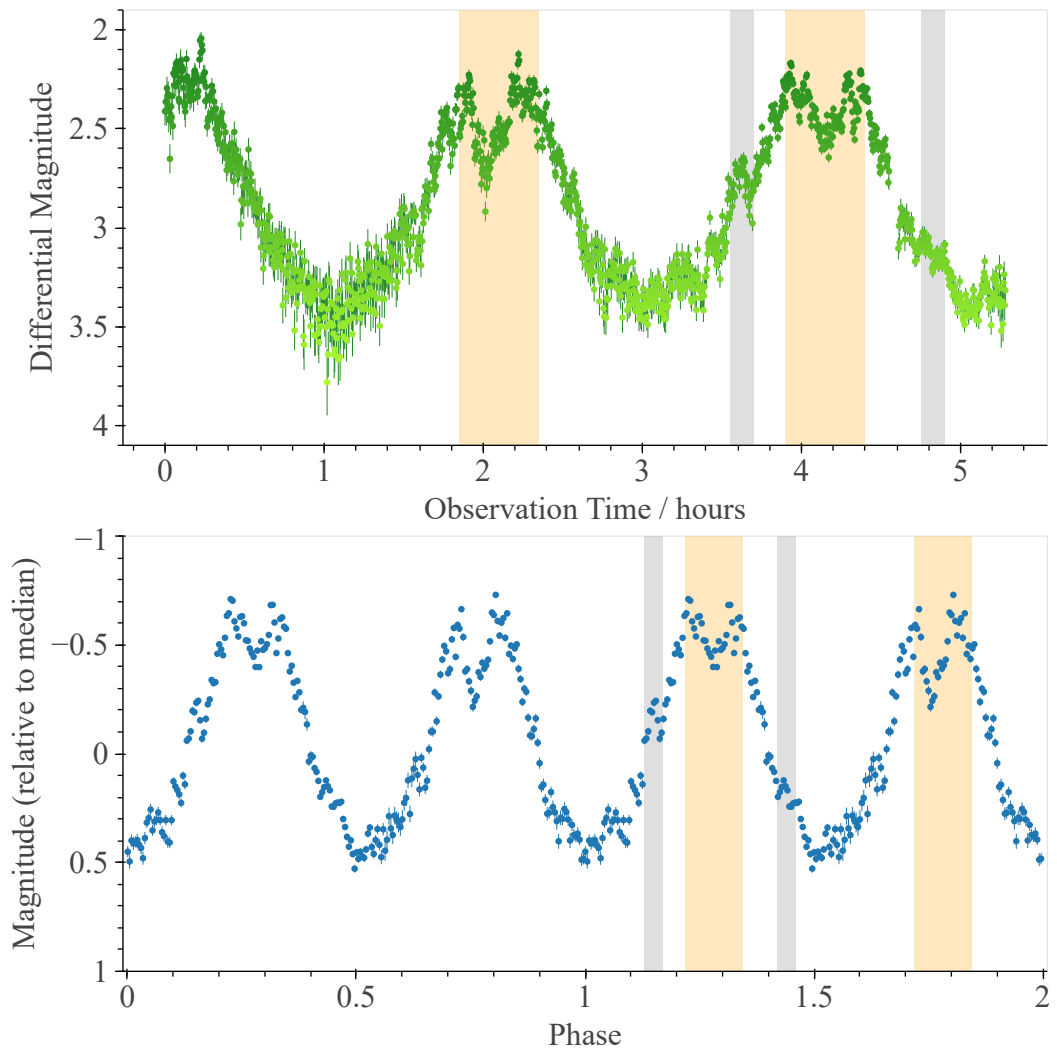


Figure 8.19: Top panel: TNT light curve of J142438.93–022739.25. Bottom panel: phase-folded TNT light curve, folded on a period of 4.06 h. Data is binned into 240 equally spaced bins in time. Grey regions highlight distinct steps in the system’s rise and fall in brightness, and orange regions highlight dips in brightness which are thought to be a result of absorption or eclipsing of the accretion zone.

steps in its modulation—indicated by the grey regions in Fig. 8.18. In this system, however, it is far less clear whether this is a result of eclipses. The cause of this is therefore not fully understood.

### 8.3 Summary

A search was carried out for AR Sco-like systems using the three known white dwarf pulsars as reference. Through these, various filtering criteria were derived and utilised to obtain a list of candidates from Gaia’s third data release. These candidates were further reduced using ZTF photometry, the analysis of which resulted in a final set of 58 candidates. Further investigation of these candidates resulted in the identification of a promising white dwarf pulsar candidate (J201135.84–021340.49), a previously unidentified CV, a millisecond pulsar candidate which was determined to be an intriguing YSO, a polar and a pre-polar. Furthermore, seven known polars and five known SU UMa dwarf novae were reidentified. The remaining 36 systems have not yet been fully explored, but available archival data along with additional high-speed photometry from the TNT (see Appendix C) suggests that a number of them are CVs of some form. The high success rate in identifying interacting white dwarf binaries demonstrates the success of the approach explored here, and we are in the process of acquiring spectroscopy to confirm (or refute) J201135.84–021340.49 as a fourth white dwarf pulsar.

## Chapter 9

# The Search for X-ray Binaries

### 9.1 Methodology

#### 9.1.1 Obtaining a Set of Candidates

Given the similarity of their goals, the general steps taken in both searches closely match. However, the number of potential reference systems here (i.e. the number of known black hole X-ray binaries, henceforth BHXBs) is significantly larger. The first task in this search was therefore to acquire a refined set of reference systems, starting with the 72 known or dynamically-confirmed black hole binaries listed in the BlackCAT catalogue.

Much like the search for white dwarf pulsars, the third data release of Gaia formed the backbone of this work. The first step towards acquiring a refined set of reference systems was therefore to find those with a matching Gaia detection. Of the 72 BlackCAT BHXBs, 17 had Gaia detections listed in SIMBAD. As discussed previously, images are a key tool in matching positional data to its host system, and so Pan-STARRS (if available, otherwise SkyMapper) images were generated at the BlackCAT coordinates of the remaining systems via ATK, with a size of 20 arcsec. These included a Gaia detection overlay which is corrected for proper motion. Combined with Gaia’s positional accuracy of less than one milliarcsecond for sources of the brightness encountered here [European Space Agency, 2025], this made the matching of positional data possible even in crowded regions. The result of this analysis was the retrieval of seven further Gaia detections, for a total of 24. A further complication which results from the crowded regions in which many BHXBs are found is the need to account for extinction, which is especially relevant here due to the dimness of the systems on which the search is focused—XRBs in quiescence. This particularly affects shorter wavelengths, resulting in the ‘reddening’ of light

	<b>J1820+0711</b>	<b>J1654–3950</b>	<b>J0622–0020</b>	<b>J1547–4740</b>
Name	-	V1033 Sco	V616 Mon	IL Lup
ra	275.0914	253.5006	95.6856	236.7844
dec	7.1853	–39.8458	–0.3457	–47.6695
$b$	10.1592	2.4560	6.5397	5.4263
$R_{p,s}$	0.370	0.711	0.343	0.680
$G_{\text{abs}}$	20.223	18.540	21.688	17.871
$G_{\text{BP}} - G_{\text{RP}}$	0.848	2.159	1.678	0.884
$V_G$	7.442	1.8579	1.567	0.379
$\pi$	0.369	0.290	0.697	0.191
$\alpha_\pi$	4.733	6.033	5.967	3.465
$\mu$	7.006	8.626	5.157	9.251
$\alpha_\mu$	75.237	168.917	53.717	182.545
RUWE	1.015	1.055	1.099	1.089
AEN	0.0	0.0	0.368	0.128

Table 9.1: Key Gaia parameters of the four reference black hole X-ray binary systems. ra is the right ascension in degrees, dec is the declination in degrees,  $b$  is the system’s J2000 latitude in galactic coordinates (degrees),  $R_{p,s}$  is the projected reddening in magnitudes (as described in the text),  $G_{\text{abs}}$  is the absolute Gaia  $G$  magnitude,  $G_{\text{BP}}$  and  $G_{\text{RP}}$  are the apparent  $BP$  and  $RP$  Gaia magnitudes, respectively,  $V_G$  is the Gaia variability parameter,  $\pi$  is the parallax in mas (milli-arcsec),  $\alpha_\pi$  is the parallax significance,  $\mu$  is the total proper motion in  $\text{mas yr}^{-1}$ ,  $\alpha_\mu$  is the proper motion significance, RUWE is the renormalised unit weight error and AEN is the astrometric excess noise. These were all used to define cuts in Gaia’s third data release. The full J2000 coordinates of these systems are J182021.94+071107.28, J165400.14–395044.76, J062244.54–002044.29 and J154708.28–474010.28, respectively.

from X-ray binaries as it is absorbed, reflected or scattered through interstellar dust. This was achieved through the use of STILISM (see Section 7.2.1.2).

In cases where the system is located beyond the extent of the map provided by STILISM, the estimated reddening is an underestimate. Likewise, the estimated reddening of a system within the extent of the extinction map is likely to be an overestimate. While STILISM provides lower limits to account for the latter, its upper limits do not extend beyond that of its extinction map. ‘Projected’ reddening values were therefore calculated for each system as:

$$R_{p,s} = \frac{D}{D_s} R_s,$$

where  $D_s$  is the maximal extent of STILISM’s extinction map along a given line of sight,  $R_s$  is the reddening along that line of sight, and  $D$  is the distance to the

system.

If a system lies beyond STILISM’s extinction map,  $R_{p,s} \gtrsim R_s$ , and hence  $R_{p,s}$  provides a more harsh estimation of the extent to which its photometry may be affected by reddening. Likewise, if it is located far closer than the extent of the extinction map,  $R_{p,s} \lesssim R_s$ . By definition, the utility of  $R_{p,s}$  in estimating the reddening of a system depends heavily on the quality of its astrometry. Nine of the 24 known BHXBs with Gaia detections either had a negative parallax or did not have a parallax measurement at all. These systems were discarded.

The specific criteria used in the next stages of filtering were primarily guided by the desired number of reference systems, which is an important balance between the quality of astrometry/photometry among the reference sample and the degree to which it represents the BHXB population as a whole. For consistency with the search for white dwarf pulsars, the target was to obtain a reference sample of  $\simeq 3-5$  systems. In order to achieve this, the remaining 15 known BHXBs were filtered by parallax significance ( $\alpha_\pi$ , see Eq. 8.1), specifically:

$$\alpha_\pi > 3.$$

Six systems met this criterion and were consequently filtered by their projected reddening,  $R_{p,s}$ :

$$R_{p,s} < 1.$$

Through the steps outlined above, the initial set of 72 expected or dynamically confirmed black hole binaries were refined to a set of four reference systems—all of which contain a dynamically confirmed black hole. The relevant parameters of these systems are shown in Table 9.1.

Similarly to the search for white dwarf pulsars, the next stage was to use these reference systems to derive a set of black hole X-ray binary candidates with similar observable properties. While both searches started with Gaia’s third data release, additional steps were introduced here. The first of these was a crossmatch of Gaia DR3 with the first data release of eROSITA-DE, which was performed through STILTS (see Section 7.3). The mean  $1\sigma$  positional uncertainty in the first data release of eROSITA-DE was found to be 4.54 arcsec, a result which is consistent with what would be expected from the early data release (4.7 arcsec, see Salvato, M. et al. [2022]). Gaia’s positional uncertainty is negligible in comparison [European Space Agency, 2025], and hence eROSITA-DE was the primary influence when choosing the radius of the crossmatch. To minimise the loss of systems from the resulting

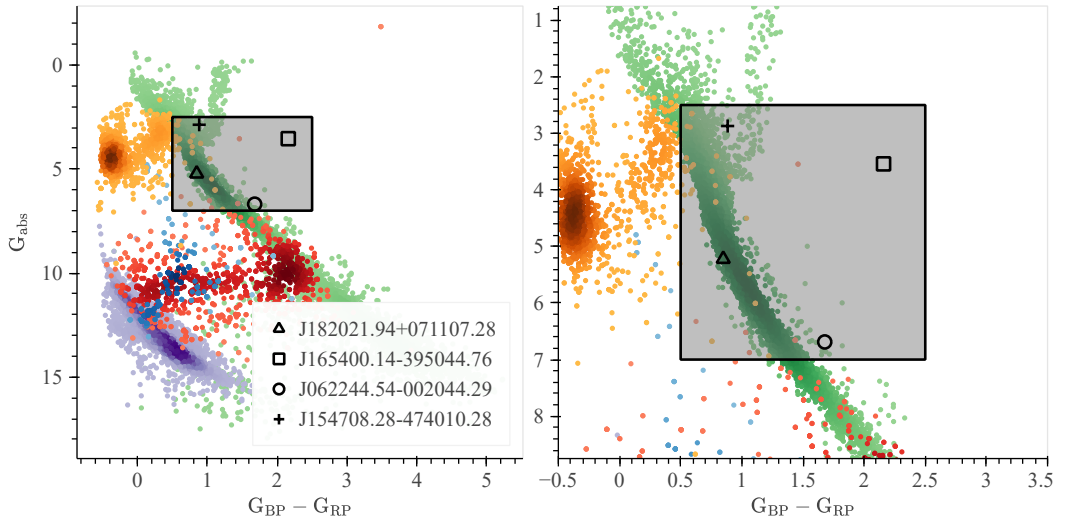


Figure 9.1: Left panel: Gaia Hertzsprung-Russell diagram showing the locations of the four reference systems that were used in the search for X-ray binaries. A box is overlaid showing the selected region as described in the text. Right panel: the same figure as in the left panel, zoomed in on the selected region. The background (colour) sample is a 100 pc Gaia sample split into various sub-groups. Green: clean sample of stars, yellow: clean sample of spectroscopically confirmed subdwarfs, blue: clean sample of spectroscopically confirmed cataclysmic variables, red: clean sample of spectroscopically confirmed white dwarf + M-dwarf binaries, purple: clean sample of white dwarfs. Background sample provided by B. Gänsicke.

data set, a matching radius of 5 arcsec was used.

The cross-matched sample was then filtered by Galactic latitude,  $b$ , to remove any systems located too close to the Galactic plane. Any systems which did not meet the following criterion were, therefore, removed:

$$|b| > 5.$$

Although this results in the exclusion of one of the reference systems, J165400.14–395044.76 (see Table 9.1), it is necessary here to limit the effects of crowding—particularly the contamination of photometry from nearby bright objects. The coverage of eROSITA-DE in Galactic longitude ( $180 < l < 360$  deg) already excludes the Galactic centre. The remaining filtering criteria were derived in the same way as those used in the search for white dwarf pulsars, with cutoff values chosen both in line with those of the reference systems (see Table 9.1), and by visual inspection in the case of the HRD selection (see Fig. 9.1). The following criteria were used:

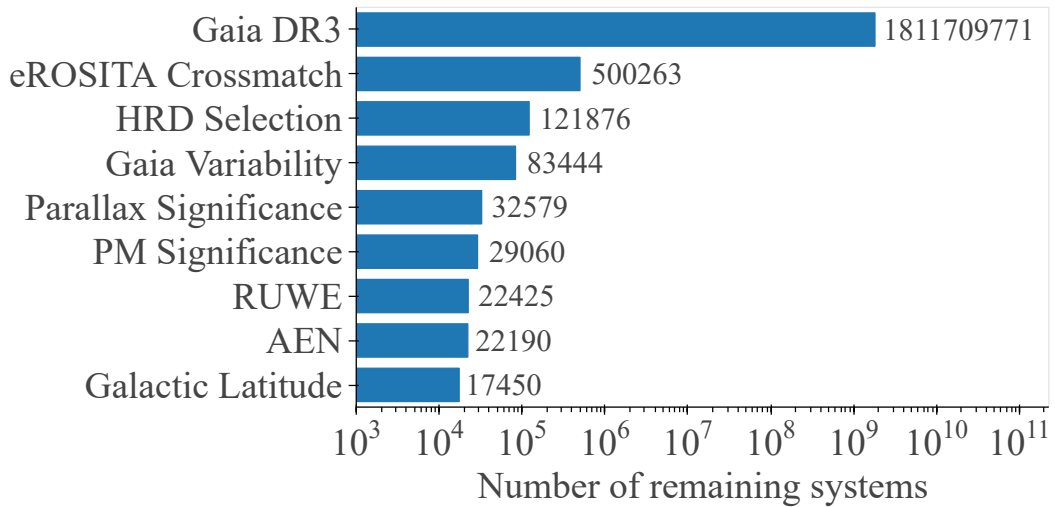


Figure 9.2: The number of remaining systems in the X-ray binary search after each stage of filtering.

$$\begin{aligned}
2.5 < G_{\text{abs}} < 7 \\
0.5 < G_{\text{BP}} - G_{\text{RP}} < 2.5 \\
V_G > 0.35 \\
\alpha_\pi > 3 \\
\alpha_\mu > 50 \\
\text{RUWE} < 1.4 \\
\text{AEN} < 0.5
\end{aligned}$$

with all parameters defined previously and in Tables 8.1 and 9.1. The number of remaining systems following each stage of filtering is shown in Fig. 9.2. The corresponding percentage decreases resulting from each stage are shown in Fig. 9.3. The final result of this filtering was a set of 17 450 systems—an order of magnitude larger than the number of systems at the equivalent stage in the search for white dwarf pulsars. Comparing Figs. 8.4 and 9.3, this is primarily due to the less harsh constraint placed on the Gaia variability parameter,  $V_G$ . Further supporting this conclusion is the reduced effect of the  $\alpha_\pi$  and  $\alpha_\mu$  criteria—despite using harsher cutoff values. This can be understood by once again considering the definition of  $V_G$ . A harsher constraint on  $V_G$  (i.e. the use of a higher cutoff value) results in systems typically having less well-defined photometry and astrometry. The effect

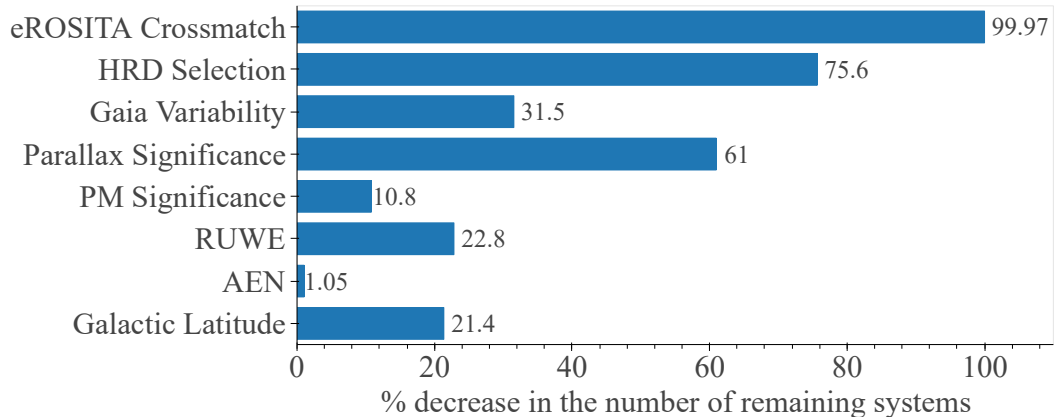


Figure 9.3: The decrease in the number of remaining systems caused by each criterion in the search for black hole binaries, given as a percentage of the systems in the previous stage.

of filtering by  $\alpha_\pi$  and  $\alpha_\mu$  is therefore expected to be proportional to the harshness of the constraint in  $V_G$ , and vice versa—as observed here. As may be expected, this also seems to be true for AEN. This is a particularly useful comparison, as the constraints on AEN were the same in both searches.

### 9.1.2 Obtaining and Analysing Light Curves

The next step was to obtain photometry for each of the candidate systems. The time constraints of an MSc meant that there was not sufficient time to analyse the full set of 17 450 candidates, and so a subset of 3 000 systems were selected based on their mean brightness across the three Gaia filters:

$$m_{\text{Gaia, total}} = \frac{G + G_{\text{BP}} + G_{\text{RP}}}{3},$$

where  $G$ ,  $G_{\text{BP}}$  and  $G_{\text{RP}}$  are the Gaia  $G$ ,  $BP$  and  $RP$  magnitudes, respectively. The primary benefit of sorting the candidates by brightness is a further assurance of high-quality astrometry and photometry among those that were subjected to further investigation (see Fig. 9.4).

To maximise the number of systems for which photometry would be available, an all-sky survey was used: ATLAS. It is important to note that the enhanced coverage of ATLAS does come at the cost of sensitivity, with a  $5\sigma$  magnitude limit of around 19.7—almost a magnitude lower than ZTF’s limit of 20.5 [Tonry et al., 2018; Bellm and Kulkarni, 2017]. However, the sorting of the candidates by brightness in the previous step renders this problem insignificant. This is reflected in the fact

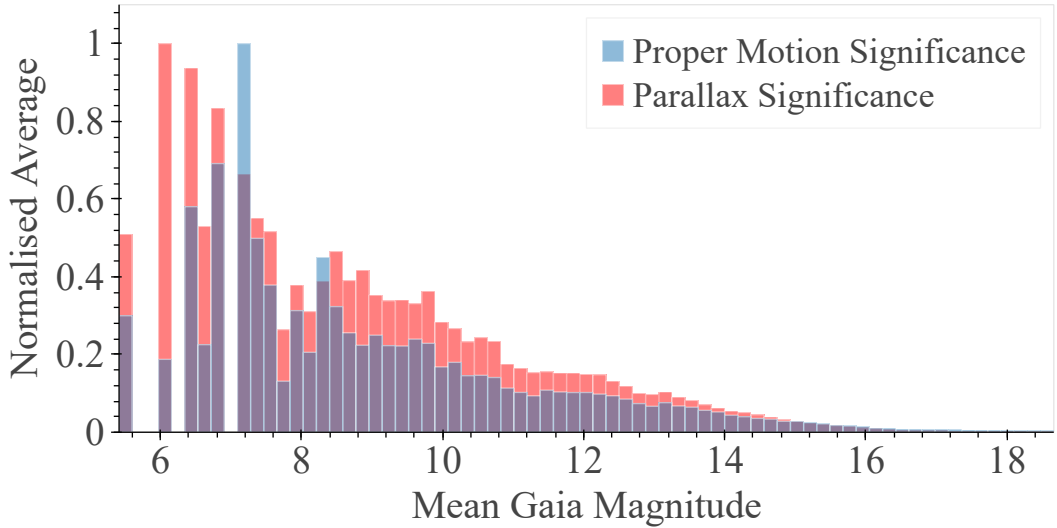


Figure 9.4: Distribution of proper motion and parallax significance (i.e. the ratio of their values to their errors) among the final set of X-ray binary candidates. Average values were taken across 100 bins in mean apparent Gaia magnitude ( $G$ ,  $G_{BP}$  and  $G_{RP}$  bands), and have been normalized.

that of these 3 000 ATLAS queries, all were successful.

It is important to note that ATLAS provides both ‘difference’ and ‘reduced’ light curves, with the latter being used here. Furthermore, ATLAS photometry is prone to poorly defined observations. To counteract this, filtering can be enabled in ATK which removes observations that do not meet the following criteria:

$$\begin{aligned}
 |f| &> 3 \\
 \sigma_f &< 4000 \\
 0 &< \sigma_m < 0.5 \\
 m &> 0.
 \end{aligned}$$

where  $f$  and  $\sigma_f$  are the flux and its error in microJanskys.  $m$  and  $\sigma_m$ , derived from these fluxes, are the apparent magnitude and its error, respectively. The first criterion removes observations for which the measured flux is below signal-to-noise, and the following two criteria remove those with erroneously large uncertainties. The final criterion removes observations which report a negative flux and hence a negative magnitude, which arise from ATLAS overestimating the brightness of the sky in its reduced light curves under certain circumstances. A full explanation can be found in ATLAS [2024].

The ATLAS photometry obtained for each system was used in the genera-

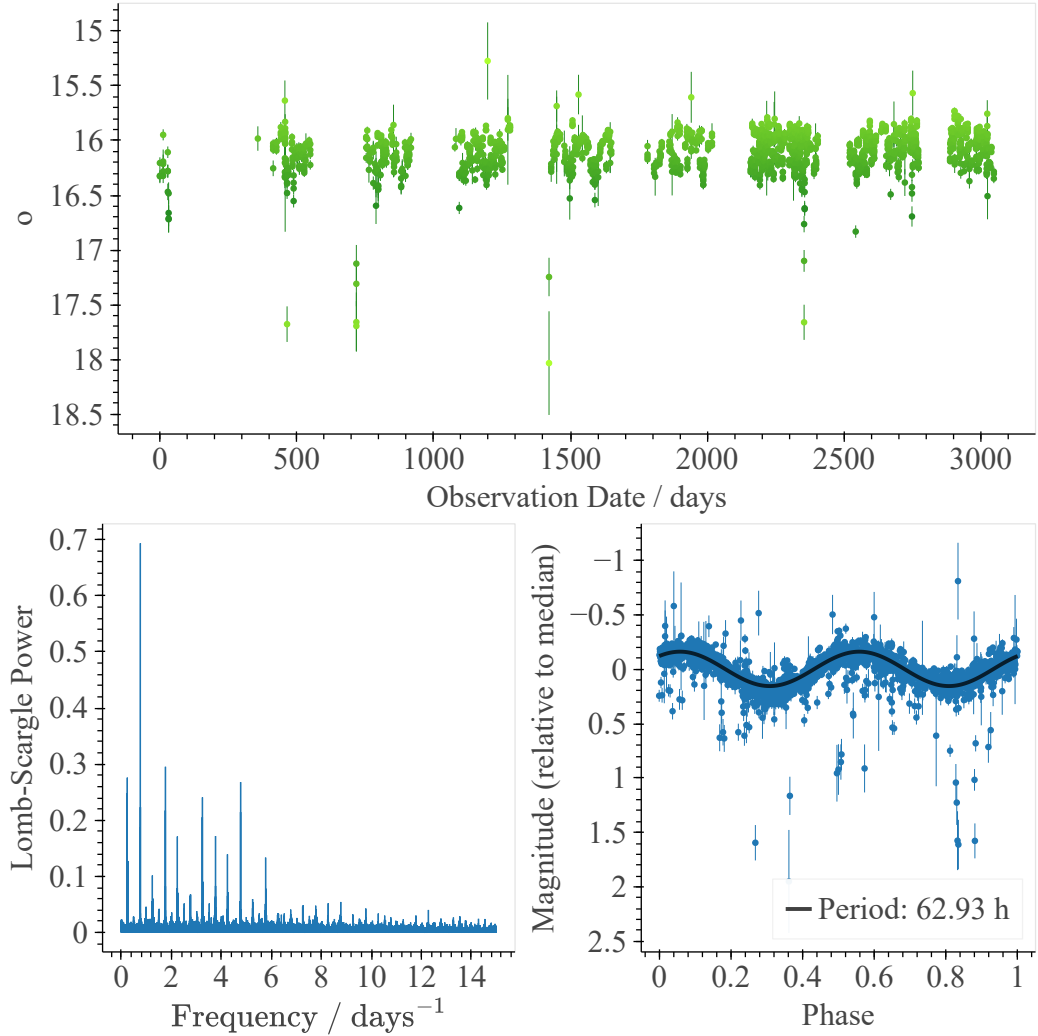


Figure 9.5: Top panel: ATLAS  $o$ -band light curve of J165400.14–395044.76, a dynamically confirmed black hole X-ray binary [Corral-Santana, 2024]. Bottom-left panel: Lomb-Scargle power spectrum of ATLAS photometry (all bands scaled and merged), suggesting an orbital period of 31.46 h. Bottom-right panel: Phase-folded ZTF light curve (all bands scaled and merged), folded on a period of 62.93 h. A sine wave of the same period is overlaid. Despite the period suggested by the system’s power spectrum, this is a harmonic of the true period of 62.93 h [Petretti et al., 2023].

tion of Lomb-Scargle power spectra, which were analysed to remove any systems which did not show clear periodicity. The power spectrum of a known black hole binary, J165400.14–395044.76, which is also one of the reference systems used in this search, is shown in Fig. 9.5. Throughout this analysis, any probable but unclear

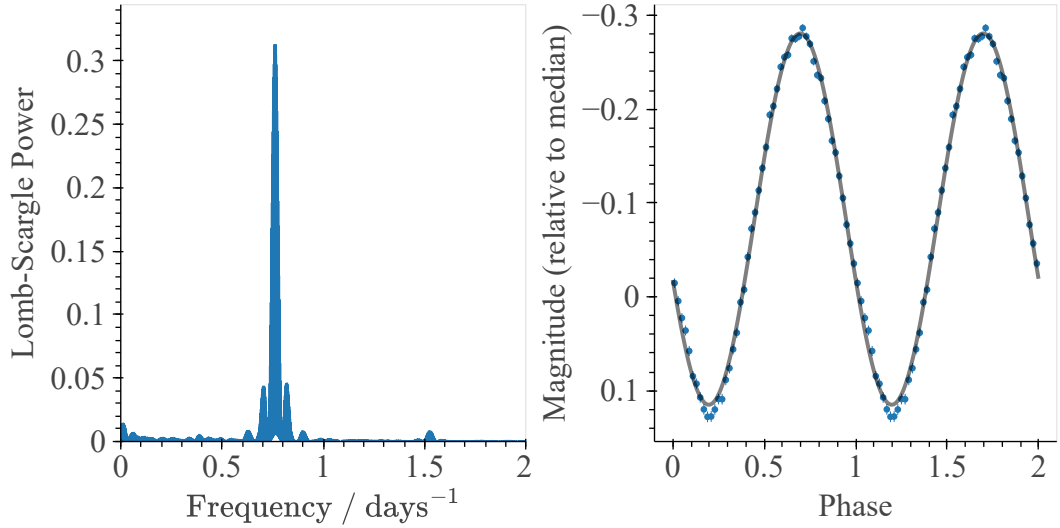


Figure 9.6: Left panel: Lomb-Scargle power spectrum of TESS photometry of J165400.14–395044.76, a dynamically confirmed black hole X-ray binary [Corral-Santana, 2024]. A well-defined spike suggests a period of 31.46 h. Right panel: phase-folded TESS photometry, split into 50 equally spaced bins in time. A sine wave is overlaid with a frequency equal to the true period of the system, 62.93 h—a harmonic of the period suggested by its power spectrum.

periodicities were validated using TESS photometry. While TESS observes systems over a much shorter interval, the typical cadence of these observations is only 2–30 min [Ricker et al., 2015]—multiple orders of magnitude faster than ATLAS’ cadence of two days [Tonry et al., 2018]). Along with its sky coverage of  $\simeq 85\%$  [Nasa, 2024], this made TESS a key component in the accurate determination of candidate orbital periods. Figure 9.6 shows the Lomb-Scargle power spectrum and phase-folded light curve derived from TESS data for the same reference black hole X-ray binary as in Fig. 9.5. The final set of candidates returned by this search is therefore comprised of the 322 systems which showed clear periodicity in their ATLAS and/or TESS photometry.

### 9.1.3 Estimating Spectral Types

Typical spectral types of the final set of candidate systems were estimated through their positions in the Gaia HRD, using a set of stars of known spectral type for calibration. These are shown in the left panel of Fig. 9.7. The regions of each spectral type in the Gaia HRD were therefore defined as:

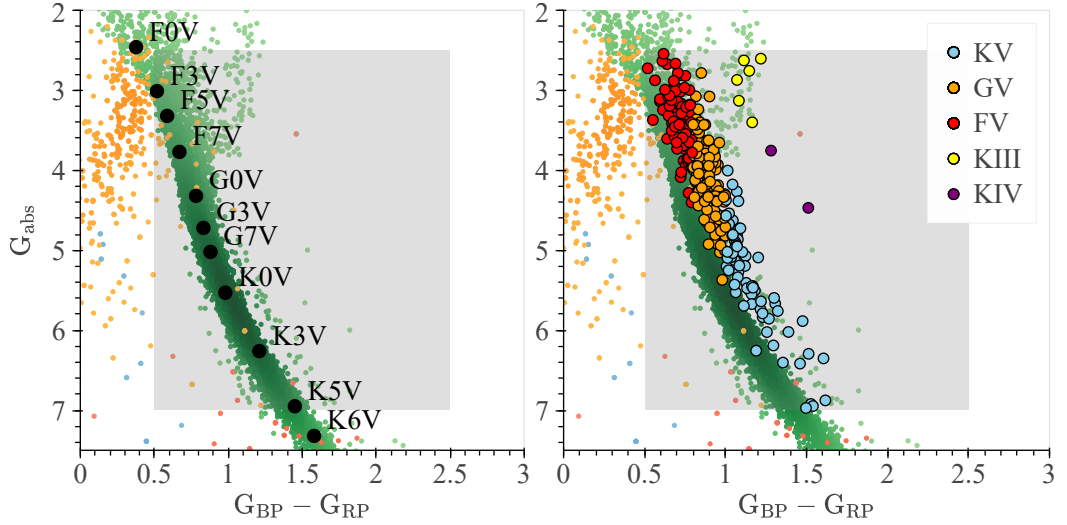


Figure 9.7: Left panel: Stars used in the calibration of typical spectral types across the Gaia HRD, taken from Table 5 in Pecaut and Mamajek [2013]. Right panel: Positions of the X-ray binary candidates identified in this work in the Gaia HRD, coloured by their typical spectral type (estimated as described in the text and the left panel of this figure). Systems marked ‘V’, ‘IV’ and ‘III’ are main sequence stars, subgiants and giants, respectively. Grey regions indicate the cut made to the HRD in this search, as described in the text. The background (colour) sample is a 100 pc Gaia sample split into various sub-groups. Green: clean sample of stars, blue: clean sample of spectroscopically confirmed CVs, red: clean sample of spectroscopically confirmed white dwarf + M-dwarf binaries, purple: clean sample of white dwarfs. Background samples provided by B. Gänsicke.

$$\text{F} : 0.4 < G_{\text{BP}} - G_{\text{RP}} \leq 0.8$$

$$\text{G} : 0.8 < G_{\text{BP}} - G_{\text{RP}} \leq 1.0$$

$$\text{K} : 1.0 < G_{\text{BP}} - G_{\text{RP}} \leq 1.85,$$

where  $G_{\text{BP}}$  and  $G_{\text{RP}}$  are the Gaia *BP* and *RP* magnitudes, respectively. The definition of a star’s spectral type as a measure of its temperature means that colour—an analogue to temperature—is typically used in its estimation. Ten subdivisions in the F – K spectral types were therefore determined via linear interpolation in the  $G_{\text{BP}} - G_{\text{RP}}$  colour.

Classifications or suggested classifications for each of these systems were then taken from any published literature. No SDSS spectra were available to aid in the classification of these candidates—likely due to them being too bright [SDSS, 2021].

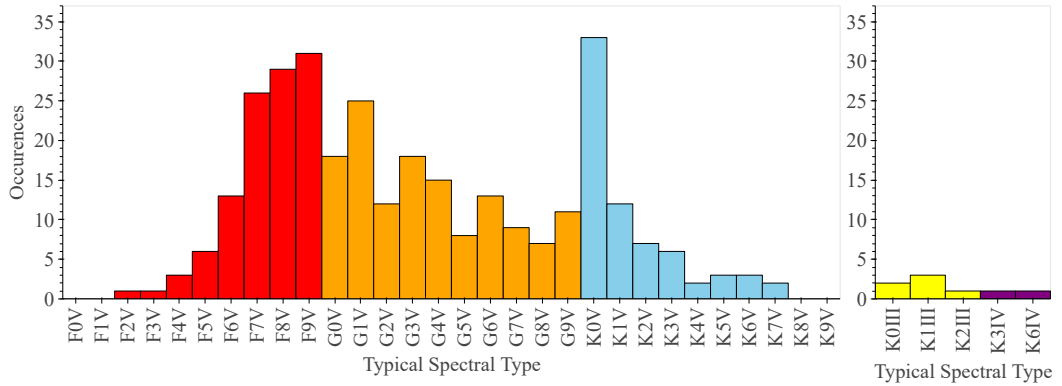


Figure 9.8: Distribution of typical spectral types among the final set of X-ray binary candidates identified in this work. Systems marked ‘V’, ‘IV’ and ‘III’ are main sequence stars, subgiants and giants, respectively.

## 9.2 Results

As noted previously, the time constraints of an MSc necessitated that the analysis of these candidates was more explorative than what was achieved in the search for white dwarf pulsars. It is also important to note that all four reference systems that were used in this search were lost in the final set of candidates, due to none of them being detected by eROSITA. One of these, J1820+0711, was lost due to it being located outside of eROSITA-DE’s coverage. The reason for the lack of detection of the remaining three is not clear but may be due to their weak X-ray luminosity in quiescence. It is worth noting, however, that two of the 72 BlackCAT X-ray binaries do have eROSITA detections—indicating that the X-ray emission from these systems *can* exceed eROSITA’s detection limit. If the lack of eROSITA detections is ignored, two of the four reference systems would have been retained in the final set of candidates. One reference system, J1654–3950, would have been lost due to the removal of systems along the galactic plane, and the other, J1820+0711, would have been lost as a result of it showing no clear periodicity in its ATLAS photometry (no TESS photometry is available).

### 9.2.1 Spectral Type Distribution

The HRD positions and broad spectral types of the candidate systems are shown in the right panel of Fig. 9.7, and the distribution of candidates among each spectral type, including subdivisions, is shown in Fig. 9.8. Despite the selected region of the HRD including a significant portion of the M-type region, no M-type systems were returned. This is a result of sorting the original 17 450 systems by brightness.

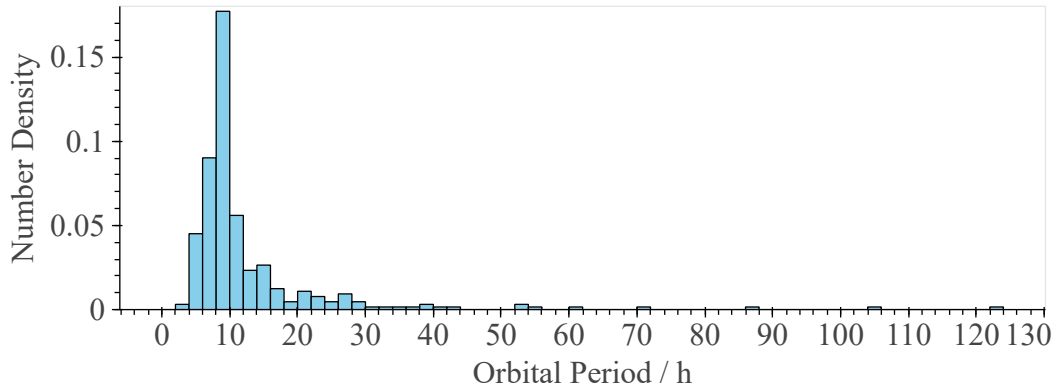


Figure 9.9: Distribution of orbital periods among the final set of X-ray binary candidates identified in this work.

The colour (in this case  $G_{\text{BP}} - G_{\text{RP}}$ ) of a system is inversely proportional to its temperature and hence its brightness, and so the loss of any systems with a spectral type beyond  $\simeq$  K7V is a side effect of the inexhaustive nature of this search. The most abundant spectral type is G, with 136 G-type systems compared to 110 and 76 F and K-type systems, respectively. However it is important to note that this is not representative, as the abundances of F and K-type systems are underestimates: the selected region of the HRD removes any systems hotter than  $\simeq$  F3V, and the sorting of systems by brightness earlier in the search restricts K-type systems to being  $\simeq$  K5V or hotter.

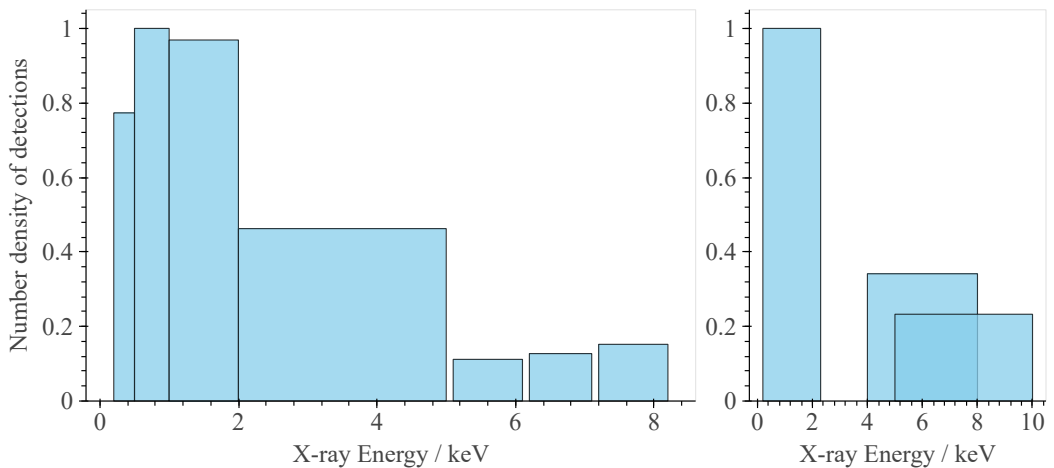


Figure 9.10: Number of X-ray binary candidates detected in each X-ray energy band of eROSITA. Left panel: narrow bands. Right panel: broad bands.

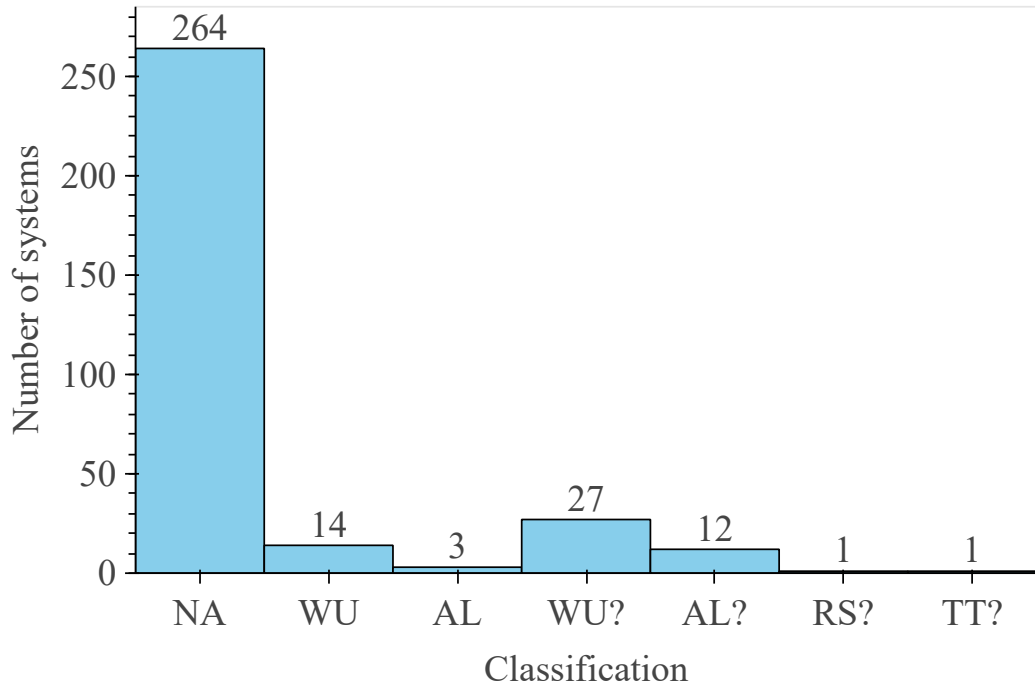


Figure 9.11: Classifications of the X-ray binary candidates identified in this work. NA = no suggested classification, WU = WUMa contact binary, AL = Algol variable, TT = T Tauri variable, RS = RS CVn variable. Those denoted with a ‘?’ are unconfirmed classifications, i.e. are only mentioned as candidates in large catalogues.

### 9.2.2 Orbital Period and X-ray Flux Distributions

The distribution of orbital periods amongst the final set of candidates is shown in Fig. 9.9, and peaks significantly in the range of 8 – 10 h. This is likely a result of a large number of close/contact binaries among the returned candidates—a problem that will be discussed fully later. These orbital periods were obtained through the visual analysis of phase-folded TESS and ATLAS light curves, using orbital frequencies derived from the Lomb-Scargle periodogram (as described above).

The distribution of detections in each of eROSITA’s X-ray energy bands is shown in Fig. 9.10.

### 9.2.3 Exploring the Candidates

The classifications or suggested classifications among the candidate systems are shown in Fig. 9.11. The category ‘NA’ in this figure is comprised of any systems that had no suggested classification in the literature or were only referenced in large

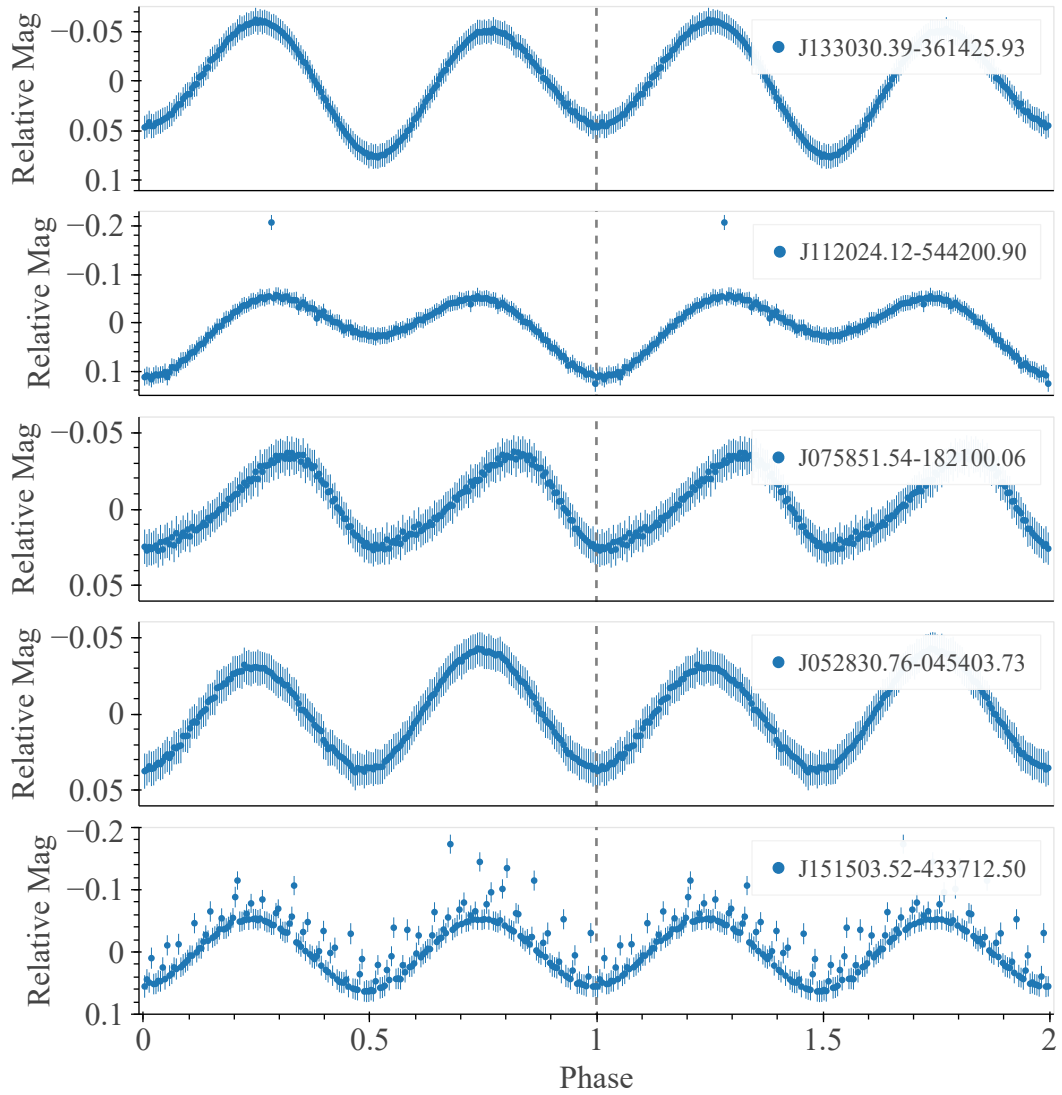


Figure 9.12: TESS photometry of five black hole binary candidates identified in this work, folded on a period calculated using the Lomb-Scargle periodogram. From the top panel to the bottom panel, the orbital periods of these systems are 8.43 h, 8.65 h, 41.96 h, 8.52 h and 8.07 h. Each system is described in the text.

surveys as some form of eclipsing/contact binary (i.e. the specific configuration was not mentioned). A selection of these candidates, all of which have no literary classification, will now be discussed. Fig. 9.12 shows the phase-folded TESS photometry of five black hole binary candidates.

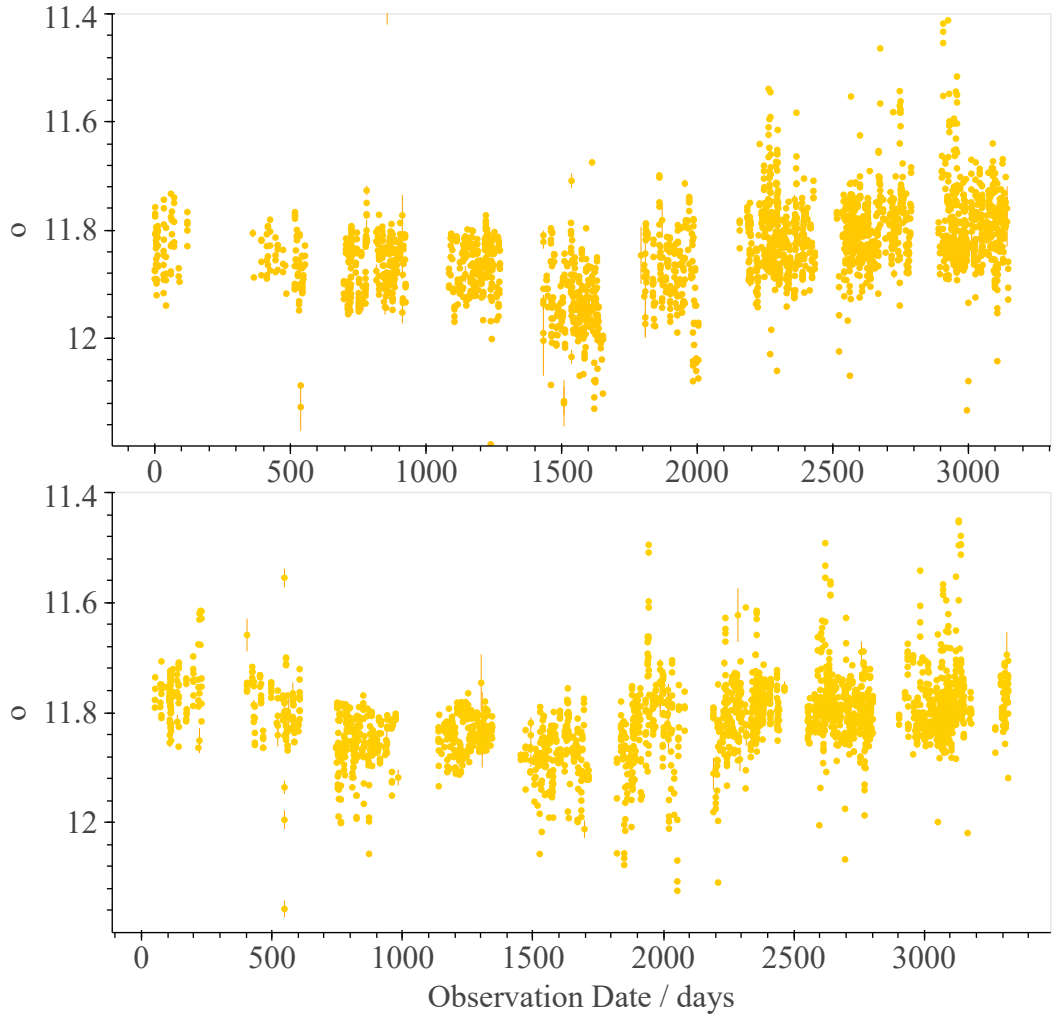


Figure 9.13: ATLAS  $o$ -band photometry of two black hole binary candidates identified in this work, both of which exhibit long-term variability. Top panel: photometry obtained for J133030.39–361425.93. Bottom panel: photometry obtained for J052830.76–045403.73.

### 9.2.3.1 J133030.39-361425.93

The first candidate, GAIA DR3 6163143967998002560, exhibits well-defined ellipsoidal modulation on a period of 8.43 h. The system is included here due to the long-term variability of its ATLAS light curve, which is shown in Fig.9.13. The typical spectral type of this system is G0V.

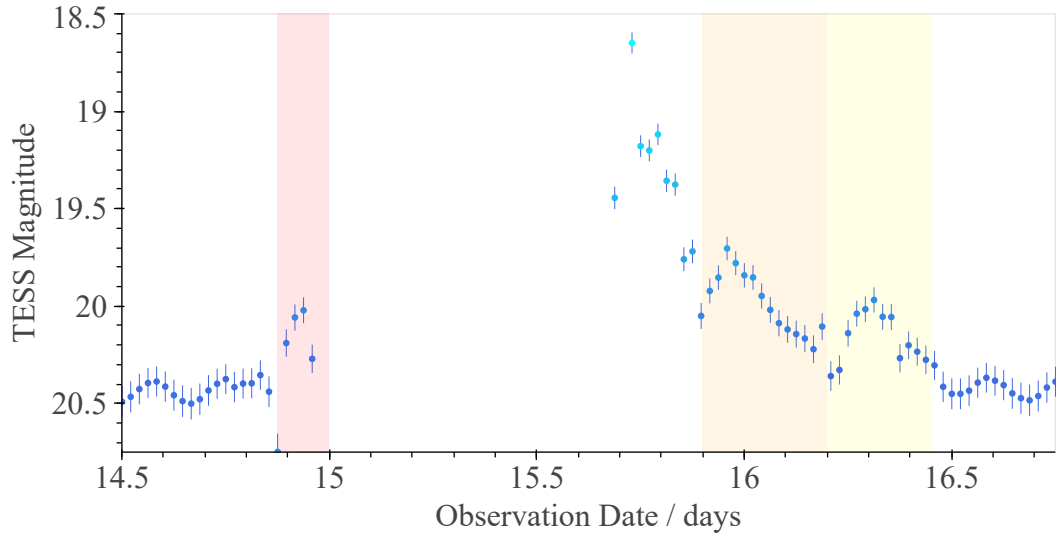


Figure 9.14: TESS photometry of J151503.52-433712.50, showing an outburst of  $\simeq 2$  mag, the start of which is indicated by the red region. Two possible echo outbursts during the primary outburst’s decay are highlighted by regions in orange and yellow.

### 9.2.3.2 J112024.12-544200.90

The second candidate, GAIA DR3 5346631922949364864, exhibits slightly noisy modulation on a period of 8.65 h, with a spike in brightness at each maximum visible in its TESS and ATLAS light curves. The typical spectral type of this system is F9V.

### 9.2.3.3 J075851.54-182100.06

This system, GAIA DR3 5714874451749946752, is included due to the asymmetry in the shape of its minima. This modulation of this system is particularly slow among the candidates returned by the search, with an orbital period of 41.96 h. The typical spectral type of this system is K2V.

### 9.2.3.4 J052830.76-045403.73

Like J133030.39-361425.93, this system (GAIA DR3 3209691560665300096) is included due to the long-term variability in its ATLAS light curves—as shown in Fig. 9.13. The rate of modulation in this system is also similar to that of J133030.39-361425.93, with an orbital period of 8.52 h. The typical spectral type of this system is G5V.

### 9.2.3.5 J151503.52-433712.50

The final candidate to be included here, GAIA DR3 6003468452715574528, is featured due to the noise in its phase-folded light curve, and the presence of an outburst in its TESS photometry (Fig. 9.14). The typical spectral type of this system is G1V.

A full table of black hole binary candidates, all of which exhibit ellipsoidal modulation similar to those featured here and do not have a confirmed classification, can be found in Appendix B.

## 9.3 Summary

From an initial set of 72 expected or dynamically confirmed black hole X-ray binaries, a refined set of four reference systems was obtained. Through these, a number of filtering criteria were derived and consequently applied to a cross-match of Gaia's third data release with the first data release of eROSITA-DE. The result of this was a set of 17 450 systems, the brightest 3 000 of which were subjected to further analysis via ATLAS and TESS photometry. The final set of candidates is comprised of 322 systems, all of which exhibit clear periodicity in their brightness modulation. Further exploration revealed the distribution of orbital periods, typical spectral types, and X-ray fluxes among these candidates, and identified the main contaminants faced by the search. Of these 322 systems, 35 exhibit unambiguous ellipsoidal modulation in their phase-folded photometry—none of which have a published classification in the available literature. These systems are shown in Appendix B and will require further follow-up at a later date.

# Chapter 10

## Discussion

### 10.1 Contamination

Setting aside the systems of interest, both searches reveal an important problem faced by work of this kind: contamination.

#### 10.1.1 Contaminants in the White Dwarf Pulsar Search

As shown in Table 8.2, the primary contaminants in this search are SU UMa systems and polars. These systems were already discussed in Chapter 4, and so they will not be described again here.

#### 10.1.2 Contaminants in the X-ray Binary Search

The primary contaminants in this search are clear from Fig. 9.11: Algol and W UMa variables. Since these are not compact binaries and hence have not yet been introduced, they will be briefly described here. The former are close binary (or higher multiple) systems in which one component is usually an F–K-type giant and the other is a hot dwarf [Hoffman et al., 2008]. These systems are typically semi-detached, with the giant transferring material to its lower mass companion. Eclipses in the phase-folded light curves of these systems are well-defined due to both components being of similar size—despite their greatly differing masses [Budding et al., 2004]. These eclipses are typically of differing magnitude owing to the differences in brightness of the two components, and are also preceded/followed by periods of relative standstill in brightness [Hoffman et al., 2008]. An example is shown in the first panel of Fig. 10.1. Algols are known X-ray sources, hence their detection by eROSITA. The mechanism behind this emission is not well-understood,

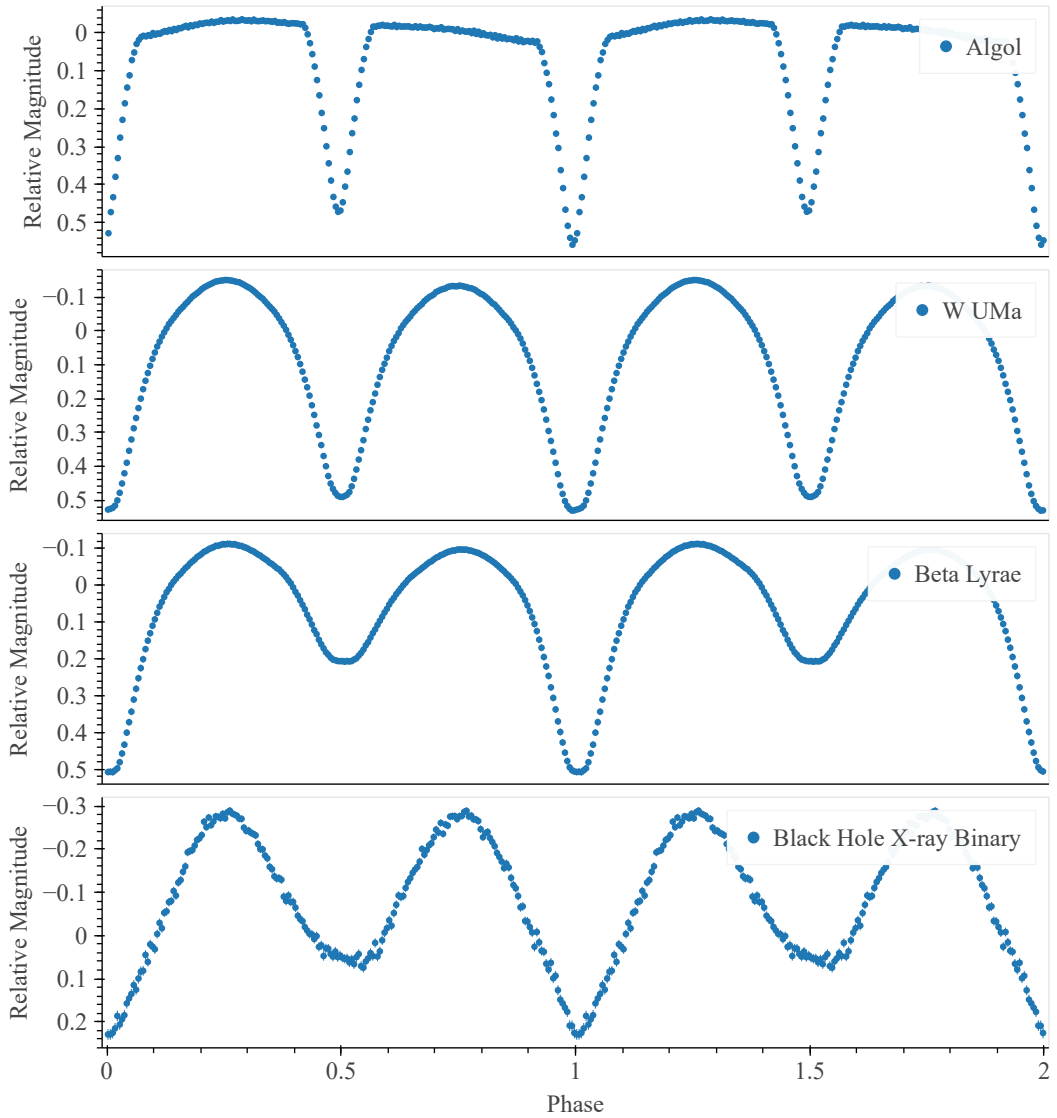


Figure 10.1: Phase-folded TESS light curves of various known systems. First panel: J150604.21–274721.32, a known Algol variable, folded on a period of  $\simeq 20.1$  h. Second panel: J094345.47+555709.06, a known W UMa contact binary, folded on a period of  $\simeq 8.0$  h. Third panel: J145123.85–374047.06, a known  $\beta$  Lyrae variable, folded on a period of  $\simeq 32.1$  h. Fourth panel: J165400.14–395044.76, a known black hole X-ray binary, folded on a period of  $\simeq 62.9$  h. This system is one of four reference systems used in this work. All light curves are split into 200 equally spaced bins in time.

but is thought to result from interactions with a dynamo-driven magnetic field that is generated by the rapid spin of the tidally-locked components [Ness et al., 2002].

W UMa variables are contact binaries: systems in which the orbital separa-

tion is so low that the components are touching or share a common envelope [Latković et al., 2021]. As a result of their proximity, the orbital periods in W UMa systems are typically  $\simeq 6 - 48$  h and the binary components are distorted into an ellipsoidal shape by the effect of their companion’s gravity. The projected area of each component therefore changes through the orbital cycle, resulting in the phase-folded light curves of these systems exhibiting ellipsoidal modulation. Similarly to Algols, W UMa systems are known X-ray emitters. The mechanism of X-ray emission in these systems is also not well-understood but is expected to be similar to that described above [Chen et al., 2006]. The components in W UMa systems are typically of similar spectral types and hence similar luminosities [Kraft, 1967], and so a key property of these systems is that consecutive minima are often of similar magnitude. An example is shown in the second panel of Fig. 10.1.

A third class of systems that are expected to contaminate X-ray binary searches such as the one performed here are  $\beta$  Lyrae variables. The components in these systems can be at varying evolutionary stages and are typically close enough to be interacting [Hoffman et al., 2008]. Similarly to W UMa variables, the tidal deformation of one or both components results in the phase-folded light curves of  $\beta$  Lyrae variables exhibiting ellipsoidal modulation. Unlike W UMa systems, however, consecutive minima are often asymmetrical owing to the different luminosities of the components [Lucy, 1968]. An example is shown in the third panel of Fig. 10.1.

While making a comparison to similar searches for white dwarf pulsars is difficult owing to the recency of their discovery, the problem of contamination by contact or near-contact binaries in X-ray binary searches is not exclusive to the one performed here. An example can be found in Gomel et al. [2023], which is also discussed in O’Doherty et al. [2024]. The search performed by Gomel et al. [2023] returned 6 306 detached or weakly-accreting black hole/neutron star candidates, but seems to be contaminated by a large number of non-X-ray binary systems. The extent of this contamination is not yet fully known, but one of its most promising candidates is now expected to instead be a contact binary [O’Doherty et al., 2024].

### 10.1.3 The Problem of Contamination

In either search, the difficulty of removing contaminants stems from the clear similarities of their observable properties to the target systems—and from how these properties manifest in their luminosity variation. Both polars and SU UMa systems occupy a very similar region of the HRD to the three known white dwarf pulsars (Fig. 10.2), and show a similar magnitude of variability in their light curves as a result of interaction between their components. Both are also known X-ray sources

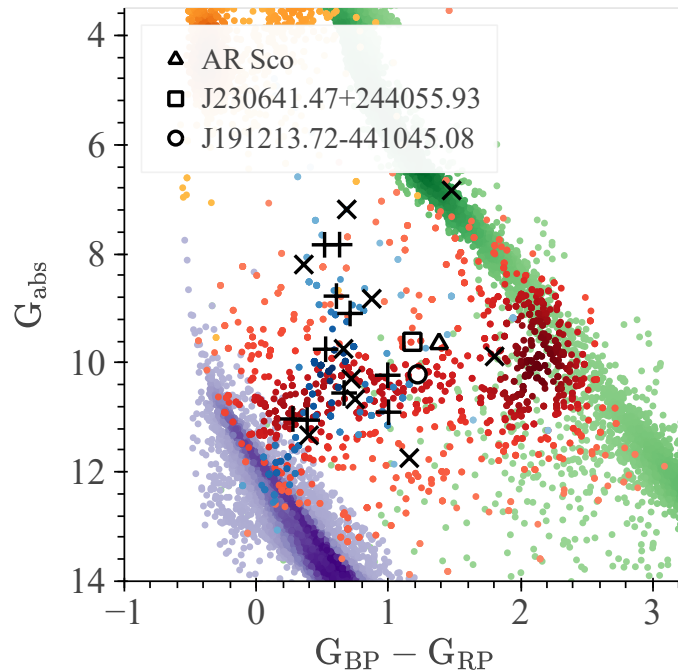


Figure 10.2: Left panel: Gaia Hertzsprung-Russell diagram showing the positions of known SUUMa (marked by ‘+’) and polar (marked by ‘x’) systems relative to the three known white dwarf pulsars. Background (colour) sample is a 100 pc Gaia sample split into various sub-groups. Green: clean sample of stars, yellow: clean sample of spectroscopically confirmed subdwarfs, blue: clean sample of spectroscopically confirmed cataclysmic variables, red: clean sample of spectroscopically confirmed white dwarf + M-dwarf binaries, purple: clean sample of white dwarfs. Background samples provided by B. Gänsicke.

and the latter have an additional parallel in that they are strongly magnetic (see Chapter 4). The same is true for the contaminants of the X-ray binary search: all expected (and observed) contaminants in the final set of candidates are interacting, highly variable X-ray sources which occupy a similar region of the HRD and have orbital periods that are typically well-defined and relatively short. The similarities in the light curves of these contaminants are perhaps even more problematic than those in the search for white dwarf pulsars, as is immediately clear from Fig. 10.1. The bottom panel of this figure shows the phase-folded light curve of the known transient black hole binary J165400.14–395044.76, a reference system used in this work. This system was also seen in Table 9.1 and Figs. 9.5 and 9.6. Much like the systems in the second and third panels of Fig. 10.1, this system exhibits ellipsoidal modulation due to the deformation of one or both of its binary components—a defining feature of black hole binaries. With the exception of Algol systems, whose light

curves are fairly distinctive owing to the shape of their eclipses, this clear similarity proves to be a significant problem in the identification of non-transient black hole binaries.

## 10.2 Search Optimisation

Despite this, there are several ways in which the problem of contamination may be reduced—hence improving the efficacy of searches of the kind performed here.

With the main contaminants in each search known, an initial source of improvement is the optimisation of filtering criteria. An effective criterion aims to either maximise the number of candidate systems, reduce the number of contaminants, or achieve both simultaneously. An example of the former can be found in the astrometric excess noise (AEN) from Gaia. As discussed in Gandhi et al. [2021], “astrometric excess noise in excess of parallax and proper motion is a potential signature of orbital wobble of individual components in binary star systems”. While this parameter was already used in both searches to ensure high-quality astrometry ( $\text{AEN} < 0.5$ ), a *large* AEN may therefore be a good indicator of the presence of a companion. The parameter used by Gandhi et al. is the AEN significance (AENS), with  $\text{AENS} \geq 2$  indicating a significant AEN. The results which they report are promising, with a sizeable increase in the number of suspected interacting binaries in their obtained populations. This same study suggests that the similarity of AEN to RUWE would imply that the latter may also have some correlation with expected binarity, and this does indeed seem to be the case [Castro-Ginard et al., 2024]. While the optimisation of these criteria wouldn’t necessarily be expected to remove many contaminants from the searches performed here (as the majority of these were already in binary configurations), there is still the potential to increase the completeness of the search. It is important to note that the use and interpretation of either of these parameters is not simple, as neither is purely sensitive to binarity. Other influences which cannot be ignored include errors in the attitude (orientation control) of the Gaia satellite, partially resolved double stars, source variability and other systematic effects. Furthermore, a low AENS does not necessarily indicate that a system is not a binary: enforcing a criterion of  $\text{AENS} > 2$ , as used by Gandhi et al. [2021], would result in the loss of three reference systems from the X-ray binary search and two from the white dwarf pulsar search. A more conservative implementation may therefore be superior in the searches performed here.

Along with optimising the existing criteria, the potential of previously unused

observable properties as a means of reducing contamination must also be considered. An example of this can be found in Gomel et al. [2023], whose X-ray binary candidates were required to exhibit asymmetrical minima in their modulation. The modulation of the systems in Fig. 10.1 suggests that a criterion of this kind could be an effective means of differentiating Algol and  $\beta$  Lyrae contaminants from black hole binary candidates. Another criterion used by Gomel et al. is the imposition of a lower limit on the orbital periods of their candidates. Contact binaries (such as the W UMa systems that contaminated the search for X-ray binaries) typically have very short orbital periods as a result of their close configuration. Consequently, the presence of these may be reduced by restricting the search to candidates with longer orbital periods. This criterion may also be applicable to the search for white dwarf pulsars, as both polars and SU UMa systems have typical orbital periods of  $\simeq 2$  h—half that of the known white dwarf pulsars [Olech et al., 2011; Butters et al., 2009]. Of course, the drawback in either case is that particularly closely-orbiting candidate systems are likely to be lost. It is also important to note that the criterion of  $P_{\text{orb}} > 0.25$  d used by Gomel et al. was not sufficient to remove all contact binary contaminants from their obtained candidates [O’Doherty et al., 2024]. The same is true of the AENS and RUWE criteria discussed above: a poor choice of cutoff value in either may not only cause the criterion to be a sub-optimal means of ensuring binarity, but may also introduce a great number of additional contaminants with poorly defined astrometry. This is a key point: the efficacy of any possible criterion (including those that were already used in this work) depends heavily on the choice of cutoff value. This requirement of fine-tuning may not be overly problematic in searches for which there are already a significant number of known systems, but that is not the case in either search performed here. In the search for white dwarf pulsars, this was a result of the recency of their discovery, while in the search for X-ray binaries, it was due to the inherent difficulty of obtaining high-quality photometry and astrometry for systems that are typically extremely faint. In either case, it is therefore not certain whether the derived criteria effectively represent the target population as a whole. This is particularly problematic in parameters which exhibit a large amount of variance among the reference systems, such as parallax/proper motion significance ( $\alpha_p/\alpha_\mu$ ), and the Gaia variability parameter ( $V_G$ ). Furthermore, this problem is made even more significant by its circularity: the derivation of optimal filtering criteria requires a representative sample of reference systems, and the ease of acquiring these systems is itself heavily dependent on the criteria which are used. It is therefore also important to consider other means by which populations of known systems may be expanded.

## 10.3 Future Developments

### 10.3.1 Instrumentation

In the case of X-ray binaries, a key recent advancement is the advent of gravitational wave detections, which allow for massive objects like the black holes/neutron stars in X-ray binaries to be probed. However, gravitational wave detections are heavily biased towards the most massive systems due to the limitations of current detectors [Cúneo et al., 2023]. Another advancement in recent decades is the study of microlensing, in which photometric (and more recently, astrometric) signals caused by the lensing (bending) of light around a massive object such as a neutron star or black hole are detected [Lam et al., 2022]. Similarly to mass estimations via radial velocity measurements (Eq. 7.1), this method allows for the detection of X-ray binaries in the absence of any interaction (i.e. detached systems). Through the history of compact binary research, observations of transient outbursts have clearly been an effective means of identifying X-ray binaries—but the infrequency of these transient events (or the complete lack of such events in some systems) significantly limits the rate at which these systems are discovered [Cúneo et al., 2023].

The applicability of the above methods to white dwarf pulsars is largely set by the dependence of their observation mechanism on the mass of the binary components. Current gravitational wave detections have been limited to mergers of massive compact binaries—neutron stars and black holes. However, with upcoming advances in detection sensitivities such as the Laser Interferometer Space Antenna (LISA), this is set to change [Georgousi et al., 2022]. While many photometric microlensing events have been observed, astrometric microlensing remains a relatively new area—with its first detection originating from a white dwarf in 2017 [Sahu et al., 2017]. The detection of a lone white dwarf in 2022 by McGill et al. clearly shows the potential of this method as a means of identifying these systems, but much like those discussed above, this method is significantly limited by the rarity and randomness of these events. Similarly to the detection of gravitational waves, however, future developments in photometric/astrometric (i.e. Gaia-like) surveys are expected to reduce the significance of this problem.

#### 10.3.1.1 Spectroscopic Surveys

The utility of spectra in the determination of the fundamental properties of compact binary systems, such as magnetic field strengths, elemental abundances, component luminosity contributions, mass transfer rates and mass constraints via radial veloc-

ity measurements results in them being the most necessary stage in a given system’s classification. Advancements in the precision and availability of spectra are therefore of the utmost importance, with the latter being particularly relevant in searches that return a large number of candidates. One of the most important developments towards this goal is the adoption of multi-object spectroscopy in modern spectroscopic surveys—e.g. the Dark Energy Spectroscopic Instrument (DESI, DESI Collaboration et al. [2016]), the WHT Enhanced Area Velocity Explorer (WEAVE, Dalton et al. [2012]), the 4-metre Multi-Object Spectrograph Telescope (4MOST, De Jong et al. [2019]) and SDSS-V (Kollmeier et al. [2019]). These will bring with them a new age in system classification, with the unprecedented availability of astrophysical spectra.

### 10.3.2 Novel Approaches

Just as the methods discussed above have been, and continue to be, improved with time, recent or entirely new approaches will likely be of great utility in the future.

A recent example can be found in Casares [2015], which found a correlation between the full width at half-maximum (FWHM) of the  $H\alpha$  emission line and the radial velocity semi-amplitude of the donor. When combined with orbital periods in Eq. 7.1, this allows for the mass of a compact component to be constrained from a single spectrum of lower resolution [Casares, 2015]. The applicability of this approach also extends beyond the typical magnitude limits faced by other approaches by  $\simeq 2.5$  mag, allowing for these constraints to be made in significantly fainter systems than has previously been possible. An additional correlation has also been proposed even more recently in Cúneo et al. [2023], which instead relates the donor’s radial velocity semi-amplitude to the FWHM of near-infrared lines. This extends the magnitude limit of this approach even further and is of particular utility in systems that are heavily reddened due to extinction—a significant problem for X-ray binaries located along the galactic plane [Cúneo et al., 2023].

Another recently proposed approach can be found in Rodriguez [2024]. The tool presented here is the “X-ray Main Sequence” which, similarly to the HR diagram, is used to split stars by their spectral properties. Unlike the HRD, however, this diagram compares the optical colour of a system (e.g. Gaia  $G_{BP} - G_{RP}$ ) to the ratio of its X-ray flux to its optical flux. An example of the X-ray main sequence is shown in Figure 1 of Rodriguez [2024], where it has been shown to be a viable way of separating accreting compact objects from many other systems. Examples include YSOs (e.g. the system discovered in this work, J035055.99–204815.82), active stars (e.g. the possible T Tauri candidate indicated in Fig. 9.11), active binaries (e.g. the

RS CVn candidate indicated in Fig. 9.11) and symbiotic binaries. Given that these systems were identified among the various contaminants of both searches, the application of this tool to the candidates acquired in this work shows significant promise. Unlike the work performed here, the diagram shown in Figure 1 of Rodriguez [2024] uses a cross-match of Gaia with XMM-Newton (an earlier X-ray survey). However, this same approach was applied to an early data release of eROSITA in Figure 4 of the same source and was similarly shown to be an effective means of identifying accreting compact objects.

## 10.4 Further Work

### 10.4.1 The White Dwarf Pulsar Search

As noted previously, a number of the systems returned by this search will require further follow-up at a later date due to the time constraints of an MSc. To this end, we are currently in the process of obtaining spectroscopy for the white dwarf pulsar candidate, J201135.84–021340.49, to confirm or refute the system as a fourth white dwarf pulsar.

### 10.4.2 The X-ray Binary Search

Similarly, the 35 ellipsoidal candidates returned by the X-ray binary search will require further follow-up at a later date. Additionally, and especially if any of these candidates are consequently identified as X-ray binaries, the potential to expand this search to the full set of 17 450 derived systems remains. Due to the time investment that this would require, it may be worth initially prioritising a further reduction of this sample—using the candidate/contaminant systems obtained so far to guide this. Beyond the further identification of possible candidate systems, the samples acquired here offer the possibility to be used as a testbed for any of the optimisations discussed above. Of course, the utility of these samples for this purpose scales with the number of candidates/contaminants that have already been identified, and so this should be the priority.

# Chapter 11

## Conclusions

The goal of this work was to expand the populations of two elusive compact binary configurations: white dwarf pulsars and X-ray binaries. A Python package, Astro-Toolkit, was developed to facilitate the retrieval and analysis of archival data from a variety of surveys, with the starting point in either search being Gaia’s third data release. In the X-ray binary search, Gaia DR3 was cross-matched with eROSITA’s first data release to obtain an initial sample of X-ray sources. In either search, a set of filtering criteria was then derived from a set of chosen reference systems. These criteria included cuts in the Gaia Hertzsprung-Russell diagram and various parameters which ensured variability and high-quality astrometry among the resulting systems. These, along with further analysis through light curves and time series analysis, resulted in a set of 58 white dwarf pulsar candidates and 322 X-ray binary candidates. The main contaminants in either set of returned systems were identified through any available literature, and a number of the obtained white dwarf pulsar candidates were subjected to further investigation through high-speed photometry from the Thailand National Telescope and spectroscopy from the Hale and Shane Telescopes.

Despite the difficulties inherent to either search performed in this work, both were ultimately successful. The search for white dwarf pulsars returned at least one promising candidate which requires further investigation, and revealed a number of otherwise interesting systems. A further look into these systems, in the form of newly acquired data ranging from phase-resolved spectra to high-speed photometry, revealed their properties beyond what was available previously. Outside of limitations in survey coverages, this search retained all three reference systems among its candidates, strongly indicating that searches of this kind are a viable approach for the identification of white dwarf pulsars.

While the set of derived X-ray binary candidates was not subjected to analysis of the same depth, the search successfully highlighted the difficulties faced by projects of its kind and identified a number of key contaminants which have been present across successful searches in other work. Ignoring a lack of eROSITA detections, two of the four reference systems would have been retained in the final set of candidates. One would have been lost due to its location along the galactic plane, while the other would have been lost due to it showing no clear periodicity. Once again, the retention of these known systems suggests that searches of this kind do have the potential to be used as a means of identifying X-ray binaries.

It is also important to note that due to the time constraints of an MSc, neither set of derived candidates has been fully explored. The true success level of either search (beyond that which has already been achieved) is therefore difficult to gauge and will become more clear following the future work that has been outlined above. This is especially true for the X-ray binary search, in which only the brightest 3 000 of a total of 17 450 potential candidate systems were the subject of further investigation.

The primary contaminants in each search have been explored, and possible optimisations to maximise the success of similar searches have been discussed. Alongside the advent of new approaches and technologies, searches of the kind performed here show clear promise for the identification of compact binaries in the future.

# Bibliography

- B. P. Abbott, R. Abbott, T. D. Abbott, M. R. Abernathy, F. Acernese, K. Ackley, C. Adams, T. Adams, P. Addesso, R. X. Adhikari, et al. Observation of gravitational waves from a binary black hole merger. *Phys. Rev. Lett.*, 2016.
- S. Abdollahi, F. Acero, M. Ackermann, M. Ajello, W. B. Atwood, M. Axelsson, L. Baldini, J. Ballet, G. Barbiellini, D. Bastieri, et al. Fermi large area telescope fourth source catalog. *The Astrophysical Journal Supplement Series*, 2020.
- E. G. Adelberger, A. García, R. G. H. Robertson, K. A. Snover, A. B. Balantekin, K. Heeger, M. J. Ramsey-Musolf, D. Bemmerer, A. Junghans, C. A. Bertulani, et al. Solar fusion cross sections. ii. the *pp* chain and cno cycles. *Reviews of Modern Physics*, 2011.
- A. L. Antunes, J. Munday, M. Vučković, I. Pelisoli, P. Németh, M. Zorotovic, T. R. Marsh, S. P. Littlefair, V. S. Dhillon, and A. J. Brown. The double low-mass white dwarf eclipsing binary system j2102-4145 and its possible evolution. *Astronomy and Astrophysics*, 2024.
- ATLAS. [ATLAS Forced Photometry](#), 2024. Accessed 22-07-24.
- ATLAS. , 2025. Accessed 01-03-25.
- T. Augusteijn, E. Kuulkers, and J. Shaham. “Glitches” in soft X-ray transients : echoes of the main burst? *Astronomy and Astrophysics*, 1993.
- Australian National University. , 2025. Accessed 01-03-25.
- J. Bailey, J. H. Hough, R. Gilmozzi, and D. J. Axon. Infrared and optical polarimetry of AM Herculis. *Monthly Notices of the Royal Astronomical Society*, 1984.
- E. J. Barlow, C. Knigge, A. J. Bird, A. J. Dean, D. J. Clark, A. B. Hill, M. Molina, and V. Sguera. 20–100 keV properties of cataclysmic variables detected in the integral/ibis survey. *Monthly Notices of the Royal Astronomical Society*, 2006.

- E. D. Barr, Dutta A., P. C. C. Freire, M. Cadelano, T. Gautam, M. Kramer, C. Palanca, S. M. Ransom, A. Ridolfi, B. W. Stappers, et al. A pulsar in a binary with a compact object in the mass gap between neutron stars and black holes. *Science*, 2024.
- G. Bath. Periodicities and disks in dwarf novae. *Nature Physical Science*, 1973.
- K. Belczynski, R. Perna, T. Bulik, V. Kalogera, N. Ivanova, and D. Q. Lamb. A study of compact object mergers as short gamma-ray burst progenitors. *The Astrophysical Journal*, 2006.
- E. Bellm and S. Kulkarni. The unblinking eye on the sky. *Nature Astronomy*, 2017.
- E. C. Bellm, S. R. Kulkarni, M. J. Graham, R. Dekany, R. M. Smith, R. Riddle, F. J. Masci, G. Helou, T. A. Prince, S. M. Adams, et al. The zwicky transient facility: System overview, performance, and first results. *Publications of the Astronomical Society of the Pacific*, 2018.
- D. Belloni and M. R. Schreiber. *Formation and Evolution of Accreting Compact Objects*. Springer, Singapore, 2023.
- D. Belloni, M. R. Schreiber, M. Zorotovic, K. Ilkiewicz, J. R. Hurley, M. Giersz, and F. Lagos. No cataclysmic variables missing: higher merger rate brings into agreement observed and predicted space densities. *Monthly Notices of the Royal Astronomical Society*, 2018.
- F. Bernardini, D. de Martino, K. Mukai, M. Falanga, and N. Masetti. 2PBC J0658.0–1746: a hard X-ray eclipsing polar in the orbital period gap. *Monthly Notices of the Royal Astronomical Society*, 2019.
- K. Beuermann, V. Burwitz, K. Reinsch, A. Schwope, and H.-C. Thomas. Neglected x-ray discovered polars - iii. rx j0154.0–5947, rx j0600.5–2709, rx j0859.1+0537, rx j0953.1+1458, and rx j1002.2–1925. *AA*, 2021.
- R. D. Blandford and R. L. Znajek. Electromagnetic extraction of energy from Kerr black holes. *Monthly Notices of the Royal Astronomical Society*, 1977.
- J. M. Blondin and M. P. Owen. Wind Accretion VS Roche Lobe Overflow in HMXBs. In *Accretion Phenomena and Related Outflows*, Astronomical Society of the Pacific Conference Series, 1997.

- J. J. Bochanski, S. L. Hawley, K. R. Covey, A. A. West, I. Neill Reid, D. A. Golimowski, and Ž. Ivezić. The Luminosity and Mass Functions of Low-mass Stars in the Galactic Disk. II. The Field. *The Astronomical Journal*, 2010.
- Bokeh. [Bokeh Plotting Library](#), 2024. Accessed 17-06-24.
- D. Boyd, P. de Ponthiere, J. Foote, M. Julian, T. Kato, R. Koff, T. Krajci, G. Poyner, J. Shears, and B. Staels. CCD photometry of the first observed superoutburst of KP Cassiopeiae in 2008 October. *Journal of the British Astronomical Association*, 2010.
- E Bozzo, P Romano, C Ferrigno, and L Oskinova. The symbiotic x-ray binaries set x-1, 4u 1700+24, and igr j173292731. *Monthly Notices of the Royal Astronomical Society*, 2022.
- M. Brightman, M. Bachetti, H. P. Earnshaw, F. Fürst, J. García, B. Grefenstette, M. Heida, E. Kara, K. K. Madsen, M. J. Middleton, et al. Breaking the limit: Super-eddington accretion onto black holes and neutron stars, 2019.
- V. Buat-Ménard and J.-M. Hameury. Superoutbursts, superhumps and the tidal-thermal instability model. *Astronomy and Astrophysics*, 2002.
- E. Budding, A. Erdem, C. Çiçek, I. Bulut, F. Soydugan, E. Soydugan, V. Bakiş, and O. Demircan. Catalogue of Algol type binary stars. *Astronomy and Astrophysics*, 2004.
- M. R. Burleigh, F. J. Clarke, E. Hogan, C. S. Brinkworth, P. Bergeron, P. Dufour, P. D. Dobbie, A. J. Levan, S. T. Hodgkin, D. W. Hoard, et al. The ‘DODO’ survey — I. Limits on ultra-cool substellar and planetary-mass companions to van Maanen’s star (vMa 2). *Monthly Notices of the Royal Astronomical Society: Letters*, 2008.
- O. W. Butters, S. Katajainen, A. J. Norton, H. J. Lehto, and V. Piirola. Circular polarization survey of intermediate polars i. northern targets in the range  $17\text{ h } j\text{ ra } j\text{ 23 h}$ . *Astronomy and Astrophysics*, 2009.
- D. T. Caditz. Adiabatic shocks in accretion flows. *The Astrophysical Journal*, 1998.
- M. Caleb, I. Heywood, K. Rajwade, M. Malenta, B. Willem Stappers, E. Barr, W. Chen, V. Morello, S. Sanidas, J. van den Eijnden, et al. Discovery of a radio-emitting neutron star with an ultra-long spin period of 76s. *Nature Astronomy*, 2022.

- Caltech. , 2025. Accessed 25-02-25.
- Palomar Observatory Caltech. [Double Spectrograph \(DBSP\) Overview](#), 2020. Accessed 07-08-24.
- Palomar Observatory Caltech. [The 200-inch \(5.1-meter\) Hale Telescope](#), 2023. Accessed 07-08-24.
- L. Capitanio, R. Lallement, J. L. Vergely, M. Elyajouri, and A. Monreal-Ibero. Three-dimensional mapping of the local interstellar medium with composite data. *Astronomy and Astrophysics*, 2017.
- J. Casares. A FWHM- $K_2$  Correlation in Black Hole Transients. *The Astrophysical Journal*, 2015.
- A. Castro-Ginard, Z. Penoyre, A. R. Casey, A. G. A. Brown, V. Belokurov, T. Cantat-Gaudin, R. Drimmel, M. Fouesneau, S. Khanna, E. P. Kurbatov, et al. Gaia dr3 detectability of unresolved binary systems. *Astronomy and Astrophysics*, 2024.
- CDS. [SIMBAD](#), 2024a. Accessed 17-06-24.
- CDS. [Vizier](#), 2024b. Accessed 14-06-24.
- S. Chandrasekhar. Xlviii. the density of white dwarf stars. *The London, Edinburgh, and Dublin Philosophical Magazine and Journal of Science*, 1931.
- S. Chandrasekhar. The Maximum Mass of Ideal White Dwarfs. *The Astrophysical Journal*, 1931.
- S. Chandrasekhar. The Highly Collapsed Configurations of a Stellar Mass. (Second Paper.). *Monthly Notices of the Royal Astronomical Society*, 1935.
- W. P. Chen, K. Sanchawala, and M. C. Chiu. W Ursae Majoris Contact Binary Variables as X-Ray Sources. *The Astrophysical Journal*, 2006.
- X. Chen, S. Wang, L. Deng, R. de Grijs, M. Yang, and H. Tian. The zwicky transient facility catalog of periodic variable stars. *The Astrophysical Journal Supplement Series*, 2020.
- X. Chen, Z. Liu, and Z. Han. Binary stars in the new millennium. *Progress in Particle and Nuclear Physics*, 2024.

- L. Chomiuk, B. D. Metzger, and K. J. Shen. New insights into classical novae. *Annual Review of Astronomy and Astrophysics*, 2021.
- A. M. Cody, J. Stauffer, A. Baglin, G. Micela, L. M. Rebull, E. Flaccomio, M. Morales-Calderón, S. Aigrain, J. Bouvier, L. A. Hillenbrand, et al. CSI 2264: Simultaneous Optical and Infrared Light Curves of Young Disk-bearing Stars in NGC 2264 with CoRoT and Spitzer—Evidence for Multiple Origins of Variability. *The Astrophysical Journal*, 2014.
- A. M. Cody, L. A. Hillenbrand, T. J. David, J. M. Carpenter, M. E. Everett, and S. B. Howell. A Continuum of Accretion Burst Behavior in Young Stars Observed by K2. *The Astrophysical Journal*, 2017.
- D. L. Coppejans and C. Knigge. The case for jets in cataclysmic variables. *New Astronomy Reviews*, 2020.
- J. M. Corral-Santana. [BlackCAT: A catalogue of stellar-mass black holes in X-ray transients](#), 2024. Accessed 22-06-24.
- J. M. Corral-Santana, J. Casares, T. Muñoz-Darias, F. E. Bauer, I. G. Martínez-Pais, and D. M. Russell. Blackcat: A catalogue of stellar-mass black holes in x-ray transients. *Astronomy and Astrophysics*, 2016.
- M. Cropper. The polars. *Space Science Reviews*, 1990.
- M. Cropper, K. Mukai, K. O. Mason, A. P. Smale, P. A. Charles, J. P. D. Mittaz, G. Machin, B. J. M. Hassall, P. J. Callanan, T. Naylor, et al. Cyclotron humps in am her systems: variations around the orbit in dp leo. *Monthly Notices of the Royal Astronomical Society*, 1990.
- CU Boulder. [White Dwarfs as Polytropes](#), 2003. Accessed 31-07-24.
- V. A. Cúneo, J. Casares, M. Armas Padilla, J. Sánchez-Sierras, J. M. Corral-Santana, T. J. Maccarone, D. Mata Sánchez, T. Muñoz Darias, M. A. P. Torres, and F. Vincentelli. An infrared FWHM–K2 correlation to uncover highly reddened quiescent black holes. *Astronomy and Astrophysics*, 2023.
- V. A. Cúneo, J. Casares, M. Armas Padilla, J. Sánchez-Sierras, J. M. Corral-Santana, T. J. Maccarone, D. Mata Sánchez, T. Muñoz-Darias, M. A. P. Torres, and F. Vincentelli. An infrared fwhm–k2 correlation to uncover highly reddened quiescent black holes. *Astronomy and Astrophysics*, 2023.

- G. Dalton, S. C. Trager, D. C. Abrams, D. Carter, P. Bonifacio, J. A. L. Aguerri, M. MacIntosh, C. Evans, I. Lewis, R. Navarro, et al. WEAVE: the next generation wide-field spectroscopy facility for the William Herschel Telescope. In *Ground-based and Airborne Instrumentation for Astronomy IV*, 2012.
- T. Damour. *Binary Systems as Test-Beds of Gravity Theories*. Springer Netherlands, 2009.
- J. A. de Jong, J. van Paradijs, and T. Augusteijn. Reprocessing of X rays in low-mass X-ray binaries. *Astronomy and Astrophysics*, 1996.
- R. S. De Jong, O. Agertz, A. A. Berbel, J. Aird, D. A. Alexander, F. Amarsi, A. and Anders, R. Andrae, B. Ansarinejad, W. Ansorge, et al. 4most: Project overview and information for the first call for proposals. *Published in The Messenger vol. 175*, 2019.
- CNRS Observatoire de Paris. [Stilism](#), 2024. Accessed 18-06-24.
- E. Dederick and J. Jackiewicz. A Possible Mechanism for Driving Oscillations in Hot Giant Planets. *The Astrophysical Journal*, 2017.
- DESI Collaboration, A. Aghamousa, J. Aguilar, S. Ahlen, S. Alam, L. E. Allen, C. Allende Prieto, J. Annis, S. Bailey, C. Balland, et al. The DESI Experiment Part I: Science, Targeting, and Survey Design. *arXiv e-prints*, 2016.
- V. S. Dhillon, T. R. Marsh, D. C. Atkinson, N. Bezawada, M. C. P. Bours, C. M. Copperwheat, T. Gamble, L. K. Hardy, R. D. H. Hickman, P. Irawati, et al. ULTRASPEC: a high-speed imaging photometer on the 2.4-m Thai National Telescope. *Monthly Notices of the Royal Astronomical Society*, 2014.
- M. Dillon, B. T. Gänsicke, A. Aungwerojwit, P. Rodríguez-Gil, T. R. Marsh, S. C. C. Barros, P. Szkody, S. Brady, T. Krajci, and A. Oksanen. Orbital periods of cataclysmic variables identified by the SDSS – III. Time-series photometry obtained during the 2004/5 International Time Project on La Palma. *Monthly Notices of the Royal Astronomical Society*, 2008.
- N. Duric. *Advanced Astrophysics*. Cambridge University Press, 2003.
- K. El-Badry, C. Conroy, J. Fuller, R. Kiman, J. van Roestel, A. C. Rodriguez, and K. B. Burdge. Magnetic braking saturates: evidence from the orbital period distribution of low-mass detached eclipsing binaries from ZTF. *Monthly Notices of the Royal Astronomical Society*, 2022.

- I. El Mellah, A. A. C. Sander, J. O. Sundqvist, and R. Keppens. Formation of wind-captured disks in supergiant x-ray binaries - consequences for vela x-1 and cygnus x-1. *Astronomy and Astrophysics*, 2019.
- European Space Agency. , 2025. Accessed 20-02-25.
- A. C. Fabian. Black holes at work. *Astronomy Geophysics*, 2009.
- M. Fausnaugh. , 2025. Accessed 03-02-25.
- É. É. Flanagan and S. A. Hughes. The basics of gravitational wave theory. *New Journal of Physics*, 2005.
- F. M. Fornasini, V. Antoniou, and G. Dubus. High-mass x-ray binaries, 2023.
- Gaia Collaboration. [Gaia Data Release Documentation](#), 2024. Accessed 09-07-24.
- Gaia Collaboration, T. Prusti, J. H. J. de Bruijne, A. G. A. Brown, A. Vallenari, C. Babusiaux, C. A. L. Bailer-Jones, U. Bastian, M. Biermann, D. W. Evans, et al. The Gaia mission. *Astronomy and Astrophysics*, 2016.
- P. Gandhi, D. A. H. Buckley, P. A. Charles, S. Hodgkin, S. Scaringi, C. Knigge, A. Rao, J. A. Paice, and Y. Zhao. Astrometric excess noise in Gaia EDR3 and the search for X-ray binaries. *Monthly Notices of the Royal Astronomical Society*, 2021.
- B. T. Gänsicke. Observational population studies of cataclysmic variables - The golden era of surveys. In *The Astrophysics of Cataclysmic Variables and Related Objects*, 2005.
- M. Georgousi, N. Karnesis, V. Korol, M. Pieroni, and N. Stergioulas. Gravitational waves from double white dwarfs as probes of the milky way. *Monthly Notices of the Royal Astronomical Society*, 2022.
- U. R. M. E. Geppert. *Thermal Evolution of Neutron Stars*. Springer International Publishing, 2016.
- F. Giovannelli. Cataclysmic variables: A review. *Chinese Journal of Astronomy Astrophysics*, 2008.
- J. Goliašch and L. Nelson. Population synthesis of cataclysmic variables: I. inclusion of detailed nuclear evolution. *The Astrophysical Journal*, 2015.

- R. Gomel, T. Mazeh, S. Faigler, D. Bashi, L. Eyer, L. Rimoldini, M. Audard, N. Mowlavi, B. Holl, G. Jevardat, et al. Gaia data release 3 - ellipsoidal variables with possible black hole or neutron star secondaries. *Astronomy and Astrophysics*, 2023.
- J. Greiner, R. Schwarz, and W. Wenzel. Discovery of the high-field polar RX J1724.0+4114. *Monthly Notices of the Royal Astronomical Society*, 1998.
- J. A. Guidry, Z. P. Vanderbosch, J. J. Hermes, B. N. Barlow, I. D. Lopez, T. M. Boudreaux, K. A. Corcoran, K. J. Bell, M. H. Montgomery, T. M. Heintz, et al. I Spy Transits and Pulsations: Empirical Variability in White Dwarfs Using Gaia and the Zwicky Transient Facility. *Astrophysical Journal*, 2021.
- J. Gunn and J. Ostriker. Magnetic dipole radiation from pulsars. *Nature*, 1969.
- B. T. Gänsicke, A. Fischer, R. Silvotti, and D. de Martino. A model for the optical high state light curve of am herculis. *Astronomy and Astrophysics*, 2001.
- B. T. Gänsicke, M. Dillon, J. Southworth, J. R. Thorstensen, P. Rodríguez-Gil, A. Aungwerojwit, T. R. Marsh, P. Szkody, S. C. C. Barros, J. Casares, et al. SDSS unveils a population of intrinsically faint cataclysmic variables at the minimum orbital period. *Monthly Notices of the Royal Astronomical Society*, 2009.
- G. Handler, J. A. Guzik, and P. A. Bradley. Delta scuti variables. In *AIP Conference Proceedings*. AIP, 2009.
- T. E. Harrison and R. K. Campbell. The wise light curves of polars. *The Astrophysical Journal Supplement Series*, 2015.
- M. Hertfelder, W. Kley, V. Suleimanov, and K. Werner. The boundary layer in compact binaries. *Astronomy and Astrophysics*, 2013.
- W. Ho and N. Andersson. Rotational evolution of young pulsars due to superfluid decoupling. *Nature Physics*, 2012.
- D. I. Hoffman, T. E. Harrison, J. L. Coughlin, B. J. McNamara, J. A. Holtzman, G. E. Taylor, and W. T. Vestrand. New lyrae and algal candidates from the northern sky variability survey. *The Astronomical Journal*, 2008.
- I. Iben. Stellar evolution within and off the main sequence. *Annual Review of Astronomy and Astrophysics*, 1967.

- A. Imada, T. Kato, K. Kubota, M. Uemura, R. Ishioka, S. Kiyota, K. Kinugasa, H. Maehara, K. Nakajima, L. A. G. B. Monard, et al. The 2003/2004 Superoutburst of SDSS J013701.06091234.9. *Publications of the Astronomical Society of Japan*, 2006.
- K. Inight, B. T. Gänsicke, E. Breedt, H. T. Israel, S. P. Littlefair, C. J. Manser, T. R. Marsh, T. Mulvany, A. F. Pala, and J. R. Thorstensen. A catalogue of cataclysmic variables from 20 yr of the sloan digital sky survey with new classifications, periods, trends, and oddities. *Monthly Notices of the Royal Astronomical Society*, 2023.
- M. J. Ireland, M. Scholz, P. G. Tuthill, and P. R. Wood. Pulsation of M-type Mira variables with moderately different mass: search for observable mass effects. *Monthly Notices of the Royal Astronomical Society*, 2004.
- IRSA. [Galactic Dust Reddening and Extinction](#), 2024. Accessed 18-06-24.
- IRSA. , 2025. Accessed 01-03-25.
- J. Isern, E. García-Berro, B. Külebi, and P. Lorén-Aguilar. A common origin of magnetism from planets to white dwarfs. *The Astrophysical Journal Letters*, 2017.
- N. Ivanova, S. Justham, X. Chen, O De Marco, C.L. Fryer, E. Gaburov, H. Ge, E. Glebbeek, Z. Han, X.-D. Li, et al. Common envelope evolution: where we stand and how we can move forward. *The Astronomy and Astrophysics Review*, 2013a.
- N. Ivanova, S. Justham, J. L. Avendano Nandez, and J. C. Lombardi. Identification of the long-sought common-envelope events. *Science*, 2013b.
- N. Ivanova, S. Justham, and P. Ricker. *Common Envelope Evolution*. IOP Publishing, 2020.
- C. P. Johnstone, M. Güdel, T. Lüftinger, G. Toth, and I. Brott. Stellar winds on the main-sequence - i. wind model. *Astronomy and Astrophysics*, 2015.
- A. Joshi, J. C. Pandey, A. Raj, K. P. Singh, G. C. Anupama, and H. P. Singh. Optical and X-ray studies of three polars: RX J0859.1+0537, RX J0749.1-0549, and RX J0649.8-0737. *Monthly Notices of the Royal Astronomical Society*, 2020.
- F. Juhan, A. King, and D. Raine. *Accretion Power in Astrophysics, Third Edition*. Cambridge University Press, 2002.

- S. Kafka, C. Tappert, and R. K. Honeycutt. Evidence for an accretion steam in the low-accretion-rate polar J2048. *Monthly Notices of the Royal Astronomical Society*, 2010.
- L. Kaper, A. van der Meer, M. van Kerkwijk, and E. van den Heuvel. Measuring the Masses of Neutron Stars. *The Messenger*, 2006.
- T. Kato. Three Z Camelopardalis-type dwarf novae exhibiting IW Andromedae-type phenomenon. *Publications of the Astronomical Society of Japan*, 2018.
- T. Kato, D. Nogami, and H. Baba. DI Ursae Majoris: Discovery of an Extreme ER UMa-Type Dwarf Nova with the Shortest Orbital Period. *Publications of the Astronomical Society of Japan*, 1996.
- T. Kato, R. Stubbings, P. Nelson, R. Santallo, R. Ishioka, M. Uemura, T. Sumi, Y. Muraki, P. Kilmartin, I. Bond, S. Noda, et al. The nature of v359 centauri revealed: New long-period su uma-type dwarf nova. *Astronomy and Astrophysics*, 2002.
- T. Kato, A. Imada, M. Uemura, D. Nogami, H. Maehara, R. Ishioka, H. Baba, K. Matsumoto, H. Iwamatsu, K. Kubota, et al. Survey of Period Variations of Superhumps in SU UMa-Type Dwarf Novae. *Publications of the Astronomical Society of Japan*, 2009.
- C. Kiefer. *Why Quantum Gravity?* Springer Berlin Heidelberg, 2007.
- A. R. King and U. Kolb. The evolution of black hole mass and angular momentum. *Monthly Notices of the Royal Astronomical Society*, 1999.
- R. Kippenhahn, A. Weigert, and A. Weiss. *Stellar Structure and Evolution*. Springer Berlin, 2012.
- C. Knigge. The donor stars of cataclysmic variables. *Monthly Notices of the Royal Astronomical Society*, 2006.
- C. Knigge, I. Baraffe, and J. Patterson. The Evolution of Cataclysmic Variables as Revealed by Their Donor Stars. *The Astrophysical Journal Supplement Series*, 2011.
- D. Koester, H. Schulz, and V. Weidemann. Atmospheric parameters and mass distribution of da white dwarfs. *Astronomy and Astrophysics*, 1979.

- J. Kollmeier, S. F. Anderson, G. A. Blanc, M. R. Blanton, K. R. Covey, J. Crane, N. Drory, P. M. Frinchaboy, C. S. Froning, J. A. Johnson, et al. SDSS-V Pioneering Panoptic Spectroscopy. In *Bulletin of the American Astronomical Society*, 2019.
- R. P. Kraft. On the structure and evolution of w ursae majoris stars. *Publications of the Astronomical Society of the Pacific*, 1967.
- C. Y. Lam, J. R. Lu, A. Udalski, I. Bond, Bennett. D. P., J. Skowron, P. Mróz, R. Poleski, T. Sumi, M. K. Szymański, et al. An isolated mass-gap black hole or neutron star detected with astrometric microlensing. *The Astrophysical Journal Letters*, 2022.
- H. J. G. L. M. Lamers and E. M. Levesque. *White Dwarfs and Neutron Stars*. IOP Publishing, 2017.
- O. Latković, A. Čeki, and S. Lazarević. Statistics of 700 individually studied w uma stars. *The Astrophysical Journal Supplement Series*, 2021.
- J. Levin, D. J. D’Orazio, and S. Garcia-Saenz. Black hole pulsar. *Physical Review D*, 2018.
- W. Lewin and M. van der Klis, editors. *Compact Stellar X-ray Sources*. Cambridge University Press, 2006.
- W.H.G. Lewin, E.P.J. van den Heuvel, and J. van Paradijs. *X-ray Binaries*. Cambridge University Press, 1997.
- J. Li. Magnetic braking in single and binary stars. *Publications of the Astronomical Society of Australia*, 1994.
- Lick Observatory. [Shane Telescope Overview](#), 2021. Accessed 16-09-24.
- LIGO. [Gravitational Waves - Why Detect Them?](#), 2024. Accessed 19-06-24.
- I. Lima, G. J. M. Luna, K. Mukai, A. Oliveira, J. Sokoloski, F. Walter, N. Palivanas, N. Nuñez, R. Souza, and R. Araujo. Symbiotic stars in x-rays iv: Xmm-newton, swift and tess observations, 2024.
- L. Lindgren. [Re-normalising the astrometric chi-square in Gaia DR2](#), 2024. Accessed 09-07-24.

- C. Littlefield, P. A. Mason, P. Garnavich, P. Szkody, J. Thorstensen, S. Scaringi, K. Izkiewicz, M. R. Kennedy, and N. Wells. Sdss j134441.83+204408.3: A highly asynchronous short-period magnetic cataclysmic variable with a 56 mg field strength. *The Astrophysical Journal Letters*, 2023.
- N. R. Lomb. Least-Squares Frequency Analysis of Unequally Spaced Data. *Astrophysics and Space Science*, 1976.
- D. R. Lorimer. Binary and millisecond pulsars. *Living Reviews in Relativity*, 2008.
- S. H. Lubow and F. H. Shu. Gas dynamics of semidetached binaries. *The Astrophysical Journal*, 1975.
- L. B. Lucy. The Light Curves of W Ursae Majoris Stars. *The Astrophysical Journal*, 1968.
- V. V. Lukin, K. L. Malanchev, N. I. Shakura, K. A. Postnov, V. M. Chechetkin, and V. P. Utrobin. 3D modelling of accretion disc in eclipsing binary system V1239 Her. *Monthly Notices of the Royal Astronomical Society*, 2017.
- G. J. M. Luna, J. L. Sokoloski, K. Mukai, and T. Nelson. Symbiotic stars in x-rays. *Astronomy and Astrophysics*, 2013.
- P. Marchant, K. Pappas, M. Gallegos-Garcia, C. Berry, R. Taam, V. Kalogera, and P. Podsiadlowski. The role of mass transfer and common envelope evolution in the formation of merging binary black holes. *Astronomy and Astrophysics*, 2021.
- T. R. Marsh. , 2025. Accessed 25-02-25.
- T. R. Marsh, B. T. Gänsicke, S. Hümmelich, F.-J. Hambsch, K. Bernhard, C. Lloyd, E. Breedt, E. R. Stanway, D. T. Steeghs, S. G. Parsons, et al. A radio-pulsing white dwarf binary star. *Nature*, 2016.
- F. J. Masci, R. R. Laher, B. Rusholme, D. L. Shupe, S. Groom, J. Surace, E. Jackson, S. Monkevitz, R. Beck, D. Flynn, et al. [ZTF Explanatory Supplement](#), 2020. Accessed 09-07-24.
- P. A. Mason, N. K. Wells, M. Motsoaledi, P. Szkody, and E. Gonzalez. CRTS J035010.7+323230, a new eclipsing polar in the cataclysmic variable period gap. *Monthly Notices of the Royal Astronomical Society*, 2019.
- J. A. Mattei. Introducing Mira Variables. *The Journal of the American Association of Variable Star Observers*, 1997.

- G. P. McCook and E. M. Sion. A catalog of spectroscopically identified white dwarfs. *The Astrophysical Journal Supplement Series*, 1999.
- P. McGill, J. Anderson, S. Casertano, K. C. Sahu, P. Bergeron, S. Blouin, P. Dufour, L. C. Smith, N. W. Evans, V. Belokurov, et al. First semi-empirical test of the white dwarf mass–radius relationship using a single white dwarf via astrometric microlensing. *Monthly Notices of the Royal Astronomical Society*, 2022.
- G. Meynet, P. Eggenberger, and A. Maeder. Massive star models with magnetic braking. *Astronomy and Astrophysics*, 2011.
- J. Mikolajewska. Orbital and stellar parameters of symbiotic stars, 2002.
- Nasa. [TESS Mission Objectives](#), 2024. Accessed 25-07-24.
- J.-U. Ness, J. H. M. M. Schmitt, V. Burwitz, R. Mewe, and P. Predehl. Chandra lets observation of the active binary algol. *Astronomy and Astrophysics*, 2002.
- N. Niang, Ü. Ertan, A. A. Gençali, O. Toyran, A. Ulubay, E. Devlen, M. A. Alpar, and E. Gügerçinoğlu. On the lack of X-ray pulsation in most neutron star low-mass X-ray binaries. *Monthly Notices of the Royal Astronomical Society*, 2024.
- K. Ny, J. Rosato, R. Stamm, J. Kovacevic-Dojcinovic, M. Dimitrijevic, L. Popovic, and Z. Simić. A new analysis of stark and zeeman effects on hydrogen lines in magnetized da white dwarfs. *Atoms*, 2017.
- T. N. O’Doherty, A. Bahramian, A. J. Goodwin, J. C. A Miller-Jones, J. A. Orosz, and J. Strader. A contact binary mis-classified as an ellipsoidal variable: Complications for detached black hole searches, 2024.
- A. Olech, E. de Miguel, M. Otulakowska, J. R. Thorstensen, A. Rutkowski, R. Novak, G. Masi, M. Richmond, B. Staels, S. Lowther, et al. Sdss j162520.29+120308.7 – a new su ursae majoris star in the period gap. *Astronomy and Astrophysics*, 2011.
- A. S. Oliveira, C. V. Rodrigues, D. Cieslinski, F. J. Jablonski, K. M. G. Silva, L. A. Almeida, A. Rodríguez-Ardila, and M. S. Palhares. Exploratory spectroscopy of magnetic cataclysmic variables candidates and other variable objects. *The Astronomical Journal*, 2017.
- Y. Osaki. An accretion model for the outbursts of u geminorum stars. *Astronomical Society of Japan*, 1974.

- Y. Osaki and T. Kato. The Cause of the Superoutburst in SU UMa Stars is Finally Revealed by Kepler Light Curve of V1504 Cygni. *Publications of the Astronomical Society of Japan*, 2013a.
- Y. Osaki and T. Kato. Study of superoutbursts and superhumps in su uma stars by the kepler light curves of v344 lyrae and v1504 cygni. *Publications of the Astronomical Society of Japan*, 2013b.
- S. P. Owocki, K. G. Gayley, and N. J. Shaviv. A Porosity-Length Formalism for Photon-Tiring-limited Mass Loss from Stars above the Eddington Limit. *The Astrophysical Journal*, 2004.
- B. Paczynski. Common Envelope Binaries. In *Structure and Evolution of Close Binary Systems*, 1976.
- B. Paczynski and R. Sienkiewicz. The minimum period and the gap in periods of cataclysmic binaries. *The Astrophysical Journal*, 1983.
- A. F. Pala, B. T. Gänsicke, E. Breedt, C. Knigge, J. J. Hermes, N. P. Gentile Fusillo, M. A. Hollands, T. Naylor, I. Pelisoli, M. R. Schreiber, et al. A Volume-limited Sample of Cataclysmic Variables from Gaia DR2: Space Density and Population Properties. *Monthly Notices of the Royal Astronomical Society*, 2020.
- J. Patterson, J. Kemp, D. R. Skillman, D. A. Harvey, A. W. Shafter, T. Vanmunster, L. Jensen, R. Fried, S. Kiyota, J. R. Thorstensen, et al. Superhumps in Cataclysmic Binaries. XV. EG Cancri, King of the Echo Outbursts. *Publications of the Astronomical Society of the Pacific*, 1998.
- M. J. Pecaut and E. E. Mamajek. Intrinsic Colors, Temperatures, and Bolometric Corrections of Pre-main-sequence Stars. *The Astrophysical Journal*, 2013.
- I. Pelisoli, T. R. Marsh, D. A. H. Buckley, I. Heywood, S. B. Potter, A. Schwope, J. Brink, A. Standke, S. G. Parsons, M. J. Green, et al. A 5.3-min-period pulsing white dwarf in a binary detected from radio to x-rays. *Nature*, 2023.
- Q.-H. Peng and H. Tong. The physics of strong magnetic fields in neutron stars. *Monthly Notices of the Royal Astronomical Society*, 2007.
- C. Petretti, J. Neilsen, and J. Homan. Determining the orbital period and wind geometry in gro j1655–40. *The Astrophysical Journal*, 2023.
- A. Philippov, A. Timokhin, and A. Spitkovsky. Origin of pulsar radio emission. *Physical Review Letters*, 2020.

- P. Podsiadlowski. *The evolution of binary systems*. Cambridge University Press, 2014.
- O. Pols. [Binary Stars](#), 2015. Accessed 11-04-24.
- R. Popham and R. Narayan. Accretion Disk Boundary Layers in Cataclysmic Variables. I. Optically Thick Boundary Layers. *The Astrophysical Journal*, 1995.
- A. Y. Potekhin. The physics of neutron stars. *Physics-Uspekhi*, 2010.
- P. Predehl, R. Andritschke, V. Arefiev, V. Babyshkin, O. Batanov, W. Becker, H. Böhringer, A. Bogomolov, T. Boller, K. Borm, et al. The eROSITA x-ray telescope on SRG. *Astronomy and Astrophysics*, 2021.
- A. S. Rajpurohit, F. Allard, S. Rajpurohit, R. Sharma, G. D. C. Teixeira, O. Mousis, and R. Kamlesh. Exploring the stellar properties of M dwarfs with high-resolution spectroscopy from the optical to the near-infrared. *Astronomy and Astrophysics*, 2018.
- G. Ramsay, M. J. Green, T. R. Marsh, T. Kupfer, E. Breedt, V. Korol, P. J. Groot, C. Knigge, G. Nelemans, D. Steeghs, et al. Physical properties of AM CVn stars: New insights from Gaia DR2. *Astronomy and Astrophysics*, 2018.
- S. Rappaport, F. Verbunt, and P. C. Joss. A new technique for calculations of binary stellar evolution application to magnetic braking. *The Astrophysical Journal*, 1983.
- N. Rawat, J. C. Pandey, A. Joshi, S. B. Potter, A. S. Hojaev, M. De Becker, S. M. Rao, and U. Yadava. Confirmation of two magnetic cataclysmic variables as polars: 1RXS J174320.1042953 and YY Sex. *Monthly Notices of the Royal Astronomical Society*, 2023.
- A. Reisenegger. Origin and evolution of neutron star magnetic fields, 2003.
- L. Rezzolla, E. R. Most, and L. R. Weih. Using gravitational-wave observations and quasi-universal relations to constrain the maximum mass of neutron stars. *The Astrophysical Journal Letters*, 2018.
- G. R. Ricker, J. N. Winn, R. Vanderspek, D. W. Latham, G. Á. Bakos, J. L. Bean, Z. K. Berta-Thompson, T. M. Brown, L. Buchhave, N.R. Butler, and title="Transiting Exoplanet Survey Satellite (TESS)" others. Transiting Exoplanet Survey Satellite (TESS). *Journal of Astronomical Telescopes, Instruments, and Systems*, 2015.

- H. Ritter. On the masses and evolution of cataclysmic binaries. *Monthly Notices of the Royal Astronomical Society*, 1976.
- C. V. Rodrigues, F. J. Jablonski, F. D’Amico, D. Cieslinski, J. E. Steiner, M. P. Diaz, and G. R. Hickel. Optical polarimetry and infrared photometry of two AM Her binaries: 1RXS J161008.0+035222 and 1RXS J231603.9052713\*. *Monthly Notices of the Royal Astronomical Society*, 2006.
- A. C. Rodriguez. From active stars to black holes: A discovery tool for galactic x-ray sources. *Publications of the Astronomical Society of the Pacific*, 2024.
- A. L. Rosen. A massive star is born: How feedback from stellar winds, radiation pressure, and collimated outflows limits accretion onto massive stars. *The Astrophysical Journal*, 2022.
- K. C. Sahu, J. Anderson, S. Casertano, H. E. Bond, P. Bergeron, E. P. Nelan, L. Pueyo, T. M. Brown, A. Bellini, Z. G. Levay, et al. Relativistic deflection of background starlight measures the mass of a nearby white dwarf star. *Science*, 2017.
- M. Salaris and S. Cassisi. *The Hydrogen Burning Phase*. John Wiley Sons, Ltd., 2005.
- Salvato, M., Wolf, J., Dwelly, T., Georgakakis, A., Brusa, M., Merloni, A., Liu, T., Toba, Y., Nandra, K., Lamer, G., et al. The erosita final equatorial-depth survey (efeds) - identification and characterization of the counterparts to point-like sources. *Astronomy and Astrophysics*, 2022.
- D. Salvetti, R. P. Mignani, A. De Luca, C. Delvaux, C. Pallanca, A. Belfiore, M. Marelli, A. A. Breeveld, J. Greiner, W. Becker, et al. Multi-wavelength observations of 3fgl j2039.6–5618: A candidate redback millisecond pulsar. *The Astrophysical Journal*, 2015.
- D. Sanyal, L. Grassitelli, N. Langer, and J. M. Bestenlehner. Massive main-sequence stars evolving at the eddington limit. *Astronomy and Astrophysics*, 2015.
- J. D. Scargle. Studies in astronomical time series analysis. II. Statistical aspects of spectral analysis of unevenly spaced data. *The Astrophysical Journal*, 1982.
- Meir Schochet, Jamie Tayar, and Jeff J. Andrews. A lack of mass-gap compact object binaries in apogee, 2024.

- M. R. Schreiber, M. Zorotovic, and T. P. G. Wijnen. Three in one go: consequential angular momentum loss can solve major problems of CV evolution. *Monthly Notices of the Royal Astronomical Society*, 2016.
- M. R. Schreiber, D. Belloni, B. T. Gänsicke, S. G. Parsons, and M. Zorotovic. The origin and evolution of magnetic white dwarfs in close binary stars. *Nature Astronomy*, 2021.
- M. R. Schreiber, D. Belloni, and J. van Roestel. Period bouncers as detached magnetic cataclysmic variables. *Astronomy and Astrophysics*, 2023.
- A. Schwarzenberg-Czerny. On the advantage of using analysis of variance for period search. *Monthly Notices of the Royal Astronomical Society*, 1989.
- A. Schwarzenberg-Czerny. Fast and Statistically Optimal Period Search in Uneven Sampled Observations. *Astrophysical Journal Letters*, 1996.
- A. Schwarzenberg-Czerny. [PyAOV](#), 2024. Accessed 13-07-24.
- SDSS. [Frequently Asked Questions](#), 2021. Accessed 17-09-24.
- N. R. Sibgatullin and R. A. Sunyaev. Energy Release During Disk Accretion onto a Rapidly Rotating Neutron Star. *Astronomy Letters*, 2000.
- K. M. G. Silva, C. V. Rodrigues, A. S. Oliveira, L. A. Almeida, D. Cieslinski, J. E. R. Costa, and F. J. Jablonski. MLS110213:022733+130617: a new eclipsing polar above the period gap. *Monthly Notices of the Royal Astronomical Society*, 2015.
- R. C. Smith. Cataclysmic variables. *Contemporary Physics*, 2006.
- J.-E. Solheim. Am cvn stars: Status and challenges. *Publications of the Astronomical Society of the Pacific*, 2010.
- H. Spruit. *Accretion Processes in Astrophysics*. Cambridge University Press, 2014.
- R. Staubert, J. Trümper, E. Kendziorra, D. Klochkov, K. Postnov, P. Kretschmar, K. Pottschmidt, F. Haberl, R. E. Rothschild, A. Santangelo, et al. Cyclotron lines in highly magnetized neutron stars. *Astronomy and Astrophysics*, 2019.
- J. Strader, S. Swihart, L. Chomiuk, A. Bahramian, C. Britt, C. C. Cheung, K. Dage, J. Halpern, K. Li, R. P. Mignani, et al. Optical spectroscopy and demographics of redback millisecond pulsar binaries. *The Astrophysical Journal*, 2019.
- STScI. , 2025a. Accessed 01-03-25.

- STScI. , 2025b. Accessed 01-03-25.
- STScI. , 2025c. Accessed 01-03-25.
- Y. Suwa, T. Yoshida, M. Shibata, H. Umeda, and K. Takahashi. On the minimum mass of neutron stars. *Monthly Notices of the Royal Astronomical Society*, 2018.
- R. E. Taam and E. L. Sandquist. Common envelope evolution of massive binary stars. *Annual Review of Astronomy and Astrophysics*, 2000.
- M. B. Taylor. STILTS - A Package for Command-Line Processing of Tabular Data. In *Astronomical Society of the Pacific Conference Series*, 2006.
- M. B. Taylor. [STILTS](#), 2024. Accessed 23-06-24.
- TESS. , 2025. Accessed 01-03-25.
- TESS Science Support Center. , 2025. Accessed 03-03-25.
- K. S. Thorne. Disk-Accretion onto a Black Hole. II. Evolution of the Hole. *The Astrophysical Journal*, 1974.
- John R. Thorstensen. Spectroscopic studies of 30 short-period cataclysmic variable stars and remarks on the evolution and population of similar objects. *The Astronomical Journal*, 2020.
- TNO. [TNT Specification](#), 2019. Accessed 12-09-24.
- J. L. Tonry, L. Denneau, A. N. Heinze, B. Stalder, K. W. Smith, S. J. Smartt, C. W. Stubbs, H. J. Weiland, and A. Rest. Atlas: A high-cadence all-sky survey system. *Publications of the Astronomical Society of the Pacific*, 2018.
- J. Trümper. Rosat—a new look at the x-ray sky. *Science*, 1993.
- M. Turchetta, M. Linares, K. Koljonen, and B. Sen. Quantifying irradiation in spider pulsars: the extreme case of PSR J16220315. *Monthly Notices of the Royal Astronomical Society*, 2023.
- J. T. VanderPlas. Understanding the lomb–scargle periodogram. *The Astrophysical Journal Supplement Series*, 2018.
- C. Vidal. Pulsar positioning system: a quest for evidence of extraterrestrial engineering. *International Journal of Astrobiology*, page 213–234, 2019.

- N. Vogt. The su uma stars - an important sub-group of dwarf-novae. *Astronomy and Astrophysics*, 1980.
- B. Warner. On the masses of cataclysmic variable stars. *Monthly Notices of the Royal Astronomical Society*, 1973.
- B. Warner. *Cataclysmic Variable Stars*. Cambridge University Press, 1995.
- A. P. Whitworth and O. Lomax. Are the majority of sun-like stars single? *Monthly Notices of the Royal Astronomical Society*, 2015.
- T. P. G. Wijnen, M. Zorotovic, and M. R. Schreiber. White dwarf masses in cataclysmic variables. *Astronomy and Astrophysics*, 2015.
- D. J. Wilson, O. Toloza, J. D. Landstreet, B. T. Gänsicke, J. J. Drake, J. J. Hermes, and D. Koester. Discovery of a young pre-intermediate polar. *Monthly Notices of the Royal Astronomical Society*, 2021.
- B. E. Wood. Astrospheres and solar-like stellar winds. *Living Rev. Sol. Phys*, 2004.
- K. Wu and L. L. Kiss. High and low states of the system am herculis. *Astronomy and Astrophysics*, 2008.
- O. Yoji. Dwarf-nova outbursts. *Publications of the Astronomical Society of the Pacific*, 1996.
- E. Zari, H. Hashemi, A. G. A. Brown, K. Jardine, and P. T. de Zeeuw. 3D mapping of young stars in the solar neighbourhood with Gaia DR2. *Astronomy and Astrophysics*, 2018.

# Appendix A

## White Dwarf Pulsar Candidates

Gaia Source ID	Identifier	RA deg	Dec deg
564802664874705536	J003837.51+792137.30	9.6565	79.3603
427229437850544512	J003854.80+611300.01	9.7285	61.2167
405035207224494080	J010643.91+531721.91	16.6829	53.2894
307194241607268992	J010858.30+273250.82	17.2429	27.5474
2465053942183130240	J013701.07−091234.72	24.2543	−9.2099
74525692700241408	J022732.87+130617.09	36.8869	13.1047
454397408096055424	J024246.70+550740.82	40.6946	55.128
216866264713691904	J035010.74+323229.72	57.5448	32.5415
5093945085525624448	J035055.99−204815.82	57.7334	−20.8044
159891122647000192	J045254.56+301718.00	73.2274	30.2886
3408324422192886528	J045944.04+192622.81	74.9335	19.4396
186765862593314944	J050353.15+372525.39	75.9714	37.4237
3417582928575520768	J052115.87+251332.15	80.3161	25.2254
3335057979544055168	J055128.99+075240.00	87.8708	7.878
3120280997380365824	J062429.71+002106.06	96.1238	0.3516
2933992632075460352	J065805.91−174424.97	104.5245	−17.7401
3057125354421645440	J073148.07−045952.92	112.9502	−4.9981
587316166180416640	J092444.48+080151.00	141.1853	8.0309
616146181399718528	J095308.20+145836.44	148.2843	14.9768
3776795812613678976	J103946.99−050658.32	159.9458	−5.1163
1680514565693517696	J123727.55+655211.79	189.3647	65.8699
3646410775989868800	J142438.93−022739.25	216.1622	−2.4609
6231616192056505984	J150353.98−220710.44	225.9749	−22.1196
4413231423818141568	J161007.51+035232.77	242.5313	3.8757
6244497859834924032	J162222.77−202707.78	245.5948	−20.4522
4331466855796298240	J162350.47−121731.12	245.9603	−12.2921
1304296149486147584	J162936.53+263519.63	247.4021	26.5888
4130951192276588672	J163459.38−202219.13	248.7474	−20.372
4357807993301167104	J163626.70−031655.18	249.1112	−3.282
4377736469755246080	J165359.18−033340.38	253.4967	−3.5612

1313538545446290688	J170213.25+322954.16	255.5553	32.4983
1347851790791563136	J172406.29+411407.69	261.0262	41.2353
4555766201373729920	J173208.39+204447.05	263.0349	20.7464
4488528655849813760	J175311.23+091555.41	268.2968	9.2654
4499667881166202624	J175505.11+132520.05	268.7713	13.4221
2151537856610343040	J181933.13+580626.07	274.888	58.1072
2140871494308695808	J190350.39+552410.86	285.9599	55.4031
4314366739882975872	J190753.75+135400.71	286.974	13.9002
2023839618412675328	J191837.52+251331.10	289.6563	25.2253
4211488524932719488	J192517.71−051956.14	291.3238	−5.3322
2032583037970999808	J193453.75+300547.89	293.7239	30.0966
1820591011340346368	J194732.86+155949.49	296.8869	15.997
2033873413612921088	J195033.63+315359.63	297.6401	31.8999
1806332647641007360	J200054.61+132331.54	300.2275	13.392
2250929515872371200	J200300.45+694150.62	300.7518	69.6974
2243995278291904768	J200821.06+623334.03	302.0877	62.5594
4223502720986764672	J201135.84−021340.49	302.8994	−2.2279
1862131728884948096	J202623.45+320108.27	306.5977	32.019
1755983188397718400	J204011.10+124403.71	310.0462	12.7343
2162478993740496256	J211129.53+445923.60	317.873	44.9899
2191758683454051584	J213251.46+602139.06	323.2145	60.3609
6810943641754934528	J213405.53−271648.39	323.523	−27.2802
1980608676604625536	J215153.41+504537.33	327.9726	50.7603
2218632465615722112	J222105.14+654033.56	335.2714	65.6759
2208852614629148800	J230538.37+652158.63	346.41	65.3663
1910713340903788160	J231013.92+321330.16	347.5579	32.2249
2299997867962066048	J231156.74+842323.10	347.9872	84.3898
1921680724575326464	J235354.93+415304.33	358.4791	41.8846

Table A.1: All candidate systems obtained through the search for white dwarf pulsars. Values labelled ‘Identifier’ are the systems J2000 coordinates in the format JHHMMSS.SS±DDMMSS.SS, RA are right ascensions, and Dec are declinations (both in degrees).

# Appendix B

## Black Hole Binary Candidates

Gaia Source ID	Identifier	RA deg	Dec deg
5115981600648173312	J034507.50–101821.34	56.28121166077	–10.30593389086
4786942536897924352	J045727.90–464538.12	74.36632148529	–46.76063447704
6011546843820042112	J154708.42–354019.66	236.78500488539	–35.67224863246
6373605440040712448	J204518.85–715801.17	311.32858668574	–71.96714267306
3230036240926962944	J044348.65+000926.05	70.95270640272	0.15718558195
6163143967998002560	J133030.39–361425.93	202.6267626198	–36.24058203604
5666192195737904000	J101200.11–222757.11	153.00028405657	–22.46582040677
5785917054813014016	J144100.52–773124.82	220.25224453206	–77.52353657589
6061163199393959168	J124201.02–565803.51	190.50396634067	–56.96762378094
4843620372741310208	J035601.78–384724.65	59.00747771298	–38.79019733862
5020393598782111232	J015736.37–311233.21	29.40153531961	–31.20931036628
5444748565336072576	J104237.76–334212.63	160.65713893105	–33.70339259168
6252791342905027712	J152240.54–211837.83	230.66879327416	–21.31051494536
4868483212566866176	J041704.02–375235.82	64.26675752953	–37.8766513582
5574393591977616256	J061802.49–391953.25	94.51032598977	–39.33148362584
3043879679578566912	J075309.22–065819.29	118.28841788428	–6.97211281971
6642506191320684288	J195239.85–522757.91	298.16601539917	–52.46612828504
6019484321357037184	J164103.55–370502.67	250.26475373626	–37.08421674949
5346631922949364864	J112024.12–544200.90	170.10024341611	–54.70015856189
4883676474694725120	J040626.56–320138.53	61.61064644352	–32.02740469464
3254866855614556032	J042408.64+002420.43	66.03608045286	0.40566656982
4815553169482903040	J043643.47–424629.42	69.18120386002	–42.77485245484
6173038232618037504	J140712.98–302443.66	211.8040750282	–30.41210128926
5109560280944174848	J035823.53–154206.43	59.59806265378	–15.70177691355
695430148108896640	J092749.73+283357.28	141.95723246727	28.56562469597
3011590665199973248	J054920.57–093825.58	87.3356960919	–9.64053907879
6165817018204434816	J131559.56–370017.73	198.99812140878	–37.00502309626
5714874451749946752	J075851.54–182100.06	119.71461610137	–18.34995453739
3148277582781224832	J074420.52+084336.25	116.08538970892	8.72669941018
3521698364667361664	J122149.42–152344.69	185.4558785924	–15.39576144124

5376113407399650432	J112728.64−441153.79	171.86920346837	−44.19828655664
3146379348973371776	J081113.74+090406.30	122.80718700368	9.06838835868
3458769981316233600	J115949.11−413439.09	179.95441944478	−41.57753506154
3209691560665300096	J052830.76−045403.73	82.12833222113	−4.90118552516
6003468452715574528	J151503.52−433712.50	228.7646305211	−43.62021793921

---

Table B.1: All ellipsoidally modulating candidate systems obtained through the search for black hole binaries. Values labelled ‘Identifier’ are the systems J2000 coordinates in the format JHHMMSS.SS±DDMMSS.SS, RA are right ascensions, and Dec are declinations (both in degrees).

## Appendix C

# Additional High-Speed Photometry

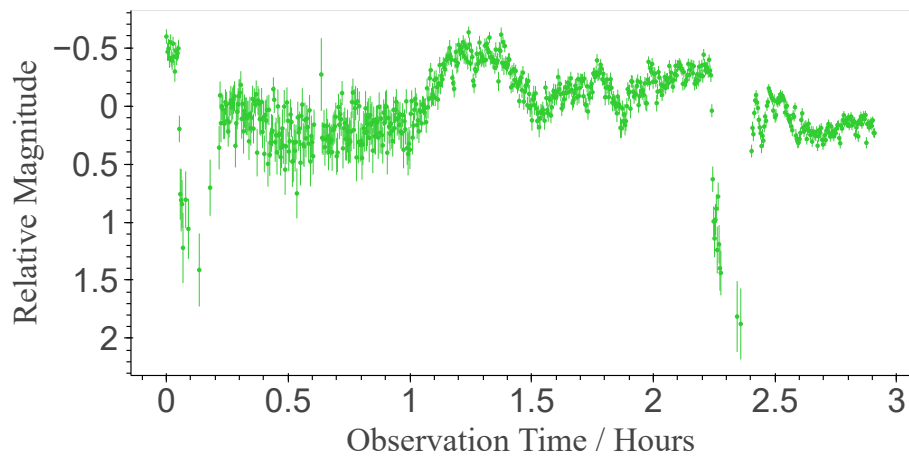


Figure C.1: TNT photometry of J092444.48+080151.00, a system identified in the search for white dwarf pulsars.

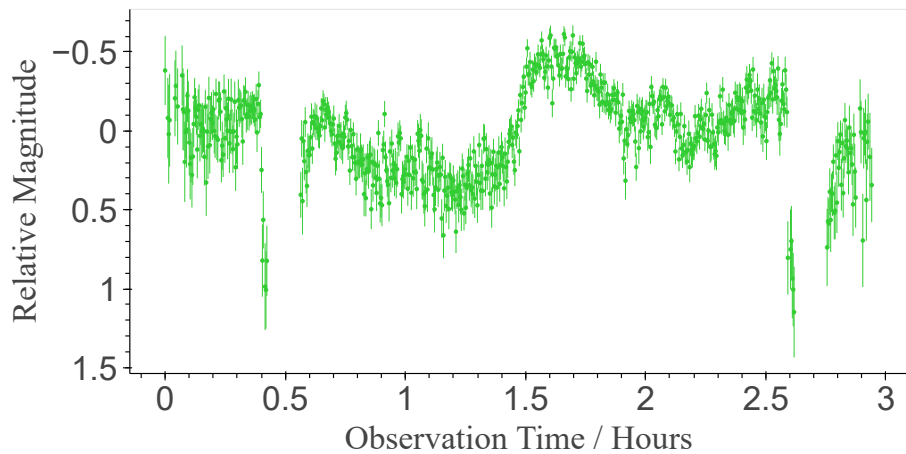


Figure C.2: Additional TNT photometry of J092444.48+080151.00, a system identified in the search for white dwarf pulsars.

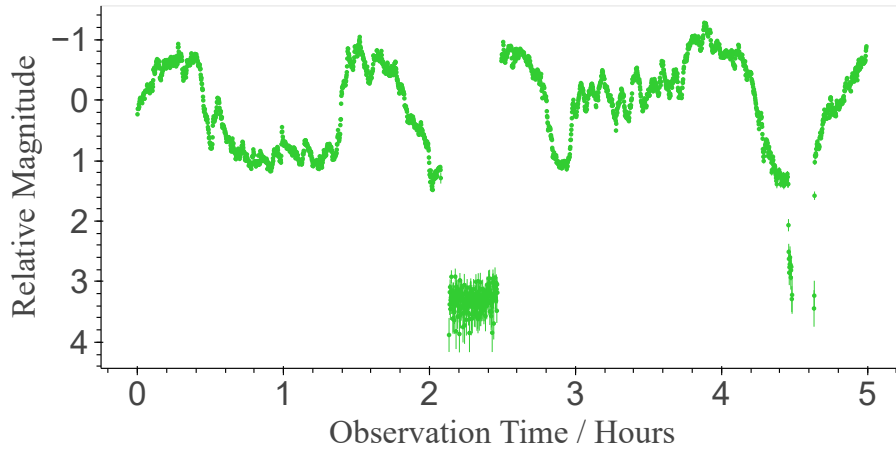


Figure C.3: TNT photometry of J065805.91-174424.97, a system identified in the search for white dwarf pulsars.

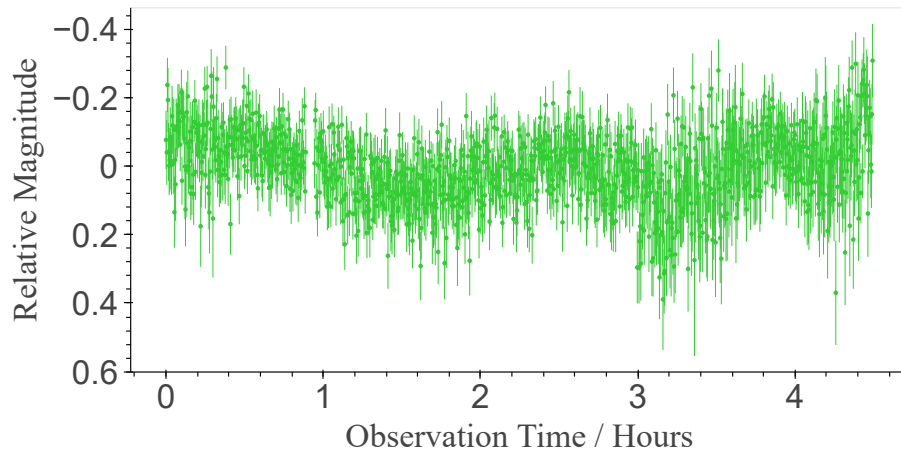


Figure C.4: TNT photometry of J055128.99+075240.00, a system identified in the search for white dwarf pulsars.

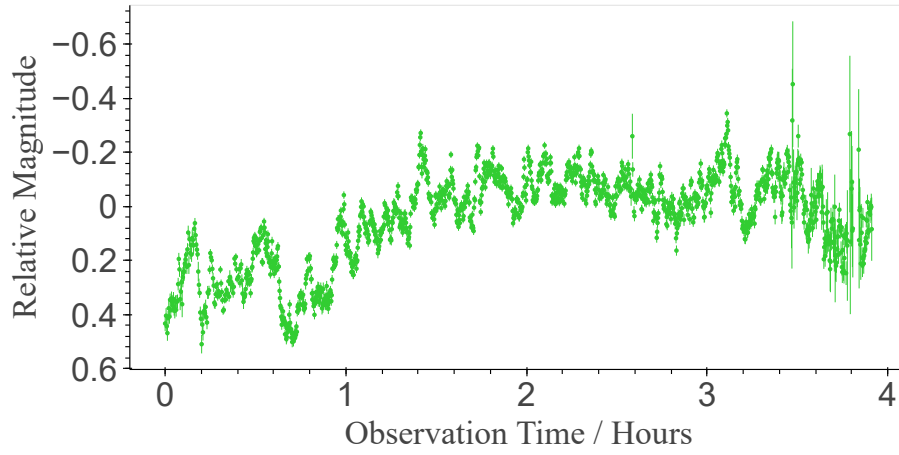


Figure C.5: TNT photometry of J052115.87+251332.15, a system identified in the search for white dwarf pulsars.

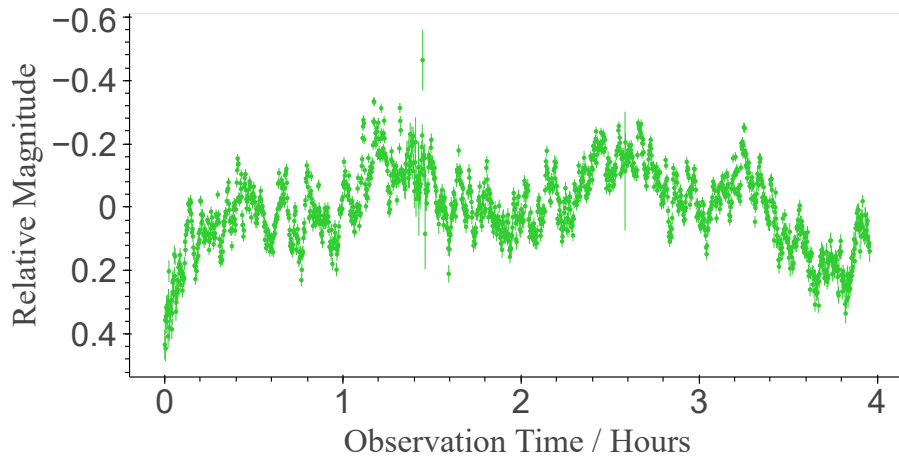


Figure C.6: Additional TNT photometry of J052115.87+251332.15, a system identified in the search for white dwarf pulsars.